

**UNCLASSIFIED**

SECURITY CLASSIFICATION OF THIS PAGE

ADA206282

**REPORT DOCUMENTATION PAGE**

Form Approved  
OMB No. 0704-0188

1a. REPORT SECURITY CLASSIFICATION <b>UNCLASSIFIED</b>		1b. RESTRICTIVE MARKINGS	
2a. SECURITY CLASSIFICATION AUTHORITY		3. DISTRIBUTION/AVAILABILITY OF REPORT <b>Approved for public release; distribution is unlimited.</b>	
2b. DECLASSIFICATION/DOWNGRADING SCHEDULE			
4. PERFORMING ORGANIZATION REPORT NUMBER(S) <b>ARL-TR-89-6</b>		5. MONITORING ORGANIZATION REPORT NUMBER(S)	
6a. NAME OF PERFORMING ORGANIZATION <b>Applied Research Laboratories</b>	6b. OFFICE SYMBOL (if applicable) <b>ARL:UT</b>	7a. NAME OF MONITORING ORGANIZATION <b>Office of the Chief of Naval Research</b>	
6c. ADDRESS (City, State, and ZIP Code) <b>The University of Texas at Austin P.O. Box 8029 Austin, Texas 78713-8029</b>		7b. ADDRESS (City, State, and ZIP Code) <b>Department of the Navy Arlington, Virginia 22217-5000</b>	
8a. NAME OF FUNDING/SPONSOR ORGANIZATION	8b. OFFICE SYMBOL (if applicable)	9. PROCUREMENT INSTRUMENT IDENTIFICATION NUMBER <b>N00014-87-K-0346</b>	
8c. ADDRESS (City, State, and ZIP Code)		10. SOURCE OF FUNDING NUMBERS	
		PROGRAM ELEMENT No.	PROJECT No.
		TASK No.	WORK UNIT ACCESSION No.
11. TITLE (Include Security Classification) <b>Acoustic Propagation Modeling in Shallow Water Using Ray Theory</b>			
12. PERSONAL AUTHOR(S) <b>Westwood, Evan K.</b>			
13a. TYPE OF REPORT <b>technical</b>	13b. TIME COVERED _____ TO _____	14. DATE OF REPORT (Year, Month, Day) <b>89-2-21</b>	15. PAGE COUNT <b>127</b>
16. SUPPLEMENTARY NOTATION			
17. COSATI CODES		18. SUPPLEMENTARY NOTATION	
FIELD	GROUP	<b>(see reverse side)</b>	
	SUB-GROUP		
19. ABSTRACT (Continue on reverse if necessary and identify by block number) <p>A ray method is developed for modeling acoustic propagation in low-frequency, shallow water ocean environments. The theoretical foundation is laid by studying the reflected and transmitted fields due to an acoustic point source in the presence of a plane, penetrable interface. Each field is expressed as a plane wave integral. The approach for solving the integral is based on the classical method of steepest descent, but the plane wave reflection and transmission coefficients are allowed to influence the location of the saddle points and their steepest descent paths. As a consequence, saddle points are, in general, complex, and complicated processes such as the reflected lateral wave field and the transmitted evanescent field are incorporated in the saddle point formulation. The saddle point criterion may be expressed in terms of eigenrays and their characteristics, which provides physical insight into the paths and mechanisms of propagation. The method developed for solving the single interface problem is then applied to two simple models for shallow water ocean environments: the flat, isovelocity waveguide (the Pekeris</p>			
20. DISTRIBUTION/AVAILABILITY OF ABSTRACT <input type="checkbox"/> UNCLASSIFIED UNLIMITED <input checked="" type="checkbox"/> SAME AS RPT. <input type="checkbox"/> DTIC USERS		21. ABSTRACT SECURITY CLASSIFICATION <b>UNCLASSIFIED</b>	
23. NAME OF RESPONSIBLE INDIVIDUAL <b>Clark S. Penrod</b>		22b. TELEPHONE (Include Area Code) <b>512 835 3473</b>	22c. OFFICE SYMBOL <b>EVG</b>

**UNCLASSIFIED**

# UNCLASSIFIED

18. ray theory complex rays shallow water sloping-bottom waveguide  
method of steepest descent benchmark wedge problems

19. (cont'd)

model) and the sloping-bottom, isovelocity waveguide (the penetrable wedge). For the flat waveguide, near perfect agreement is found between the ray model and a model whose algorithm solves the wave equation numerically (the SAFARI fast field model). The ray method proves to be accurate even when the water depth is only half of the acoustic wavelength. For the sloping-bottom waveguide, ray model solutions to benchmark problems proposed by the Acoustical Society of America are compared to solutions from a model based on two-way coupled mode theory. For cases of upslope propagation in shallow-water penetrable wedges, agreement between the two independent models is excellent, both in the water and in the bottom. The ray method is applied to the three-dimensional wedge problem, where the source and receiver may lie across the slope from each other. The ray method is also extended to model directional sources by placing a point source in complex space.

2/10/81  
E

UNCLASSIFIED

## TABLE OF CONTENTS

	<u>Page</u>
<b>LIST OF FIGURES</b>	vii
<b>PREFACE</b>	ix
<b>1 INTRODUCTION</b>	1
<b>2 COMPLEX RAY METHODS FOR ACOUSTIC INTERACTION AT A FLUID-FLUID INTERFACE</b>	4
2-1 INTRODUCTION . . . . .	4
2-2 PLANE WAVE INTEGRAL REPRESENTATION OF THE RE- FLECTED FIELD . . . . .	7
2-3 THE METHOD OF STEEPEST DESCENT . . . . .	14
2-3.1 General formulation . . . . .	14
2-3.2 Classical ray theory . . . . .	16
2-4 COMPLEX RAY FORMULATION . . . . .	18
2-4.1 Rearrangement of the integral . . . . .	18
2-4.2 Branch cuts in $V(\theta)$ . . . . .	19
2-5 SADDLE POINT STRUCTURE OF THE REFLECTED FIELD	20
2-6 COMPUTATION OF THE EIGENRAY FIELD . . . . .	24
2-7 GEOMETRIC INTERPRETATION . . . . .	28
2-7.1 Derivation of eigenray characteristics . . . . .	28
2-7.2 Analysis of the geometric spreading factors . . . . .	30
2-7.3 Interpretation of complex eigenrays . . . . .	32
2-8 THE TRANSMITTED FIELD IN THE BOTTOM . . . . .	33
2-8.1 Integral representation of the transmitted field . . . . .	33
2-8.2 Saddle point structure of the transmitted field . . . . .	35
2-8.3 Geometric interpretation of the transmitted field . . . . .	39
2-9 CONCLUSIONS . . . . .	42
<b>3 APPLICATION OF THE RAY METHOD TO FLAT AND SLOPING WAVEGUIDES</b>	43
3-1 INTRODUCTION . . . . .	43
3-2 RAY METHOD FOR THE FLAT WAVEGUIDE . . . . .	45

	<u>Page</u>
3-3 COMPARISON OF MODELS FOR THE FLAT WAVEGUIDE . . . . .	49
3-4 EIGENRAY STRUCTURE IN THE FLAT WAVEGUIDE . . . . .	54
3-5 RAY METHOD FOR THE SLOPING WAVEGUIDE . . . . .	56
3-5.1 Derivation of the plane wave integrals . . . . .	56
3-5.2 The mathematical basis for the multiplicity of lateral waves	60
3-6 COMPARISON OF MODELS FOR THE SLOPING WAVEGUIDE	62
3-7 EIGENRAY STRUCTURE IN THE SLOPING WAVEGUIDE . . . . .	62
3-8 CONCLUSIONS . . . . .	65
<b>4 RAY MODEL SOLUTIONS TO THE BENCHMARK WEDGE PROBLEMS</b>	<b>67</b>
4-1 INTRODUCTION . . . . .	67
4-2 THE BENCHMARK WEDGE PROBLEMS . . . . .	68
4-3 COMPARISONS BETWEEN MODELS . . . . .	69
4-4 ACCURACY AND EFFICIENCY CONSIDERATIONS . . . . .	70
4-5 ANALYSIS OF THE FIELD IN THE WEDGE . . . . .	74
4-5.1 Characteristics of eigenrays in the wedge . . . . .	75
4-5.2 Eigenrays in the bottom . . . . .	78
4-5.3 Backscatter . . . . .	80
4-6 CONCLUSIONS . . . . .	82
<b>5 THE THREE-DIMENSIONAL WEDGE PROBLEM</b>	<b>84</b>
5-1 INTRODUCTION . . . . .	84
5-2 DERIVATION OF THE PLANE WAVE INTEGRAL . . . . .	85
5-3 AN APPROXIMATE METHOD OF SOLUTION . . . . .	88
5-3.1 An analysis of the approximation . . . . .	90
<b>6 THE MODELING OF A DIRECTIONAL SOURCE</b>	<b>92</b>
6-1 INTRODUCTION . . . . .	92
6-2 THE FIELD DUE TO A COMPLEX POINT SOURCE IN FREE SPACE . . . . .	92
6-3 DETERMINATION OF COMPLEX SOURCE PARAMETERS . . . . .	94
6-4 REFLECTED AND TRANSMITTED FIELDS DUE TO AN INCIDENT BEAM . . . . .	96
6-5 EXAMPLES OF COMPUTED FIELDS . . . . .	98
6-6 SADDLE POINT STRUCTURE . . . . .	102
6-7 CONCLUSIONS . . . . .	103

7 CONCLUSIONS

107

REFERENCES

110

Accession For	
NTIS GRA&I	<input checked="" type="checkbox"/>
DTIC TAB	<input type="checkbox"/>
Unannounced	<input type="checkbox"/>
Justification	
By _____	
Distribution/	
Availability Codes	
Dist	Avail and/or Special
A-1	



## LIST OF FIGURES

		<u>Page</u>
2-1	Change of variable from rectangular coordinates $(k_x, k_y, k_z)$ to polar coordinates $(k, \theta, \phi)$ . . . . .	9
2-2	Geometry for the reflected field. . . . .	11
2-3	Contour of integration in the complex $\theta$ -plane for the reflected field integral. . . . .	13
2-4	Comparison between classical ray theory and the exact result for the normalized reflected field. . . . .	17
2-5	Saddle points and steepest descent paths for the reflected field. . . . .	21
2-6	Eigenray picture for the reflected field. . . . .	22
2-7	As in Fig. 2-5, except the lower medium has an attenuation of 0.5 dB/ $\lambda$ . . . . .	25
2-8	Eigenray interpretation of the saddle point $\gamma$ for the reflected field. . . . .	28
2-9	Geometric spreading of an eigenray (a) in the $\hat{\theta}$ -direction, and (b) in the $\hat{\phi}$ -direction. . . . .	31
2-10	Geometry for calculation of the transmitted field in the bottom. . . . .	34
2-11	Saddle points and steepest descent paths for the transmitted field. . . . .	36
2-12	Saddle points and steepest descent paths for a case where an additional "evanescent ray" saddle point must be found. . . . .	37
2-13	Comparison between classical ray theory and the exact result for the normalized transmitted field. . . . .	38
2-14	Interpretation of the transmitted field in terms of eigenrays. . . . .	39
3-1	Geometry for the flat waveguide. . . . .	46
3-2	Comparison of models for a flat waveguide of depth $h = 3.6\lambda$ . . . . .	50
3-3	As in Fig. 3-2, except the water depth has been reduced to $h = 3.5\lambda$ . . . . .	51
3-4	As in Fig. 3-2, except the bottom has an attenuation of 0.5 dB/ $\lambda$ . . . . .	52
3-5	Comparison of models for a flat waveguide of depth $h = 0.5\lambda$ . . . . .	53
3-6	Saddle points and steepest descent paths for the waveguide modeled in Fig. 3-2. . . . .	55
3-7	Geometry for the sloping waveguide. . . . .	57
3-8	Multiple lateral waves in a sloping waveguide. . . . .	61

	<u>Page</u>
3-9 Comparison of models for upslope propagation in a wedge of angle $\alpha = 2.86^\circ$ . . . . .	63
3-10 Eigenray structure in a sloping environment. . . . .	64
4-1 Geometry for the benchmark wedge problems . . . . .	69
4-2 Comparison between the ray model and the two-way coupled mode model for Benchmark 2. . . . .	71
4-3 Comparison between the ray model and the two-way coupled mode model for Benchmark 3. . . . .	72
4-4 Image method representation of a backscattered ray. . . . .	81
5-1 Geometry for the three-dimensional wedge problem. . . . .	86
6-1 Geometry for the directional source. . . . .	93
6-2 Calculation of the radius of phase front curvature $R_c$ . . . . .	95
6-3 Geometry for the reflection and transmission of a beam produced by a point source in complex space. . . . .	97
6-4 Reflected and transmitted field for an incident beam with angle $\theta_B = 55^\circ$ . . . . .	99
6-5 Reflected and transmitted field for an incident beam with angle $\theta_B = 62^\circ$ . . . . .	101
6-6 Reflected and transmitted field for an incident beam with angle $\theta_B = 68^\circ$ . . . . .	102
6-7 Saddle points and steepest descent paths for the reflected and transmitted fields in Fig. 6-4. . . . .	104
6-8 Saddle points and steepest descent paths for the reflected and transmitted fields in Fig. 6-6. . . . .	105

## PREFACE

This material was originally published in December 1988 as a dissertation, in partial fulfillment of the requirements for the degree of Doctor of Philosophy in Electrical Engineering, The University of Texas at Austin.

## CHAPTER 1

### INTRODUCTION

In the field of underwater sound, the ability to model acoustic propagation is an essential part of most practical applications. For example, the development of passive and active sonar systems, the estimation of ranges at which targets can be detected, and the study of the effects of ambient noise sources all require an understanding of how sound propagates in complex ocean environments.

In recent years, the advent of ever more powerful computers has enabled researchers to develop and implement sophisticated propagation models that numerically solve the acoustic wave equation or approximations to it. Such models rely on a thorough description of the environment, which must include the geometry (bathymetry, layering in the ocean bottom, and sea surface state, for example), as well as the acoustic properties of the media (sound speed, density, and attenuation, for example). However, even if the environment were known exactly, models typically have limitations associated with them, such as the ability to properly account for (1) dependence of the environmental parameters on range, (2) propagation in three-dimensional environments, (3) energy propagating at angles near vertical, (4) shear wave propagation in the ocean bottom, (5) scattering from rough surfaces, and (6) nonlinear effects. Practical limitations, such as the range of frequencies that can be modeled, often arise simply because the computation time is too large or the storage capacity of the computer is exceeded.

A problem with the development of any model is the evaluation of its accuracy. There are always factors that can introduce error in the results of a propagation model, such as approximations in the theoretical formulation, errors arising from numerical methods used in the computer algorithm, or simply errors in the coding of the program. One way to verify the accuracy of a model is to compare its solutions with those of another model that relies on a different method. This technique for model verification requires the definition of certain "benchmark" problems to which different models can be applied and their solutions compared. Recently, the Underwater Acoustics community of the Acoustical

Society of America proposed benchmark problems that address propagation in range-dependent environments. More specifically, the problems consist of a point source in a two-dimensional, isovelocity wedge of shallow water, surrounded above by air and below by sand. One concrete result of the present research is a new, accurate, and physically intuitive method for acoustic propagation modeling that can be applied to these benchmark problems.

The goal of the research in this dissertation has been to develop a method based on ray theory that is accurate in shallow water ocean environments. Since classical ray theory is based on a high-frequency approximation to the wave equation, it is *not* valid in shallow water, where the water depth is typically on the order of tens of wavelengths or less. In order to adapt classical ray theory, we begin with an exact formulation for the reflection and transmission of a spherical wave incident on a single plane interface. Preserving as much as possible the intuitive notions of ray theory, we develop a method for solving the single interface problem accurately, even at low frequencies. We then extend the method to calculate the field due to rays that undergo multiple reflections. Using these tools, we can calculate the total field in ocean environments with flat or sloping bottoms by summing together all of the significant rays. Unlike most numerical models, which provide little or no physical insight into the paths and mechanisms of propagation, the ray method developed here can be analyzed in terms of ray arrival angles, travel times, and propagation paths.

This dissertation is organized as follows. In Chapter 2 the basic method for finding the reflected and transmitted fields due to a point source in the presence of a single plane interface is developed. The extension to oceanic environments with flat and sloping bottoms is made in Chapter 3. In Chapter 4 we address in detail the benchmark wedge problems and show comparisons between solutions obtained from the ray model and from a two-way coupled mode model. The problem of propagation in a three-dimensional wedge, where sound travels *across* the sloping bottom rather than straight up or down the slope, is discussed in Chapter 5. In Chapter 6, we demonstrate how the methods we have developed for modeling a point source can be used to model a directional source. Several examples of the reflected and transmitted fields due to a beam incident on a fluid-fluid interface near the critical angle are given. Concluding remarks are made in Chapter 7.

Three of the chapters of this dissertation are based on manuscripts that were submitted for publication in the *Journal of the Acoustical Society of America* in 1988. Chapter 2 is based on the manuscript<sup>1</sup> entitled "Complex ray methods for acoustic interaction at a fluid-fluid interface," Chapter 3 is based on the manuscript<sup>2</sup> entitled "Ray methods for flat and sloping oceanic waveguides," and

Chapter 4 is based on the manuscript<sup>3</sup> entitled "Ray model solutions to the benchmark wedge problems." The results in the last manuscript were first reported at the 115th Meeting of the Acoustical Society of America in Seattle, Washington, in May 1988.<sup>4</sup>

## CHAPTER 2

### COMPLEX RAY METHODS FOR ACOUSTIC INTERACTION AT A FLUID-FLUID INTERFACE

#### 2-1 INTRODUCTION

One of the most basic problems in acoustics is that of the reflection and transmission of a spherical wave at a plane, fluid-fluid interface. In the case of underwater acoustics, this problem represents an idealized model for the interaction of a point-source field with the ocean bottom. More specifically, one isovelocity, constant-density halfspace (water) overlies another (sand, for example). In shallow water ocean environments, the lower medium usually has the higher velocity, which results in the presence of a critical angle in the plane wave reflection coefficient. Plane waves incident on the interface at angles "steeper" than the critical angle (closer to normal incidence) are partially reflected back into the water and partially transmitted into the bottom. Plane waves incident on the interface at angles "shallower" than the critical angle (closer to grazing incidence) are totally reflected back into the water. When the incident wave is a spherical wave, energy incident near the critical angle produces a wave that travels parallel to the interface in the bottom. As it propagates, it continually excites a wave called the *lateral wave* or *head wave*, which travels at the critical angle in the water.

The initial step in the mathematical analysis of the two-fluid model is to represent the incident spherical wave as a sum of (integral over) plane waves. An integral expression for the reflected or transmitted field at a given receiver point is then obtained by multiplying each plane wave in the integrand by the appropriate plane wave reflection or transmission coefficient. In the classic work of Brekhovskikh,<sup>5</sup> the author primarily uses the method of steepest descent to solve the integral. Briefly stated, this method involves finding the saddle point, deforming the contour of integration into the steepest descent path, and deriving an approximate solution to the integral. When viewed in terms of rays, the saddle point corresponds to the angle of the *eigenray*, a specific ray connecting the source

and receiver. The major complication in this analysis arises from the presence of the critical angle, which in mathematical terms corresponds to a branch point singularity in the reflection or transmission coefficient. When the saddle point lies sufficiently close to the critical angle, the usual methods for estimating the field break down.

Various improvements to the solution in the neighborhood of the critical angle have been developed. In Sec. 31 of Ref. 5, Brekhovskikh derives expressions for the reflected and lateral wave fields in the vicinity of the critical angle. Bleistein<sup>6</sup> derives uniform asymptotic expansions for integrals involving stationary points near algebraic singularities. In the present case, a saddle point lies near a branch point of order  $1/2$ . Stickler<sup>7</sup> refines the formulation by allowing for the possibility that the critical angle is close to grazing incidence. Chin-Bing and Davis<sup>8</sup> apply Bleistein's technique to the lateral wave expression and point out errors in Brekhovskikh's treatment. In all of these investigations, asymptotic expansions involving parabolic cylinder functions are derived.

In the present work, we wish to develop a method for finding the reflected and transmitted fields that (1) can be interpreted in terms of rays, (2) is applicable even at very low frequencies, and (3) can be extended to environments where more than one interface is present. The above-mentioned asymptotic expansions do not satisfy these criteria because (1) there is no physical interpretation of the terms in the expansion, (2) an expansion with a fixed number of terms will fail at a sufficiently low frequency, and (3) the treatment of multiply reflected fields would require a rederivation of the asymptotic expansion.

The approach we take in this dissertation is based on the saddle point method outlined by Brekhovskikh.<sup>5</sup> In one variation on this method, Brekhovskikh (Sec. 31.3) allows the *phase* of the reflection coefficient to influence the location of the saddle points. The result is a phenomenon commonly referred to as *beam displacement*, where totally reflected rays have a horizontal displacement along the interface before they are reflected back into the water. (Since the term "beam displacement" originated from the displacement of a beam incident on an interface, a more appropriate term for the present case would be *ray displacement*.) In recent years, the phenomenon of beam displacement has been included in ray theory calculations, and the resulting method successfully applied to the flat, isovelocity, penetrable-bottom waveguide (the Pekeris model)<sup>9,10,11</sup> and to the sloping-bottom waveguide.<sup>12</sup>

The one deficiency in the beam displacement formulation, however, is that it is not accurate in a certain "transition" region, where eigenray angles are close to the critical angle. At shorter ranges, the field can be expressed in terms of a single partially reflected eigenray, and at longer ranges, the field can be expressed

as a sum of two separate rays: a totally reflected eigenray and a lateral wave eigenray. But in the transition region, the field is more complicated and cannot be expressed as a simple ray field or even as a sum of simple ray fields. In this region the ray formulation breaks down — it predicts infinite intensity at caustics, points in space where two rays coalesce into one. Special caustic correction factors<sup>11,12</sup> based on uniform asymptotics are used to attempt to “patch up” the ray solution in this problematic region.

In the approach developed in this chapter, the key modification is to allow the *entire* reflection coefficient (amplitude as well as phase) to influence the locations of the saddle points. The result is that the saddle points become, in general, complex, corresponding to eigenrays that have complex angles of incidence  $\theta$ . In the neighborhood of the critical angle, the saddle point approximation to the integral still fails. However, in this region we find the exact field by numerically integrating along the steepest descent path in the complex  $\theta$ -plane. The number of integration points is made independent of frequency by choosing step sizes appropriately. In work done concurrently with the present research, Plumpton and Tindle<sup>13</sup> formulate an identical complex saddle point criterion for the single reflection problem and develop improved caustic correction procedures.

The notion of incorporating the reflection and transmission coefficients into the saddle point formulation is attractive because it allows the full effects of the interaction with the interface to be included. For example, in the case of the water-sand interface, our method accounts for the reflected lateral wave field as well as the evanescent wave field in the bottom. In cases where the total field is composed of several different ray fields, the individual contributions can be isolated.

In this chapter we develop our ray method while solving for the reflected field, and then apply it in a straightforward manner to the transmitted field. In Sec. 2-2 we derive the plane wave integral for the reflected field. In Sec. 2-3 we review the method of steepest descent and apply it in the usual way to the reflected field integral to obtain classical ray theory. In Sec. 2-4 we obtain the complex ray formulation by including the plane wave reflection coefficient in the saddle point criterion. The resulting saddle point structure is discussed in Sec. 2-5, and the technique for evaluating the field is summarized in Sec. 2-6. In Sec. 2-7 we interpret the saddle point formulation in terms of eigenrays. Section 2-8 contains the solution for and analysis of the transmitted field. Concluding remarks are made in Sec. 2-9.

## 2-2 PLANE WAVE INTEGRAL REPRESENTATION OF THE REFLECTED FIELD

In this section we derive the plane wave integral representation for the reflected field. The derivation follows the treatment by Brekhovskikh in Secs. 26 and 28 of Ref. 5. The first step is to express the pressure field from an acoustic point source in free space as an integral over plane waves. This type of formulation is attractive because the interaction of individual plane waves with planar interfaces is mathematically tractable and well understood.

We begin with the linear, scalar wave equation for the acoustic pressure  $p$  in a homogeneous medium of sound speed  $c$ :

$$\nabla^2 p = \frac{1}{c^2} \frac{\partial^2 p}{\partial t^2} \quad (2-1)$$

We consider the following solution to Eq. (2-1), which represents the field due to a harmonic point source at the origin of a Cartesian coordinate system:

$$p(x, y, z) = p_0 \frac{e^{i(kR - \omega t)}}{R}, \quad \text{where } R = \sqrt{x^2 + y^2 + z^2} \neq 0 \quad (2-2)$$

The quantity  $p_0$  in Eq. (2-2) is a constant (in units pressure-distance) that gives the pressure at unit distance from the origin. After substituting Eq. (2-2) into Eq. (2-1), carrying out the partial derivatives with respect to  $t$ , and expressing the spatial derivatives in Cartesian coordinates, we obtain the scalar Helmholtz equation

$$\frac{\partial^2 p}{\partial x^2} + \frac{\partial^2 p}{\partial y^2} + \frac{\partial^2 p}{\partial z^2} + k^2 p = 0, \quad (2-3)$$

where the wavenumber is defined as  $k = \omega/c$ .

In order to derive a plane wave representation of the spherical wave in Eq. (2-2), we first write the pressure field in the  $z = 0$  plane as

$$p(x, y) = \frac{e^{ikr}}{r}, \quad \text{where } r = \sqrt{x^2 + y^2} \neq 0 \quad (2-4)$$

In Eq. (2-4), the  $e^{-i\omega t}$  time dependence of the field has been suppressed, and, for convenience, we have taken  $p_0$  to be unity. We now express the field in the  $(x, y)$  plane as a double Fourier integral over the transform variables  $(k_x, k_y)$ :

$$\frac{e^{ikr}}{r} = \iint_{-\infty}^{\infty} A(k_x, k_y) e^{i(k_x x + k_y y)} dk_x dk_y \quad (r \neq 0), \quad (2-5)$$

where

$$A(k_x, k_y) = \frac{1}{(2\pi)^2} \iint_{-\infty}^{\infty} \frac{e^{ikr}}{r} e^{-i(k_x x + k_y y)} dx dy \quad (2-6)$$

The integral in Eq. (2-6) is solved by converting from  $(x, y)$  coordinates to polar coordinates  $(r, \phi)$  and solving the two integrals analytically (see Ref. 5, pp. 228-229). The result is

$$A(k_x, k_y) = \frac{i}{2\pi \sqrt{k^2 - k_x^2 - k_y^2}} \quad (2-7)$$

Using Eqs. (2-5) and (2-7) in Eq. (2-4), we may write the pressure field in the  $z = 0$  plane as

$$p(x, y) = \iint_{-\infty}^{\infty} \frac{i}{2\pi \sqrt{k^2 - k_x^2 - k_y^2}} e^{i(k_x x + k_y y)} dk_x dk_y \quad (r \neq 0) \quad (2-8)$$

We now construct an expression for the spherical wave field *off* the  $z = 0$  plane by formally multiplying the integrand of Eq. (2-8) by  $e^{\pm ik_z z}$  for  $\pm z \geq 0$ :

$$p(x, y, z) = \iint_{-\infty}^{\infty} \frac{i}{2\pi \sqrt{k^2 - k_x^2 - k_y^2}} e^{i(k_x x + k_y y + k_z z)} dk_x dk_y \quad z \geq 0 \quad (2-9)$$

This "continuation" is valid because the integrand of Eq. (2-9), and therefore  $p$  itself, satisfies the Helmholtz equation (2-3) and reduces to Eq. (2-8) when  $z = 0$ . Substitution of Eq. (2-9) into the Helmholtz equation yields the relation

$$k_x^2 + k_y^2 + k_z^2 = k^2 \quad (2-10)$$

Recognizing the radical in Eq. (2-9) to be

$$k_z = \sqrt{k^2 - k_x^2 - k_y^2} \quad (2-11)$$

we may rewrite the expression for the spherical wave

$$p(x, y, z) = \frac{e^{ikR}}{R} = \iint_{-\infty}^{\infty} \frac{i}{2\pi k_z} e^{i(k_x x + k_y y + k_z z)} dk_x dk_y \quad z \geq 0 \quad (2-12)$$

The exponential term in Eq. (2-12) represents a plane wave whose direction is given by the three wave numbers  $k_x$ ,  $k_y$ , and  $k_z$ , the last of which is

dependent on the first two by way of Eq. (2-11) (see Fig. 2-1). Each point in the  $(k_x, k_y)$  plane can be viewed as representing a plane wave that contributes to the spherical wave representation in Eq. (2-12). The fraction in the integrand of Eq. (2-12) can be viewed as a weighting function for each plane wave. Points inside the circle of radius  $k$  in the  $(k_x, k_y)$  plane correspond to the usual, propagating (homogeneous) plane waves since, by Eq. (2-11),  $k_z$  is real. Points outside the circle correspond to "inhomogeneous" plane waves, for which  $k_z$  is imaginary. By substituting a positive imaginary value for  $k_z$  into the plane wave form  $e^{i(k_x x + k_y y + k_z z)}$ , it can be seen that inhomogeneous plane waves are attenuated in the positive  $z$ -direction. The inclusion of the inhomogeneous plane waves is necessary to mathematically complete the description of the spherical wave in terms of plane waves.

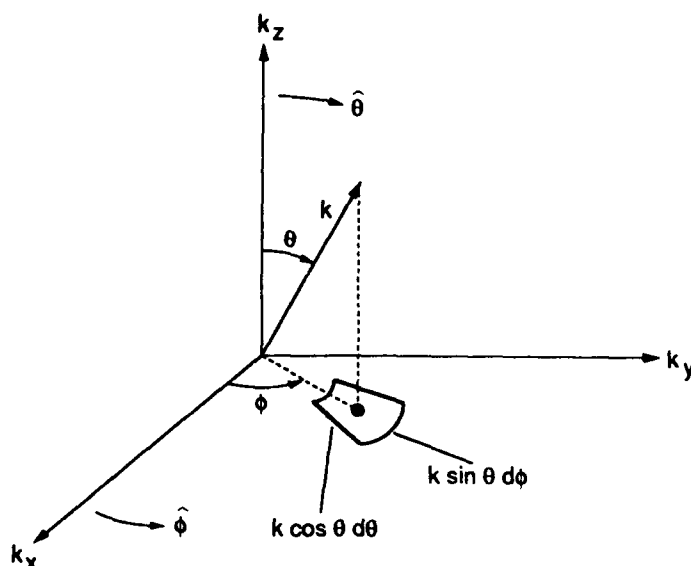


**Figure 2-1** CHANGE OF VARIABLE FROM RECTANGULAR COORDINATES  $(k_x, k_y, k_z)$  TO POLAR COORDINATES  $(k, \theta, \phi)$ . THE DIFFERENTIAL ELEMENT OF AREA IN THE  $(k_x, k_y)$  PLANE IS SHOWN.

We now convert the wave number coordinates from rectangular  $(k_x, k_y, k_z)$  to polar  $(k, \theta, \phi)$  by way of the relations

$$\begin{aligned} k_x &= k \sin \theta \cos \phi \\ k_y &= k \sin \theta \sin \phi \\ k_z &= k \cos \theta \end{aligned} \quad (2-13)$$

These relations are shown graphically in Fig. 2-1. From Fig. 2-1, the differential element of area  $dk_x dk_y$  transforms to

$$dk_x dk_y \leftrightarrow (k \sin \theta d\phi) (k \cos \theta d\theta) \quad , \quad (2-14)$$

where the first term reflects the  $\phi$ -dependence and the second term the  $\theta$ -dependence. To cover the whole  $(k_x, k_y)$  plane,  $\phi$  must vary from 0 to  $2\pi$ . The inside of the circle of radius  $k$  is covered when  $\theta$  varies from 0 to  $\pi/2$ , while the outside of the circle is covered when  $\theta$  varies from  $\pi/2$  to  $\pi/2 - i\infty$ . The imaginary part of  $\theta$  is chosen to go from 0 to  $-i\infty$  in order to make the amplitudes of the inhomogeneous plane waves in the integrand of Eq. (2-12) exponentially decreasing rather than increasing, which can be seen by writing

$$k_z = k \cos \theta = k \cos(\theta_R + i\theta_I) = k(\cos \theta_R \cosh \theta_I - i \sin \theta_R \sinh \theta_I) \quad . \quad (2-15)$$

For  $\theta_I$  negative,  $\text{Im}[k_z]$  is positive, and  $e^{ik_z z}$  represents an exponentially decreasing amplitude. Introducing the change of variables given by Eqs. (2-13) into Eq. (2-12) results in

$$p(x, y, z) = \frac{ik}{2\pi} \int_{\theta=0}^{\frac{\pi}{2} - i\infty} \int_{\phi=0}^{2\pi} e^{i(k_x x + k_y y + k_z z)} \sin \theta d\phi d\theta \quad z \geq 0 \quad , \quad (2-16)$$

where the dependence of  $k_x$ ,  $k_y$ , and  $k_z$  on  $\theta$  and  $\phi$  is summarized in Eqs. (2-13).

We consider now a point source  $S$  at coordinates  $(0, 0, z_s)$ , located a distance  $z_s$  above a plane interface separating two fluid media with sound speeds  $c$  and  $c_1$ , densities  $\rho$  and  $\rho_1$ , and wave numbers  $k$  and  $k_1$ , respectively (see Fig. 2-2). The field at a given receiver  $R$  at horizontal range  $r = \sqrt{x^2 + y^2}$  and height  $z_r$  above the interface is composed of a direct path contribution and a reflected contribution. The reflected pressure field  $p(r, z_t)$  at  $R$  is constructed by multiplying each of the plane waves in the integrand of Eq. (2-16) by the plane wave reflection coefficient  $V(\theta)$  and by taking into account the total vertical distance  $z_t = z_s + z_r$  each plane wave must travel:

$$p(r, z_t) = \frac{ik}{2\pi} \int_{\theta=0}^{\frac{\pi}{2} - i\infty} \int_{\phi=0}^{2\pi} e^{i(k_x x + k_y y + k_z z_t)} V(\theta) \sin \theta d\phi d\theta \quad . \quad (2-17)$$

The plane wave (Rayleigh) reflection coefficient for the fluid-fluid interface is

$$V(\theta) = \frac{m \cos \theta - \sqrt{n^2 - \sin^2 \theta}}{m \cos \theta + \sqrt{n^2 - \sin^2 \theta}} \quad , \quad (2-18)$$

where

$$n = c/c_1 \quad , \quad m = \rho_1/\rho \quad . \quad (2-19)$$

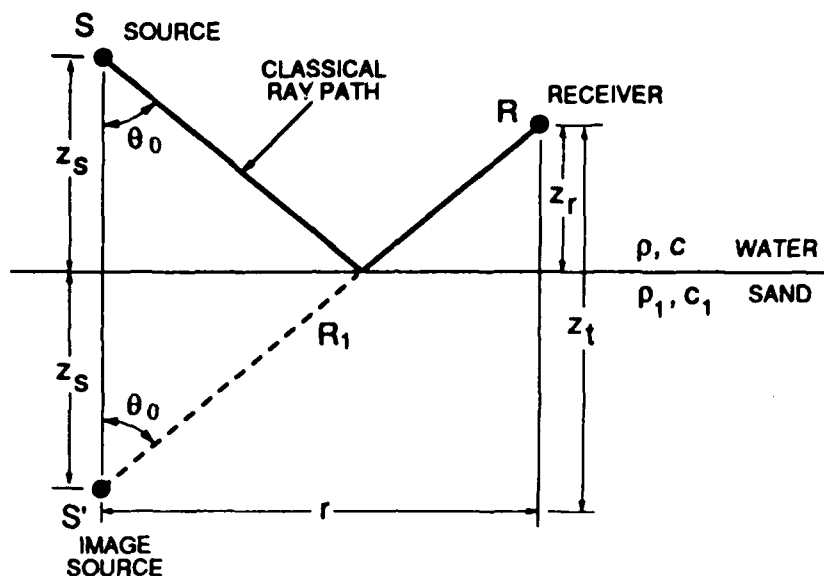


Figure 2-2 GEOMETRY FOR THE REFLECTED FIELD.

The critical angle introduced by  $V(\theta)$  is defined as

$$\theta_{cr} = \arcsin(c/c_1) = \arcsin(n) \quad (2-20)$$

The integral over  $\phi$  in Eq. (2-17) can be performed analytically by substituting for  $k_x$  and  $k_y$  from Eqs. (2-13) and expressing the receiver coordinates  $x$  and  $y$  in terms of polar coordinates  $r$  and  $\phi_1$ :

$$x = r \cos \phi_1 \quad y = r \sin \phi_1 \quad (2-21)$$

The result is

$$\begin{aligned} I_\phi &= \int_{\phi=0}^{2\pi} e^{i(k_x x + k_y y)} d\phi \\ &= \int_{\phi=0}^{2\pi} e^{i k r \sin \theta (\cos \phi_1 \cos \phi + \sin \phi_1 \sin \phi)} d\phi \\ &= \int_{\phi=0}^{2\pi} e^{i k r \sin \theta [\cos(\phi - \phi_1)]} d\phi \\ &= 2\pi J_0(kr \sin \theta) \quad (2-22) \end{aligned}$$

Introducing this result in Eq. (2-17), we obtain

$$p(r, z_t) = ik \int_0^{\frac{\pi}{2} - i\infty} J_0(kr \sin \theta) e^{ikz_t \cos \theta} V(\theta) \sin \theta d\theta \quad (2-23)$$

Equation (2-23) is an exact representation of the reflected pressure field. However, in order to apply the method of steepest descent, we need to manipulate the integral once more. We use the following identity<sup>14</sup> for the Bessel function:

$$\begin{aligned} J_0(u) &= (1/2) [H_0^{(1)}(u) + H_0^{(2)}(u)] \\ &= (1/2) [H_0^{(1)}(u) - H_0^{(1)}(-u)] \quad , \end{aligned} \quad (2-24)$$

where  $H_0^{(1)}$  and  $H_0^{(2)}$  are Hankel functions of the first and second kind, respectively, of order zero. After substituting Eq. (2-24) into Eq. (2-23), we obtain two integrals in terms of  $H_0^{(1)}$ . A change of variable from  $\theta$  to  $-\theta$  is then introduced into the second of the two integrals. Since  $V(\theta)$  and  $\cos \theta$  are even functions and  $\sin \theta$  is an odd function, the resulting integrand is the same as that of the first integral, but the integration runs from  $-\pi/2 + i\infty$  to 0. Therefore the two integrals may be added together by simply combining the limits of integration:

$$p(r, z_t) = \frac{ik}{2} \int_{-\pi/2 + i\infty}^{\pi/2 - i\infty} H_0^{(1)}(kr \sin \theta) e^{ikz_t \cos \theta} V(\theta) \sin \theta d\theta \quad . \quad (2-25)$$

The contour of integration in the complex  $\theta$ -plane is shown in Fig. 2-3.

The first approximation introduced into Brekhovskikh's analysis is the use of the asymptotic expansion for the Hankel function

$$H_0^{(1)}(kr \sin \theta) \sim \sqrt{\frac{2}{\pi kr \sin \theta}} e^{-i\pi/4} e^{ikr \sin \theta} \quad . \quad (2-26)$$

Substituting for the Hankel function in Eq. (2-25), we obtain

$$p(r, z_t) = \sqrt{\frac{k}{2\pi r}} e^{i\pi/4} \int_{-\pi/2 + i\infty}^{\pi/2 - i\infty} e^{ik(r \sin \theta + z_t \cos \theta)} V(\theta) \sqrt{\sin \theta} d\theta \quad , \quad (2-27)$$

valid for large  $kr \sin \theta$ . Although the contour of integration for Eq. (2-27) passes through  $\theta = 0$ , where the above condition clearly is not satisfied, we shall see in Sec. 2-5 that in the application of the method of steepest descent, the contour of integration is deformed in such a way that it does not pass through  $\theta = 0$ . The condition of large  $kr \sin \theta$  is also not satisfied at short ranges  $r$ ; this issue will be discussed in Sec. 2-7.2.

Recognizing from Fig. 2-2 that  $r = R_1 \sin \theta_0$  and  $z_t = R_1 \cos \theta_0$ , we may write the reflected pressure field as

$$p(\theta_0, R_1) = \sqrt{\frac{k}{2\pi r}} e^{i\pi/4} \int_{-\pi/2 + i\infty}^{\pi/2 - i\infty} e^{ikR_1 \cos(\theta - \theta_0)} V(\theta) \sqrt{\sin \theta} d\theta \quad , \quad (2-28)$$

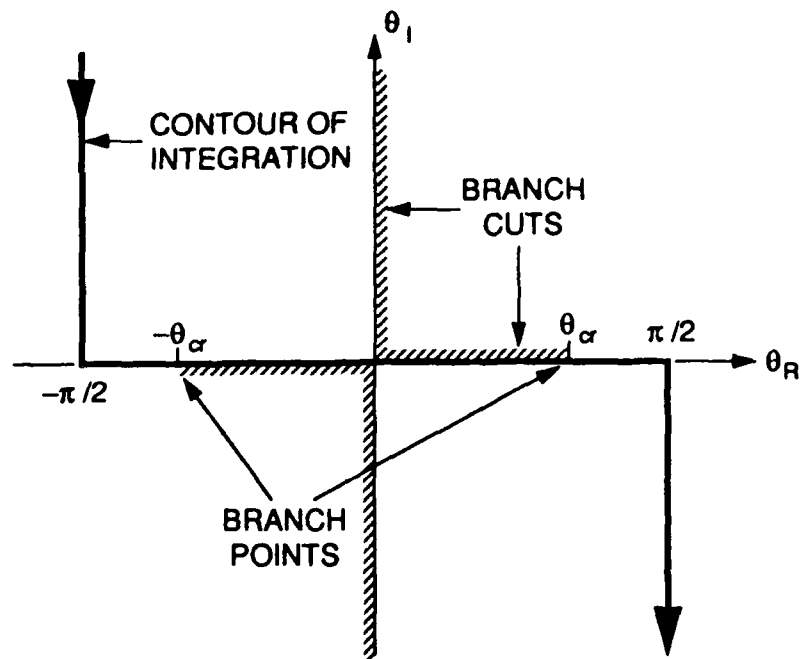


**Figure 2-3** CONTOUR OF INTEGRATION IN THE COMPLEX  $\theta$ -PLANE FOR THE REFLECTED FIELD INTEGRAL EQ. (2-25). ALSO SHOWN ARE THE BRANCH POINTS (AT  $\pm\theta_{cr} = \pm \arcsin(n)$ ) AND BRANCH CUTS INTRODUCED BY  $V(\theta)$ .

where the receiver position is now specified by the incident angle  $\theta_0$  and the distance  $R_1$  from the image source (see Fig. 2-2). Equation (2-28), finally, is the correct form of the integral for application of the method of steepest descent, which will be described next.

## 2-3 THE METHOD OF STEEPEST DESCENT

### 2-3.1 General formulation

The method of steepest descent (see Ref. 5, Sec. 27) is used to approximate integrals of the form

$$I = \int_C e^{\rho f(\theta)} F(\theta) d\theta \quad , \quad (2-29)$$

where  $C$  is a general contour in the complex  $\theta$ -plane,  $\rho$  (unrelated to the density in  $m$ ) is real, and  $f(\theta)$  and  $F(\theta)$  are analytic functions of the complex variable  $\theta$ .<sup>\*</sup> The method of steepest descent consists of three basic steps: (1) finding one or more saddle points, (2) deforming the path of integration into the steepest descent path(s), and (3) estimating the value of the integral. Saddle points are important because they mark particular regions of the complex  $\theta$ -plane where the integrand makes a distinct contribution to the integral. The path of integration is deformed into the path of steepest descent (which, by definition, passes through the saddle point) because the contribution to the integral is made over a relatively short interval. To obtain an estimate of the integral, the integrand is replaced by its Taylor series expansion about the saddle point, and the simpler integral that results is then performed analytically. In our applications of the method of steepest descent to acoustic field integrals, we find that saddle points represent eigenray angles.

Saddle points, which we will call  $\gamma$  throughout this work, are defined by the criterion

$$f'(\theta) = 0 \quad \text{at } \theta = \gamma \quad , \quad (2-30)$$

where prime indicates differentiation with respect to  $\theta$ . Expressing the phase function  $f$  in terms of its real and imaginary parts

$$f(\theta) = f_R(\theta) + i f_I(\theta) \quad , \quad (2-31)$$

we define the steepest descent path as the path in the complex  $\theta$ -plane that passes through the saddle point  $\gamma$ , and along which  $f_R$  decreases most rapidly. By the

---

<sup>\*</sup>We will often refer to  $f(\theta)$  as the "phase function," with the understanding that it is actually related to the phase of the exponential by the constant factor  $i/\rho$ .

properties of the real and imaginary parts of an analytic function,  $f_I$  remains constant along the path of steepest descent of  $f_R$ . Since

$$e^{\rho f(\theta)} = e^{\rho f_R(\theta)} e^{i\rho f_I(\theta)} \quad , \quad (2-32)$$

we see that along the steepest descent path the amplitude of the exponential decreases rapidly as one moves away from the saddle point, while the phase remains constant. Mathematically, the steepest descent path is defined by

$$f(\theta) = f(\gamma) - s^2 \quad , \quad (2-33)$$

where  $s$  is a real number that parameterizes the path.

To obtain an approximation to the integral, we equate a Taylor series expansion for  $f(\theta)$  about the saddle point  $\gamma$  to the steepest descent path definition in Eq. (2-33):

$$\begin{aligned} f(\theta) &= f(\gamma) - s^2 \\ &= f(\gamma) + f'(\gamma)(\theta - \gamma) + \frac{1}{2}f''(\gamma)(\theta - \gamma)^2 + \dots \quad , \end{aligned} \quad (2-34)$$

where the second term in the Taylor series is zero due to the saddle point definition Eq. (2-30). Keeping only the terms shown and solving for  $s$  in terms of  $\theta$ , we obtain the change of variable

$$s = \sqrt{\frac{-f''(\gamma)}{2}} (\theta - \gamma) \quad . \quad (2-35)$$

The change of variable in Eq. (2-29) yields

$$I = \sqrt{\frac{2}{-f''(\gamma)}} \int_{-\infty}^{\infty} e^{\rho[f(\gamma) - s^2]} F(s) ds \quad . \quad (2-36)$$

Note that the integrand is small at all values of  $s$  except in the neighborhood of  $s = 0$ . If we assume  $F(s)$  is slowly varying in this neighborhood,  $F(s = 0) = F(\gamma)$  can be brought outside the integral, leaving only the definite integral

$$\int_{-\infty}^{\infty} e^{-\rho s^2} ds = \sqrt{\pi/\rho} \quad . \quad (2-37)$$

The first order saddle point approximation to the integral is, then,

$$I = \sqrt{\frac{2\pi}{-\rho f''(\gamma)}} e^{\rho f(\gamma)} F(\gamma) \quad . \quad (2-38)$$

The correct sign of the square root in Eq. (2-38) is found by considering Eq. (2-35) and verifying that  $s$  is positive in the forward direction of integration from the saddle point. In the case at hand, the real part of the radical should be positive. Brekhovskikh derives higher order approximations in Sec. 27 of Ref. 5. Additional terms include factors of  $\rho^{-\frac{1}{2}}$ ,  $\rho^{-\frac{3}{2}}$ , and so forth.

### 2-3.2 Classical ray theory

A straightforward application of the method of steepest descent to the integral for the reflected field in Eq. (2-28) yields a result consistent with classical ray theory. In terms of the parameters given in Eq. (2-29), we rewrite Eq. (2-28)

$$p(\theta_0, R_1) = \sqrt{\frac{k}{2\pi r}} e^{i\frac{\pi}{4}} \int_{-\frac{\pi}{2}+i\infty}^{\frac{\pi}{2}-i\infty} \exp\left\{\underbrace{\{kR_1\}}_{\rho} \underbrace{\{i \cos(\theta - \theta_0)\}}_{f(\theta)}\right\} \underbrace{V(\theta) \sqrt{\sin \theta}}_{F(\theta)} d\theta, \quad (2-39)$$

where

$$\rho = kR_1 \quad (2-40a)$$

$$f(\theta) = i \cos(\theta - \theta_0) \quad (2-40b)$$

$$F(\theta) = V(\theta) \sqrt{\sin \theta} \quad (2-40c)$$

Upon setting  $f'(\gamma) = -i \sin(\gamma - \theta_0) = 0$ , we find the saddle point to be  $\gamma = \theta_0$ . Using the saddle point approximation in Eq. (2-38) and recalling that  $r = R_1 \sin \theta_0$ , we write the reflected pressure field

$$\begin{aligned} p(\theta_0, R_1) &= \sqrt{\frac{k}{2\pi r}} e^{i\frac{\pi}{4}} \sqrt{\frac{2\pi}{ikR_1}} e^{ikR_1} V(\theta_0) \sqrt{\sin \theta_0} \\ &= V(\theta_0) \frac{e^{ikR_1}}{R_1}, \end{aligned} \quad (2-41)$$

which represents the field due to a point source at the image  $S'$  (see Fig. 2-2), whose strength is multiplied by the factor  $V(\theta_0)$ . This solution expresses the reflected field in terms of spherically spreading rays that emanate from the (actual) source  $S$  and specularly reflect from the interface, acquiring the *plane wave* reflection coefficient factor  $V(\theta_0)$  in the process.

Comparisons between classical ray theory [Eq. (2-41)] and the exact solution [obtained by numerically integrating Eq. (2-23)] at various frequencies are shown in Fig. 2-4. The interface, typical of a water-sand interface, is characterized by  $n = 0.866$  ( $\theta_{cr} = 60.0^\circ$ ) and  $m = 1.67$ . The vertical axis is the magnitude of

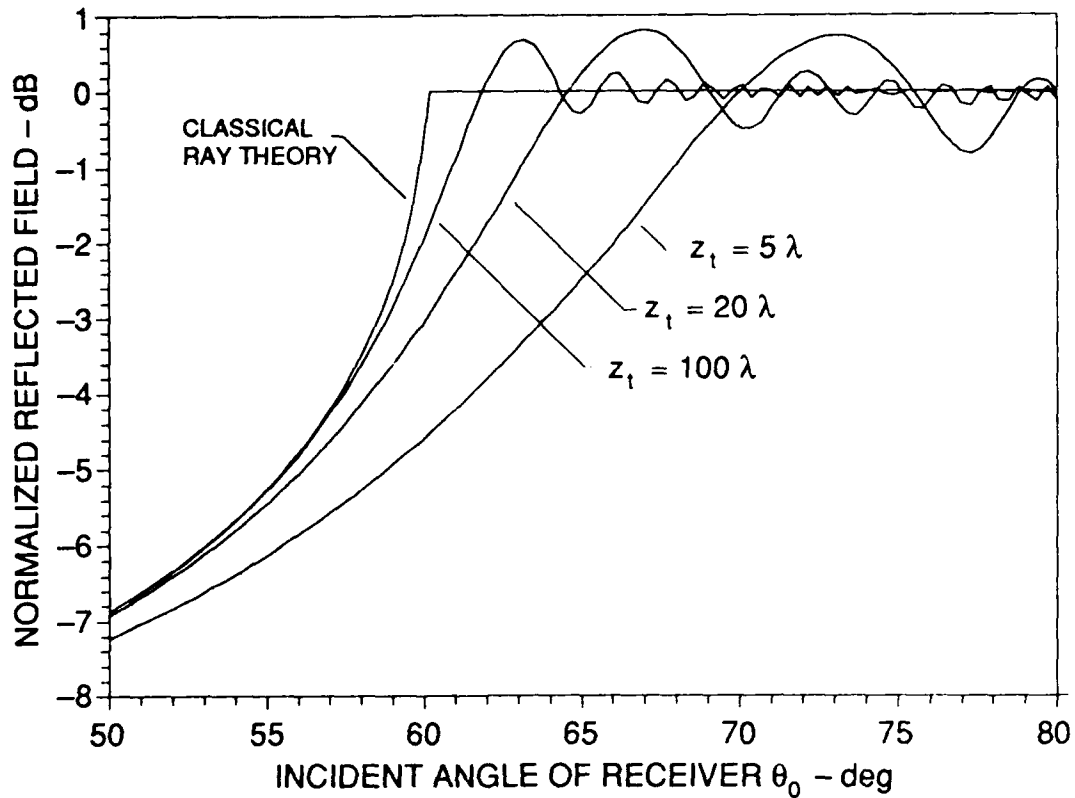


**Figure 2-4** COMPARISON BETWEEN CLASSICAL RAY THEORY [Eq. (2-41)] AND THE EXACT RESULT [Eq. (2-23)] FOR THE NORMALIZED REFLECTED FIELD. FOR EACH PLOT OF THE EXACT FIELD, THE VALUE OF  $z_t$  (SEE FIG. 2-2) IN WAVELENGTHS  $\lambda$  IS INDICATED. THE CRITICAL ANGLE LIES AT  $\theta_{cr} = 60.0^\circ$ .

the reflected pressure field in decibels (dB), where 0 dB corresponds to the field at unit distance from a point source in free space. The field in Fig. 2-4 has been normalized by removing the spherical wave factor  $e^{ikR_1}/R_1$  at each point. All that remains is the effect of the reflection process, which, according to classical ray theory, is just  $V(\theta_0)$  [see Eq. (2-41)]. The horizontal axis specifies receiver location by giving the angle of incidence  $\theta_0$  from the image source, where  $z_t$  in wavelengths  $\lambda$  is constant for each plot. Note that the classical ray result does not include the oscillations in the exact field at incident angles larger than critical. We will see in Sec. 2-5 that these oscillations are caused by interference between the totally reflected field and the lateral wave field. The largest error in classical ray theory occurs at the lowest frequency (smallest  $z_t$ ) and at angles close to the critical angle.

## 2-4 COMPLEX RAY FORMULATION

### 2-4.1 Rearrangement of the integral

In a variation on the method of steepest descent (Sec. 31.3, Ref. 5), Brekhovskikh allows the phase of the reflection coefficient to influence the locations of the saddle points. Expressing  $V$  in terms of its magnitude  $|V|$  and phase  $\phi_v$ , we may write Eq. (2-28)

$$p(\theta_0, R_1) = \sqrt{\frac{k}{2\pi r}} e^{i\frac{\pi}{4}} \int_{-\frac{\pi}{2}+i\infty}^{\frac{\pi}{2}-i\infty} e^{i[kR_1 \cos(\theta-\theta_0)+\phi_v(\theta)]} |V(\theta)| \sqrt{\sin \theta} d\theta \quad (2-42)$$

The phase function in the exponent of Eq. (2-29) is now

$$f(\theta) = i \cos(\theta - \theta_0) + \frac{i}{kR_1} \phi_v(\theta) \quad , \quad (2-43)$$

and the saddle point criterion is

$$f'(\theta) = -i \sin(\theta - \theta_0) + \frac{i}{kR_1} \phi'_v(\theta) = 0 \quad \text{at } \theta = \gamma \quad . \quad (2-44)$$

This formulation results in saddle points on the real axis, each of which corresponds to the angle of the eigenray that starts at the source and passes through the receiver. It is the formulation used in Refs. 9-11.

In the present work, we take Brekhovskikh's variation one step further by allowing both the *amplitude and phase* of the reflection coefficient to affect the saddle point location.\* To do this we express

$$V(\theta) = e^{\ln V(\theta)} \quad , \quad (2-45)$$

and rewrite Eq. (2-28)

$$p(\theta_0, R_1) = \sqrt{\frac{k}{2\pi r}} e^{i\frac{\pi}{4}} \int_{-\frac{\pi}{2}+i\infty}^{\frac{\pi}{2}-i\infty} e^{kR_1[i \cos(\theta-\theta_0)+\frac{1}{kR_1} \ln V(\theta)]} \sqrt{\sin \theta} d\theta \quad , \quad (2-46)$$

\*A careful reading of Sec. 31.3 of Ref. 5 suggests that Brekhovskikh may have intended just this step. He sets  $V(\theta) = e^{i\phi_v(\theta)}$  and states that "the phase coefficient of reflection can be a complex function." However, he does not consider complex saddle points, and later in the section he applies this formulation only to the case of total reflection, writing the phase  $\phi_v$  as a real quantity.

where the associations with Eq. (2-29) are now

$$\rho = kR_1 \quad (2-47a)$$

$$f(\theta) = i \cos(\theta - \theta_0) + \frac{1}{kR_1} \ln V(\theta) \quad (2-47b)$$

$$F(\theta) = \sqrt{\sin \theta} \quad (2-47c)$$

The saddle point criterion is

$$f'(\theta) = -i \sin(\theta - \theta_0) + \frac{1}{kR_1} \frac{V'(\theta)}{V(\theta)} = 0 \quad \text{at } \theta = \gamma \quad , \quad (2-48)$$

and the second derivative  $f''$ , which is needed for the saddle point approximation Eq. (2-38), is

$$f''(\theta) = -i \cos(\theta - \theta_0) + \frac{1}{kR_1} \frac{VV'' - (V')^2}{V^2} \quad (2-49)$$

The result of the rearrangement of the plane wave integral and reformulation of the saddle point criterion is that the saddle points  $\gamma$  are, in general, located at complex values of  $\theta$ . The motivation for incorporating  $V(\theta)$  into  $f(\theta)$  is that we want the saddle point criterion Eq. (2-48) to include the complicated effects that the reflection process introduces.

The saddle point approximation to the integral for the reflected field in Eq. (2-46) is obtained by substituting the appropriate quantities into Eq. (2-38). After simplification, we obtain

$$p(\theta_0, R_1) = \sqrt{\frac{\sin \gamma}{r}} \sqrt{\frac{1}{iR_1 f''(\gamma)}} V(\gamma) e^{ikR_1 \cos(\gamma - \theta_0)} \quad , \quad (2-50)$$

where  $f''$  is given in Eq. (2-49).

#### 2-4.2 Branch cuts in $V(\theta)$

The dependence of the plane wave reflection coefficient  $V$  on incident angle  $\theta$  is what makes the reflected field much more complicated than the simple classical ray theory result in Eq. (2-41). In particular, the square root term  $q(\theta) \doteq \sqrt{n^2 - \sin^2 \theta} \doteq \sqrt{\tilde{q}(\theta)}$  in Eq. (2-18) for  $V(\theta)$  introduces branch points and branch cuts in the complex  $\theta$ -plane. Branch points lie at values of  $\theta$  for which the radicand  $\tilde{q}$  is zero. It is easy to see that the branch points lie at

$$\theta = \pm \arcsin(n) = \pm \theta_{cr} \quad , \quad (2-51)$$

where  $\theta_{cr}$  is the critical angle. The branch cuts are chosen to be along lines for which  $\tilde{q}(\theta)$  lies on the positive real axis. This imposes the following two requirements:

$$\operatorname{Re}[\tilde{q}(\theta)] = n_R^2 - n_I^2 - (\sin^2 \theta_R \cosh^2 \theta_I - \cos^2 \theta_R \sinh^2 \theta_I) > 0 \quad (2-52a)$$

$$\operatorname{Im}[\tilde{q}(\theta)] = 2(n_R n_I + \sin \theta_R \cos \theta_R \sinh \theta_I \cosh \theta_I) = 0 \quad , \quad (2-52b)$$

where, to allow for the possibility of attenuation in either medium, the index of refraction is written as the complex number  $n = n_R + in_I$ . For the case of no attenuation ( $n_I = 0$ ), solution of Eqs. (2-52a) and (2-52b) for  $\theta$  results in the branch cuts shown in Fig. 2-3.

Since the square root operator is double valued, the evaluation of  $V(\theta)$  introduces two Riemann sheets, where

$$\operatorname{Im}[q(\theta)] \quad \begin{cases} > 0 & \text{on the upper Riemann sheet} \\ < 0 & \text{on the lower Riemann sheet} \end{cases} \quad (2-53)$$

The branch cuts are significant in our problem because in order to keep the function  $q(\theta)$  [and therefore  $V(\theta)$ ] continuous, one must change Riemann sheets when an integration path crosses a branch cut.

The contour of integration for the reflected field integral Eq. (2-46) begins on the upper Riemann sheet at  $\theta = -\pi/2 + i\infty$  and ends on the upper Riemann sheet at  $\theta = \pi/2 - i\infty$ . By Cauchy's theorem the original contour may be deformed into the steepest descent path as long as no singularities are crossed in the deformation and the path starts and ends on the correct sheets at the correct points. Therefore, when applying the method of steepest descent, it is essential to verify that the deformed path of integration, which may cross the branch cuts one or more times, is equivalent to the original contour. When the steepest descent path of a saddle point ends on the wrong sheet, we must locate another saddle point whose path completes the required contour.

## 2-5 SADDLE POINT STRUCTURE OF THE REFLECTED FIELD

The saddle points and steepest descent paths for the reflected field along a horizontal line are shown in Fig. 2-5. The interface is characterized by  $\theta_{cr} = 60^\circ$  and  $m = 1.67$ . The source-receiver geometry is characterized by  $z_t = 5\lambda$ , and  $\theta_0$  is varied from  $50^\circ$  to  $80^\circ$  in increments of  $2.5^\circ$ . The saddle point angles  $\gamma$  [obtained by numerically solving Eq. (2-48)] as a function of receiver position (given by  $\theta_0$ ) are indicated by the bold dots. Each saddle point represents the angle at which an eigenray arrives at the receiver. The physical picture of the eigenray paths for

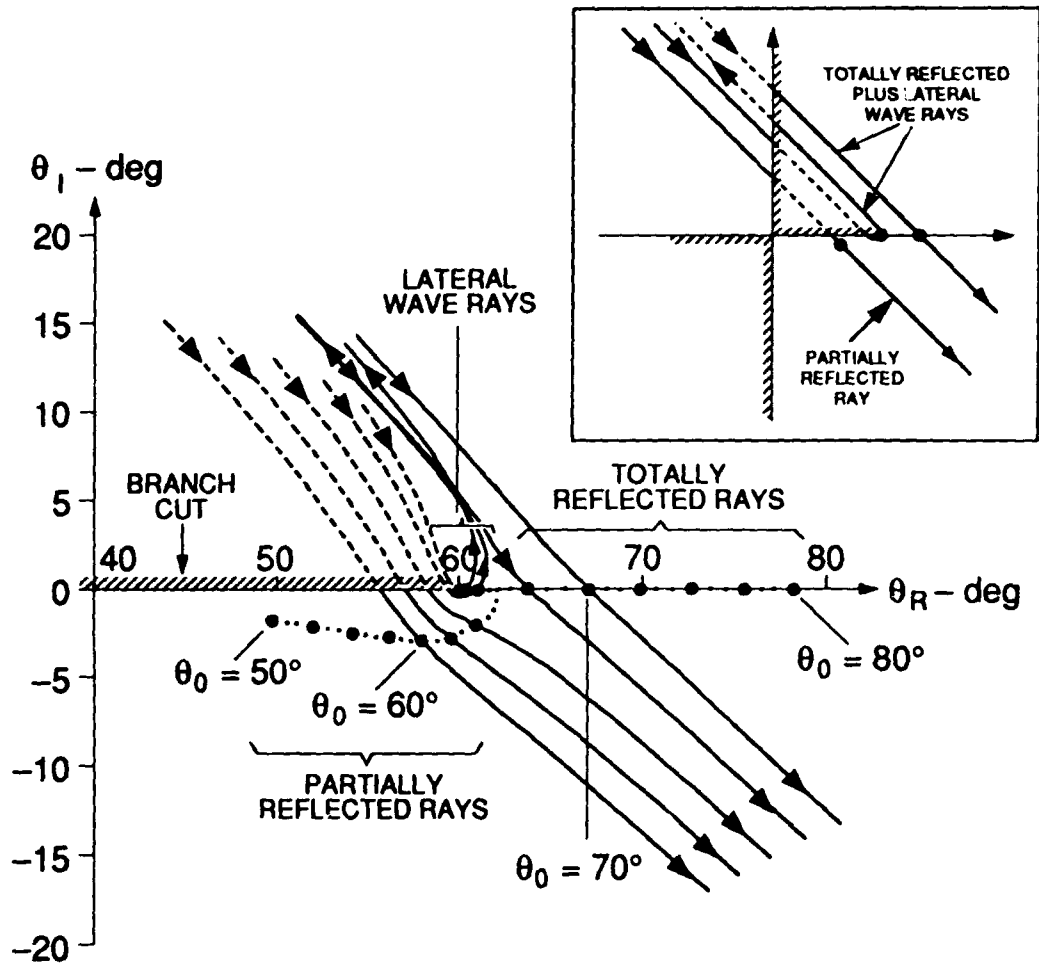


**Figure 2-5** SADDLE POINTS AND STEEPEST DESCENT PATHS FOR THE REFLECTED FIELD. THE GEOMETRY IS DESCRIBED IN THE TEXT, AND THE INTERFACE IS THE SAME AS IN FIG. 2-4. STEEPEST DESCENT PATHS ARE SHOWN FOR THE SADDLE POINTS IN THE REGION OF THE CRITICAL ANGLE. DASHED PORTIONS LIE ON THE LOWER RIEMANN SHEET. THE INSET ILLUSTRATES THE COMPLETION OF THE REQUIRED CONTOUR OF INTEGRATION FOR THE TWO BASIC CASES.

both the reflected and transmitted fields is shown in Fig. 2-6. For small  $\theta_0$  (short ranges) the field is made up of a single partially reflected eigenray. For large  $\theta_0$  (long ranges) the field is made up of a totally reflected eigenray plus a lateral wave eigenray. The origin of the lateral wave will be discussed shortly.

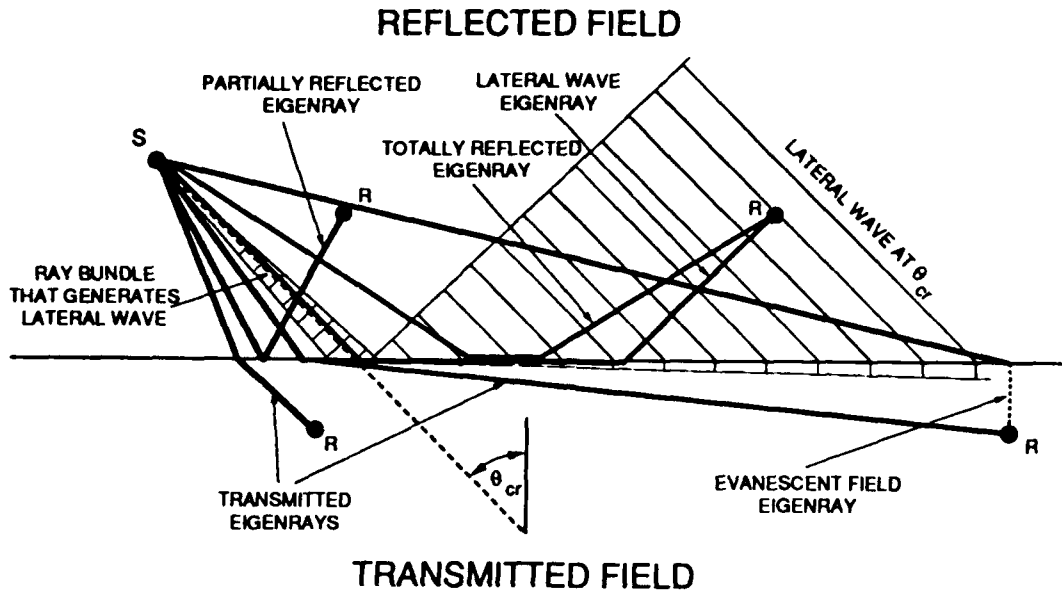


**Figure 2-6** EIGENRAY PICTURE FOR THE REFLECTED FIELD IN THE UPPER MEDIUM (SEE SEC. 2-5) AND TRANSMITTED FIELD IN THE LOWER MEDIUM (SEE SEC. 2-8.2).

Recall that classical ray theory predicts saddle points to lie at  $\gamma = \theta_0$ . However, from Fig. 2-5 we see that saddle points of the partially reflected eigenrays are complex, lying slightly below and to the left of  $\theta_0$ , and that saddle points of the totally reflected eigenrays lie on the real  $\theta$ -axis, but at angles noticeably smaller than  $\theta_0$ . In Sec. 2-7 we will see that these shifts in eigenray angle away from  $\theta_0$  are due to displacements in the ray trajectories along the interface upon reflection, as shown in Fig. 2-6. Finally, saddle points of the lateral wave eigenrays lie next to the critical angle. As the horizontal range to the receiver increases, the lateral wave saddle points move closer and closer to the critical angle. There are 6 lateral wave ray saddle points in Fig. 2-5 (to match the 6 totally reflected ray saddle points), but since they all lie very close to  $\theta_{cr}$ , it is not possible to draw them distinctly.

Steepest descent paths are shown for the saddle points in the region of the critical angle.\* The paths of the first seven saddle points, corresponding to

\*The paths drawn in Fig. 2-5 are those along which the numerical integration technique,

partially reflected eigenrays, cross the branch cut on the real  $\theta$ -axis. Since these paths cross the branch cut again on the positive imaginary axis (see inset of Fig. 2-5), they begin on the correct (upper) Riemann sheet and thereby complete the required contour. However, the path of the first totally reflected eigenray, for the receiver at  $\theta_0 = 67.5^\circ$ , does *not* cross the branch cut on the real axis, so it begins on the *wrong* (lower) Riemann sheet.<sup>†</sup> At this point it is necessary to seek an additional saddle point [an additional root of Eq. (2-48)] whose steepest descent path completes the contour. Such a saddle point is found on the real  $\theta$ -axis close to the branch point  $\theta_{cr} = 60^\circ$ . The saddle point represents the contribution from the lateral wave, and its steepest descent path loops around the branch point such that it starts on the upper Riemann sheet and ends on the lower Riemann sheet (see inset of Fig. 2-5). Thus, when the lateral wave ray and totally reflected ray are added together, their integration paths complete the required contour.

The physical interpretation of the lateral wave, illustrated in Fig. 2-6, is well known (see, for example, Sec. 30.2 of Ref. 5). It is generated by energy incident on the interface in the region of the critical angle. Some of this energy penetrates into the bottom and travels almost parallel to the interface at the bottom sound speed. Since the pressure across the interface must be continuous, the horizontally traveling energy in the bottom continuously excites a wave, the lateral wave, that travels at the critical angle in the water. The lateral wave arrives at all receivers that lie beyond a certain range from the source, and its wavefronts are conical about the  $S$ - $S'$  axis in Fig. 2-6.

The transition from a field composed of one saddle point at a complex angle (representing a partially reflected eigenray) to a field composed of two saddle points at real angles (representing the totally reflected eigenray and the lateral wave eigenray) occurs at a ray theory caustic. Caustics, which can be caused by the bending of rays as they are continuously refracted by a sound speed gradient in the medium, are points in space where two rays coalesce into one. In the present case, the caustic is caused by the reflection process, where two separate rays are formed upon reflection. When only considering rays with real angles, the caustic is the transition point between the shadow zone, into which no rays penetrate, and the insonified zone, where two rays arrive at every point. Mathematically, caustics are defined as saddle points [ $f'(\gamma) = 0$ ] at which  $f''(\gamma) = 0$ .

In Fig. 2-5 the caustic saddle point is recognized as the point where the totally reflected rays merge with the lateral wave rays ( $\gamma_c \approx 62^\circ$ ). The location

---

described in Sec. 2-6, is performed.

<sup>†</sup>Although the transition from total to partial reflection is, in reality, a gradual process, we use this criterion of steepest descent paths crossing, or not crossing, the branch cut to distinguish between partially and totally reflected rays.

of the caustic in *physical space* is given by  $z_c = 5\lambda$  and  $\theta_0 \approx 66.5^\circ$  (obtained by interpolating between the value of  $\theta_0 = 65^\circ$  for the last partially reflected ray shown and  $\theta_0 = 67.5^\circ$  for the first totally reflected ray shown). Since  $f''(\gamma_c) = 0$ , the saddle point approximation for the field given by Eq. (2-50) is infinite at the caustic. In the following subsection we summarize our method for finding the field in such regions where Eq. (2-50) is invalid.

Attenuation in the bottom can be included by introducing an imaginary part to the sound speed  $c_1$ .<sup>\*</sup> As a result, the index of refraction  $n = c/c_1$  in Eq. (2-18) is complex, the critical angle  $\theta_\alpha = \arcsin(n)$  acquires a positive imaginary part, and the saddle points are shifted. Figure 2-7 is the same as Fig. 2-5, except the lower medium has an attenuation of  $\alpha_{dB} = 0.5$  dB/ $\lambda$ . Notice that in this case there is a smooth transition between the partially reflected and the totally reflected ray saddle points. Since there is no receiver location where two saddle points coalesce into one, there is no caustic. The lateral wave saddle points have followed  $\theta_\alpha$  (the branch point) off the real axis, and the corresponding eigenrays suffer attenuation as they travel along the interface in the bottom. The totally reflected ray saddle points have a small negative imaginary part, and the eigenrays are attenuated to a lesser degree.

## 2-6 COMPUTATION OF THE EIGENRAY FIELD

The saddle point approximation in Eq. (2-50) is based on the assumption that, in the neighborhood of  $\gamma$ , the phase function  $f(\theta)$  is quadratic and the steepest descent path is a straight line in the complex  $\theta$ -plane. But this assumption is invalid when there is significant curvature in the steepest descent path (see, for example, Fig. 2-5). At the caustic itself, Eq. (2-50) predicts an infinite eigenray magnitude.

One way to find the correct field in the caustic region would be to apply caustic corrections that are based on uniform asymptotic expansions.<sup>11,16</sup> However this approach is not attractive for several reasons. First, it is difficult to smoothly join the shadow-zone field with the field due to the partially reflected rays. Second, the asymptotic expansions become extremely cumbersome as one is forced to include higher order terms. In our case, low frequencies and the proximity of the caustic to the singularity at the critical angle would make the calculation of higher order terms necessary.

---

<sup>\*</sup>This procedure is summarized in Sec. A8.4 of Ref. 15. We define a complex sound speed  $c = c_R + ic_I$ . For small attenuations, we set the imaginary part  $c_I = -[(\ln 10)/(40\pi)]c_R\alpha_{dB}$ , where  $c_R$  is the usual (real) sound speed and  $\alpha_{dB}$  is the attenuation in the medium in units dB/ $\lambda$ .

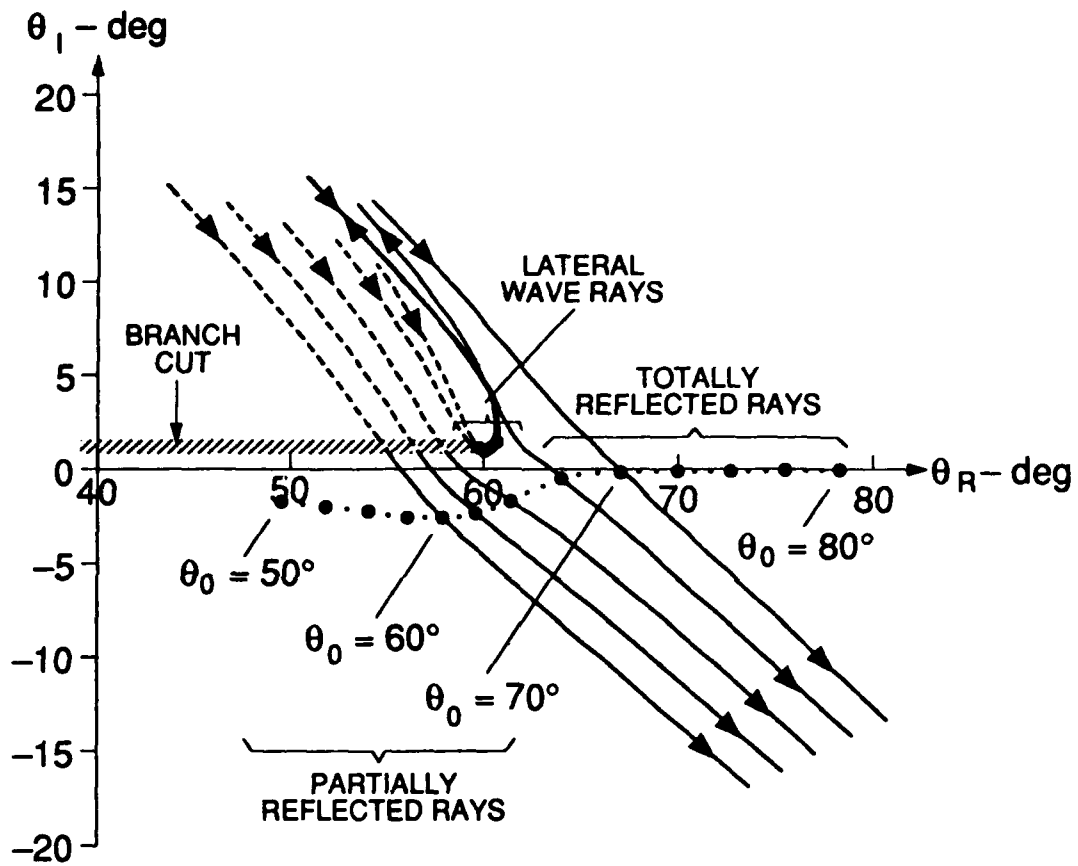


Figure 2-7 As in FIG. 2-5, EXCEPT  $n = 0.866 + i0.009$ , CORRESPONDING TO AN ATTENUATION OF  $0.5 \text{ dB}/\lambda$  IN THE LOWER MEDIUM.

To find the eigenray field for saddle points in the region of the critical angle we simply integrate numerically along the steepest descent path. The advantages of this technique are that it works at any frequency, it can be used to determine when more than one saddle point must be found, and it can be applied to any integrand for which the phase function  $f$  and its derivatives  $f'$  and  $f''$  can be computed.

Points along the steepest descent path are found sequentially, working away from the saddle point in one direction, then the other. The procedure is to determine desired values of  $f$  along the path, and then use a Taylor series for  $f$  to obtain an initial guess for each successive  $\theta$  point on the path. The first-order Taylor series at the previous point  $\theta_p$  on the steepest descent path is

$$f(\theta) = f(\theta_p) + f'(\theta_p)(\theta - \theta_p) \quad . \quad (2-54)$$

Given a desired value of  $f(\theta)$  at the next point on the path,  $f_d$ , the initial guess,  $\theta_g$ , is obtained by solving Eq. (2-54):

$$\theta_g = \theta_p + [f_d - f(\theta_p)] / f'(\theta_p) \quad . \quad (2-55)$$

At the saddle point itself,  $\theta_p = \gamma$  and  $f'(\theta_p) = 0$ , so a second-order Taylor expansion is needed. The result is

$$\theta_g = \gamma + \sqrt{2[f_d - f(\gamma)] / f''(\gamma)} \quad , \quad (2-56)$$

where the real part of the square root term is chosen to be positive in the forward direction of integration and negative in the opposite direction.

The remaining question is how to choose the desired values  $f_d$ . The imaginary part of  $f_d$  must be held constant at  $f_I(\gamma)$ , the value at the saddle point, in order to keep the phase of the exponential constant at  $\rho f_I(\gamma)$  [see Eq. (2-32)]. The real part of  $f_d$  is chosen so as to sample the amplitude of the exponential factor at desired levels, referenced to the maximum of  $A_{max} = e^{\rho f_R(\gamma)}$  at the saddle point. For example, if the first sample away from the saddle point is desired to have an amplitude of  $0.99A_{max}$ , then we would set

$$\text{Re}[f_d] = f_R(\gamma) + \ln(.99) / \rho \quad . \quad (2-57)$$

The desired levels at which to sample the amplitude factor are chosen so that a linear interpolation between samples gives a good approximation to a Gaussian, the approximate shape of the amplitude function along the steepest descent path. We use a total of 37 sample points in the numerical integration, resulting in an

error in the pressure field on the order of  $\pm 0.01$  dB. The end points of the integration paths drawn in Figs. 2-5 and 2-7 are determined by the criterion that the exponential factor have an amplitude of  $0.005A_{max}$  there. The integration algorithm must include special provisions for sections of paths that change direction rapidly, such as those associated with the lateral wave, which loop tightly around the critical angle.

The results using numerical integration along the steepest descent path for the cases in Fig. 2-4 are indistinguishable from the exact results shown. For the case of  $z_t = 5\lambda$ , the steepest descent method is approximately twice as efficient as the direct numerical integration of Eq. (2-23). However, the latter requires more sample points as the frequency is increased, while the number of sample points for the steepest descent method is *independent of frequency*. When the saddle point approximation can be used instead of steepest descent path integration, the efficiency of computing the field improves greatly.

It is difficult to determine from the saddle point characteristics alone how accurate the saddle point approximation is in a particular case. The method we employ is to begin in the area where the approximation is the poorest, the region of the critical angle, and work away from it in both directions. At each point we compare the result from steepest-descent integration with the saddle point approximation. When the latter is sufficiently close to the "exact" answer, we do not need to perform the numerical integration for any more receivers in that direction.

The accuracy of the method of numerically integrating along the path of steepest descent begins to deteriorate only when the frequency becomes extremely low. For  $z_t = 1\lambda$ , the steepest descent method differs from the exact solution [obtained by numerical integration of Eq. (2-23)] by less than 0.1 dB at all angles. For  $z_t < 0.5\lambda$ , we find that, instead of proceeding directly to the end point of the integration path at  $\pi/2 - i\infty$ , the steepest descent paths can end at the angle of intromission,  $\theta_{im}$ , where  $V(\theta_{im}) = 0$  and  $\text{Re}[f]$  approaches  $-\infty$ . For the interface considered in Fig. 2-5,  $\theta_{im} = 90^\circ - i21^\circ$ . In such cases, another saddle point that lies near  $\theta_{im}$  must be found. Its steepest descent path begins at  $\theta_{im}$  and ends in the correct direction, thus completing the contour of integration. In Sec. 2-8.2 and Fig. 2-12 we encounter a similar phenomenon for the transmission case, caused by the fact that the transmission coefficient is zero at a particular angle.

## 2-7 GEOMETRIC INTERPRETATION

### 2-7.1 Derivation of eigenray characteristics

One of the most attractive features of the saddle point approach is that the mathematical solution can be interpreted in terms of intuitive ray quantities, such as the path of propagation, the geometric spreading loss, the reflection loss, and the travel time. By moving the reflection coefficient  $V(\theta)$  into the phase function  $f$  in Eq. (2-46), we have incorporated the reflection process into the calculation of these ray characteristics.

The geometric interpretation of the ray path is shown in Fig. 2-8. The

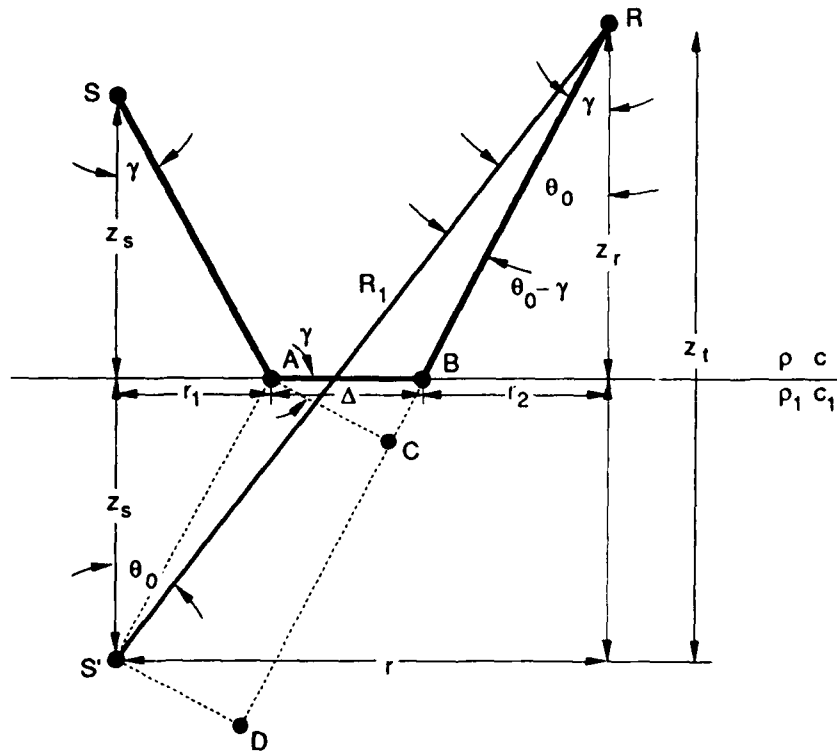


**Figure 2-8** EIGENRAY INTERPRETATION OF THE SADDLE POINT  $\gamma$  FOR THE REFLECTED FIELD

eigenray at angle  $\gamma$  is traced from the source  $S$  to the interface at  $A$  and backward from the receiver  $R$  to the interface at  $B$ . The resulting ray displacement  $\overline{AB}$  is defined as  $\Delta$ . Although the angle  $\gamma$  is, in general, complex, we can only draw it as a real angle. In cases where  $\gamma$  is complex, we must use trigonometric functions defined for complex arguments in the derivations that follow. The physical

interpretation of eigenrays with complex angles will be discussed in Sec. 2-7.3.

We begin by deriving the general form for the ray displacement  $\Delta$ . Using the geometrical relation

$$\sin(\gamma - \theta_0) = -\overline{S'D}/R_1 = -\Delta \cos \gamma / R_1 \quad (2-58)$$

in the saddle point criterion

$$f'(\gamma) = -i \sin(\gamma - \theta_0) + \frac{1}{kR_1} \frac{V'(\gamma)}{V(\gamma)} = 0 \quad (2-59)$$

we obtain

$$\Delta(\gamma) = \frac{i}{k \cos \gamma} \frac{V'(\gamma)}{V(\gamma)} \quad (2-60)$$

Equation (2-60) reduces to Brekhovskikh's result in Eq. 31.30 of Ref. 5 for the special case where  $\gamma$  is real and  $|V| = 1$  (total reflection). In this case,  $\Delta = -\phi'_v / (k \cos \gamma)$ , where  $\phi_v$  is the phase of  $V$ .

We can convert the saddle point criterion Eq. (2-59) to an eigenray equation by (1) substituting for  $V'/V$  in terms of  $\Delta$ , (2) expanding the  $\sin(\gamma - \theta_0)$  term, and (3) using the geometric relations  $R_1 \sin \theta_0 = r$  and  $R_1 \cos \theta_0 = z_s + z_r$ :

$$f'(\gamma) = -i(\sin \gamma \cos \theta_0 - \sin \theta_0 \cos \gamma) + \frac{1}{kR_1} (-ik\Delta \cos \gamma) = 0$$

$$\left( \frac{iR_1}{\cos \gamma} \right) f'(\gamma) = R_1 \cos \theta_0 \tan \gamma - R_1 \sin \theta_0 + \Delta \quad (2-61)$$

$$0 = (z_s \tan \gamma + \Delta + z_r \tan \gamma) - r \quad (2-62)$$

By Fig. 2-8, we interpret Eq. (2-62) as the eigenray equation

$$r = r_1(\gamma) + \Delta(\gamma) + r_2(\gamma) \quad (2-63)$$

Equation (2-63) gives the horizontal range  $r$  covered by a ray launched at complex angle  $\gamma$ . Note that any of the three intermediate range terms  $r_1$ ,  $\Delta$ , and  $r_2$  shown in Fig. 2-8 may be complex, but their sum must be the real quantity  $r$ .

Upon using the geometric relation (see Fig. 2-8)

$$R_1 \cos(\gamma - \theta_0) = \overline{DC} + \overline{CB} + \overline{BR} = \overline{SA} + \Delta \sin \gamma + \overline{BR} \quad (2-64)$$

for the phase factor in the saddle point approximation Eq. (2-50), we obtain the reflected field in terms of eigenray characteristics:

$$p(\theta_0, R_1) = \underbrace{\sqrt{\frac{\sin \gamma}{r}}}_{G_\phi} \underbrace{\sqrt{\frac{1}{iR_1 f''(\gamma)}}}_{G_\theta} \underbrace{V(\gamma)}_{\text{reflection loss}} \exp[i k (\overline{SA} + \Delta \sin \gamma + \overline{BR})] \quad (2-65)$$

ray path phase  $\Phi$

The factors  $G_\phi$  and  $G_\theta$  are geometric spreading factors and will be described in detail in the next section. The reflection loss factor in Eq. (2-65) is just the plane wave coefficient. The ray path phase  $\Phi$  shows that the ray travels along segments  $\overline{SA}$  and  $\overline{BR}$  at the water sound speed  $c$ , but along the interface at the speed

$$c_\Delta = c / \sin \gamma \quad (2-66)$$

Thus, lateral wave rays (see Sec. 2-5), for which  $\sin \gamma \approx \sin \theta_{cr} = c/c_1$ , travel the distance  $\Delta$  along the interface at the bottom sound speed, while rays at grazing incidence,  $\gamma = 90^\circ$ , travel at the water sound speed. Totally reflected rays, for which  $\theta_{cr} < \gamma < 90^\circ$ , travel at speeds somewhere between  $c$  and  $c_1$ .

### 2-7.2 Analysis of the geometric spreading factors

The first two factors in Eq. (2-65),  $G_\phi$  and  $G_\theta$ , are the geometric spreading factors in the two orthogonal directions  $\hat{\phi}$  and  $\hat{\theta}$  shown in Fig. 2-1. The spreading of a ray bundle in the  $\hat{\theta}$ -direction is illustrated in Fig. 2-9(a), which is drawn in the plane of incidence of the ray (the plane containing the ray and the normal to the interface). The bundle has width  $\Delta\theta$  and is centered about the eigenray angle  $\gamma$ . Its cross section at the receiver is  $r'(\gamma) \cos \gamma \Delta\theta$ , where  $r'$  is the derivative of  $r$  in Eq. (2-63) with respect to  $\gamma$ . Since the geometric loss is inversely proportional to the square root of the variation in the cross section of the bundle, we expect  $G_\theta = \sqrt{1/r'(\gamma) \cos \gamma}$ . This is indeed equivalent to the expression in Eq. (2-65) because differentiation of Eq. (2-61) results in the relation  $iR_1 f''(\gamma) = r'(\gamma) \cos \gamma$ . Carrying out the differentiation, one can express

$$G_\theta = \sqrt{\frac{1}{r'(\gamma) \cos \gamma}} = \sqrt{\frac{1}{\overline{SA} + \Delta' \cos \gamma + \overline{BR}}} \quad (2-67)$$

where

$$\Delta' = \frac{i}{k \cos \gamma} \frac{VV'' - (V')^2}{V^2} + \Delta \tan \gamma \quad (2-68)$$

Near the caustic Eq. (2-67) is invalid because  $r'$  approaches zero, and  $G_\theta$  therefore approaches infinity. In this case, the exact field  $p$  must be obtained by numerical integration along the steepest descent path. If desired, the value of  $G_\theta$  may be obtained by rearranging Eq. (2-65):

$$G_\theta = \frac{p(\theta_0, R_1)}{G_\phi V(\gamma) \exp(i\Phi)} \quad (2-69)$$

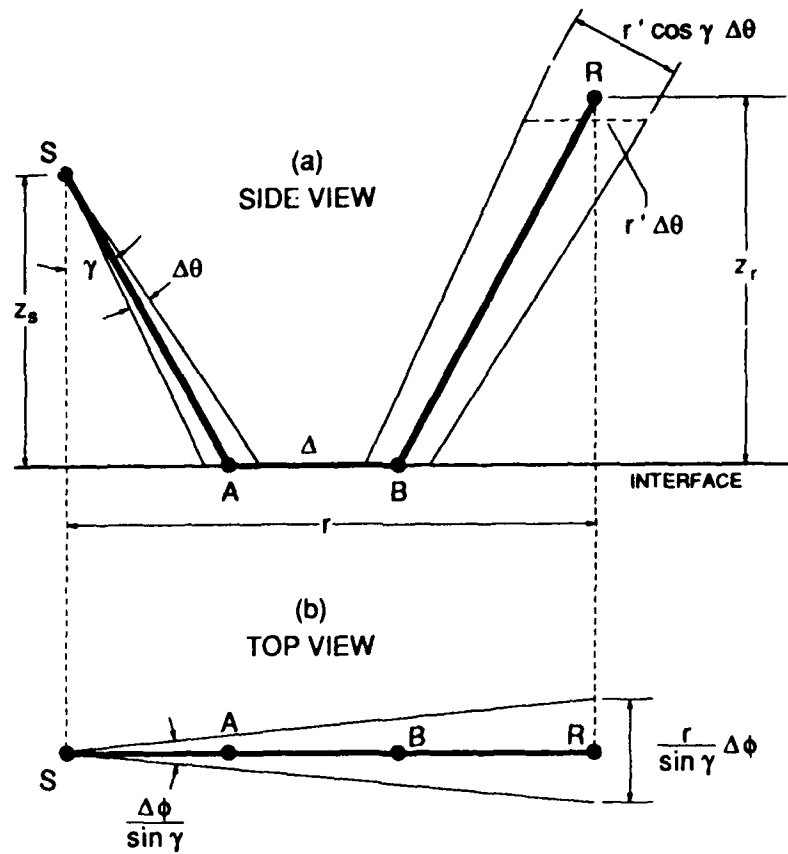


Figure 2-9 GEOMETRIC SPREADING OF AN EIGENRAY (a) IN THE  $\hat{\theta}$ -DIRECTION, AND (b) IN THE  $\hat{\phi}$ -DIRECTION.

The spreading of a ray bundle in the  $\hat{\phi}$ -direction is illustrated in Fig. 2-9(b). A ray bundle of angular width  $\Delta\phi$ , when projected on the plane of the interface, has angular width  $\Delta\phi/\sin\gamma$ . Cylindrical symmetry dictates that the center of curvature of the various portions of the ray path lie on the line through the source  $S$  and perpendicular to the interface. Thus, the (linear) cross section of the bundle at the receiver is simply  $r\Delta\phi/\sin\gamma$ . In terms of the path lengths along each segment of the ray trajectory,  $G_\phi$  can be expressed as

$$G_\phi = \sqrt{\frac{\sin\gamma}{r}} = \sqrt{\frac{1}{SA + \Delta/\sin\gamma + BR}} \quad (2-70)$$

Note that when the reflection coefficient is not a function of incident angle,  $\Delta = 0$  and  $G_\theta = G_\phi = \sqrt{1/R_1}$ . In such a case, the classical ray result Eq. (2-41) is exact.

At this point it is worthwhile to recognize the origin of the spreading loss factor  $G_\phi$ . The spreading in the  $\hat{\phi}$ -direction can be traced back to the change of variable in Eq. (2-14). The first factor on the right hand side of Eq. (2-14) accounted for the  $\phi$ -spreading and introduced the  $\sin\theta$  factor inside the double integral of Eq. (2-16). The integral over  $\phi$  eventually resulted in the Hankel function factor in Eq. (2-25), which was then replaced by its asymptotic form in Eq. (2-26). Combination of the asymptotic form of the Hankel function with the  $\sin\theta$  factor resulted in the factor  $\sqrt{\sin\theta/r}$ .

When viewed geometrically as in Fig. 2-9, it makes sense to separate the spreading factors in the two independent directions. This is achieved by evaluating the  $\hat{\phi}$ -spreading factor  $G_\phi = \sqrt{\sin\theta/r}$  at the saddle point  $\gamma$  and taking it outside the integral over  $\theta$  in Eq. (2-46), which accounts for the  $\hat{\theta}$ -spreading factor  $G_\theta$ . With the  $G_\phi$  factor removed, the Hankel function approximation ( $kr\sin\theta$  not small) no longer causes errors at short ranges and low frequencies. As we shall see in Chapter 3, separation of the two spreading factors in this way enables our basic method for evaluating the field to be extended to more complicated environments, where ray paths may have multiple reflections at possibly different angles of incidence.

### 2-7.3 Interpretation of complex eigenrays

As we have seen, saddle points, and therefore eigenray angles, can be complex. When  $\gamma$  is complex, the eigenray characteristics in Eq. (2-65) have non-zero imaginary parts that may not have a clear physical interpretation. When saddle points are complex due to attenuation in one or both media, as is the case for the saddle points representing the totally reflected and lateral wave rays

in Fig. 2-7, the imaginary parts of the eigenray characteristics may be viewed as simply accounting for the attenuation along the eigenray paths. However, even with no attenuation, partially reflected eigenray angles have small imaginary parts, as seen in Fig. 2-5. The largest imaginary parts of  $\gamma$  occur at receivers near  $\theta_0 = \theta_{cr}$ . The significance of the complex saddle points in this region is that the field does not behave like a simple (classical ray theory) ray field there. At lower frequencies (source and receiver closer to the interface in terms of wavelengths) the field in this region behaves less like a simple ray field, and the imaginary parts of the saddle points  $\gamma$  are correspondingly larger. Although we can assign no simple physical interpretation to complex-valued eigenray characteristics, we can deduce the approximate path of the energy the "ray" represents from the real part of the eigenray angle.

The possibility of complex-valued saddle points makes the process of "ray tracing" more difficult. An eigenray with a complex angle begins and ends in real space at the source and receiver, respectively, but otherwise travels through complex-valued spatial coordinates. Thus, in regions where eigenrays are complex, we may not use the usual practice of launching a series of real rays and tracing them through real space.

## 2-8 THE TRANSMITTED FIELD IN THE BOTTOM

In this section we solve for the transmitted field in the bottom using the same method used for the reflected field. After developing the plane wave integral for the field in the bottom, we summarize the saddle point structure and interpret the field in terms of eigenray characteristics.

### 2-8.1 Integral representation of the transmitted field

The derivation of the plane wave integral for the field at a point in the bottom begins with the representation of the spherical wave in Eq. (2-16). A plane wave incident on the interface at angle  $\theta$  is transmitted into the bottom at angle  $\theta_1$  according to Snell's law

$$\sin \theta_1 = \sin \theta / n \quad . \quad (2-71)$$

Figure 2-14 shows the geometrical configuration of the source and receiver. We express distances in the bottom as well as in the water in terms of the wavelength  $\lambda$  in the water.

The pressure field in the bottom is constructed by multiplying each plane wave in the integrand of Eq. (2-16) by the transmission coefficient  $W(\theta)$  and by

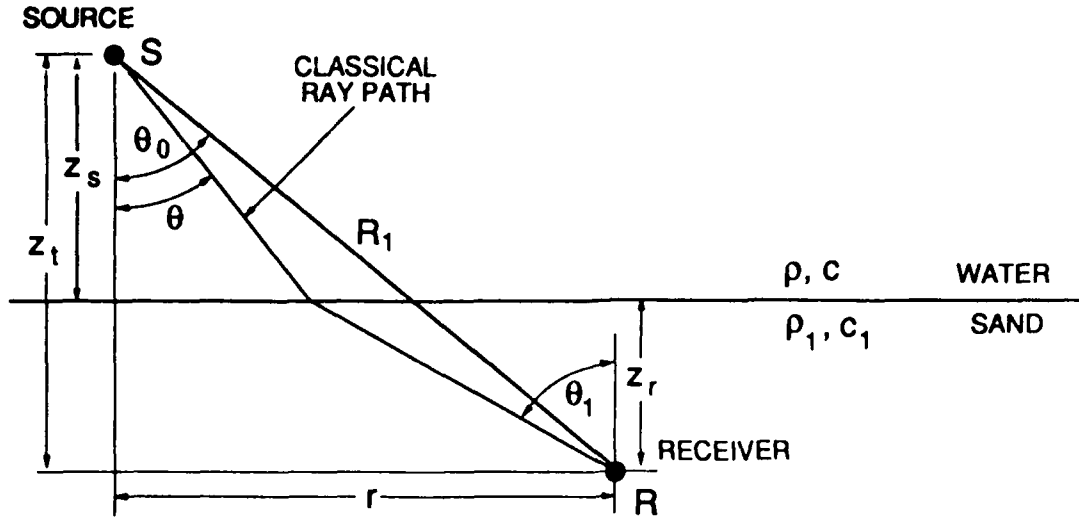


Figure 2-10 GEOMETRY FOR CALCULATION OF THE TRANSMITTED FIELD IN THE BOTTOM.

taking into account the total phase in the water  $k_z z_s$ , and in the bottom  $k_{1z} z_r$ :

$$p(r, z_s, z_r) = \frac{ik}{2\pi} \int_{\theta=0}^{\frac{\pi}{2}-i\infty} \int_{\phi=0}^{2\pi} e^{i(k_x x + k_y y + k_z z_s + k_{1z} z_r)} W(\theta) \sin \theta d\phi d\theta \quad , \quad (2-72)$$

where  $k_x$ ,  $k_y$ , and  $k_z$  are given in Eqs. (2-13),  $k_{1z} = k_1 \cos \theta_1$  is the vertical component of the wave number in the bottom, and the fluid-fluid plane wave transmission coefficient is

$$W(\theta) = \frac{2m \cos \theta}{m \cos \theta + \sqrt{n^2 - \sin^2 \theta}} \quad . \quad (2-73)$$

Following the derivation for the reflection case, we perform the integration over  $\phi$  analytically, with the result

$$p(r, z_s, z_r) = ik \int_0^{\frac{\pi}{2}-i\infty} J_0(kr \sin \theta) e^{i(k_z z_s + k_{1z} z_r)} W(\theta) \sin \theta d\theta \quad . \quad (2-74)$$

Next, we express the Bessel function in terms of Hankel functions and use the asymptotic form of the Hankel function. Finally, after rearrangement such that  $W(\theta)$  appears in the phase function, we obtain

$$p(\theta_0, R_1, z_r) = \sqrt{\frac{k}{2\pi r}} e^{i\frac{\pi}{4}} \int_{-\frac{\pi}{2}+i\infty}^{\frac{\pi}{2}-i\infty} \exp \left\{ kR_1 [i \cos(\theta - \theta_0) - \frac{iz_r}{R_1} (\cos \theta - n \cos \theta_1) + \frac{1}{kR_1} \ln W(\theta)] \right\} \sqrt{\sin \theta} d\theta \quad . \quad (2-75)$$

The integration contour and branch cuts are the same as for the reflection case in Fig. 2-3. The choice of the Riemann sheet [see Eq. (2-53)] applies to the term  $n \cos \theta_1 = \sqrt{n^2 - \sin^2 \theta} \doteq q$  in the exponent of Eq. (2-75) and in  $W(\theta)$ . Note that the transmitted field depends on  $z_r$  as well as  $\theta_0$  and  $R_1$ .

The phase function in the transmitted field integral Eq. (2-75) is

$$f(\theta) = i \cos(\theta - \theta_0) - \frac{iz_r}{R_1}(\cos \theta - n \cos \theta_1) + \frac{1}{kR_1} \ln W(\theta) \quad , \quad (2-76)$$

the saddle point criterion is

$$f'(\theta) = -i \sin(\theta - \theta_0) + \frac{iz_r}{R_1}(\sin \theta + q') + \frac{1}{kR_1} \frac{W'(\theta)}{W(\theta)} = 0 \quad \text{at } \theta = \gamma, \quad (2-77)$$

and the second derivative required by the saddle point approximation is

$$f''(\theta) = -i \cos(\theta - \theta_0) + \frac{iz_r}{R_1}(\cos \theta + q'') + \frac{1}{kR_1} \frac{WW'' - (W')^2}{W^2} \quad , \quad (2-78)$$

where

$$\begin{aligned} q' &= -\sin \theta \cos \theta / (n \cos \theta_1) \\ q'' &= [\sin^2 \theta - \cos^2 \theta - (q')^2] / (n \cos \theta_1) \quad . \end{aligned}$$

## 2-8.2 Saddle point structure of the transmitted field

The saddle points and steepest descent paths are found in a manner analogous to the reflection case. In Fig. 2-11 we show the situation in the complex  $\theta$ -plane for a low frequency case where  $z_s = 4\lambda$ ,  $z_r = 1\lambda$ , and the angle  $\theta_0$  specifying the receiver position is varied from  $50^\circ$  to  $80^\circ$  in increments of  $2.5^\circ$ . We see that for the seven receivers closest to the source, the steepest descent path for the transmitted ray completes the required contour of integration by itself. But for receivers farther from the source, the path turns back up and to the left instead of down and to the right. For these receivers the steepest descent path of an additional saddle point, corresponding to the evanescent field, completes the contour. The evanescent field is produced by energy that is totally reflected at the interface, but that nevertheless causes a disturbance in the bottom. The complex angle of the "evanescent ray" has a real part that is slightly greater than  $\theta_0$  and an imaginary part that is positive. The eigenray interpretation of the field in the bottom is shown in Fig. 2-6.

When the source and receiver are very close to the interface and somewhat far apart, a complication in the steepest descent path of the evanescent ray

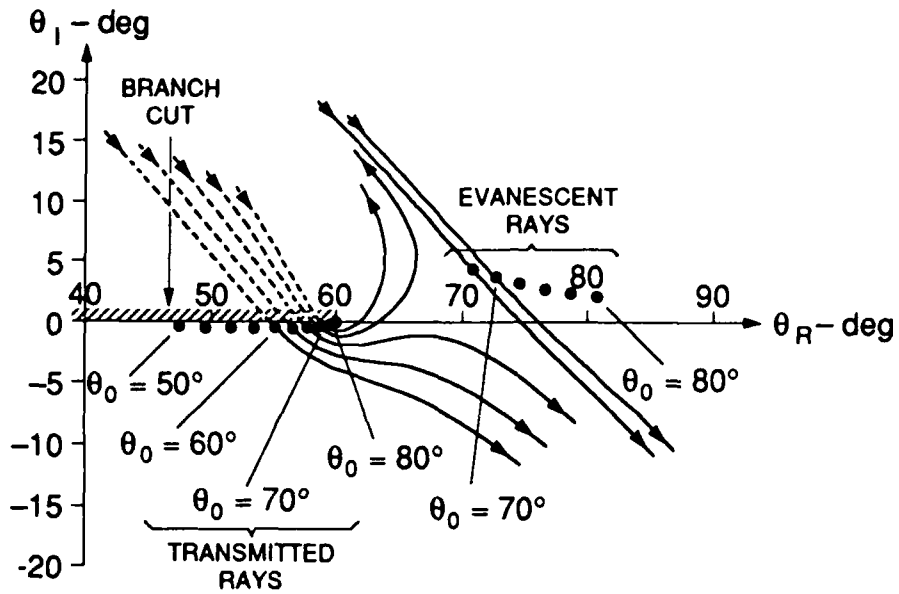


**Figure 2-11** SADDLE POINTS AND STEEPEST DESCENT PATHS FOR THE TRANSMITTED FIELD. THE GEOMETRY IS DESCRIBED IN THE TEXT, AND THE INTERFACE IS THE SAME AS IN FIG. 2-4.

saddle point can arise. Instead of ending in the correct direction, the path ends at  $\theta = 90^\circ + i0^\circ$ , where  $W$  by Eq. (2-73) is zero and  $\text{Re}[f]$  by Eq. (2-76) approaches  $-\infty$ . When this happens, we must search for an additional saddle point  $\gamma_{ev2}$  whose path of integration completes the required contour of integration (see Fig. 2-12). We call  $\gamma_{ev2}$ , which lies slightly below and to the right of  $90^\circ$  in the complex

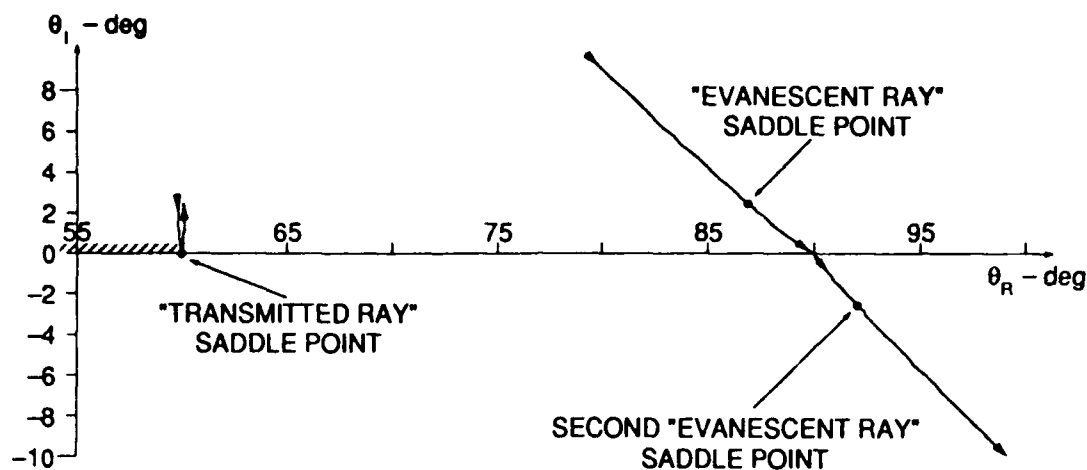
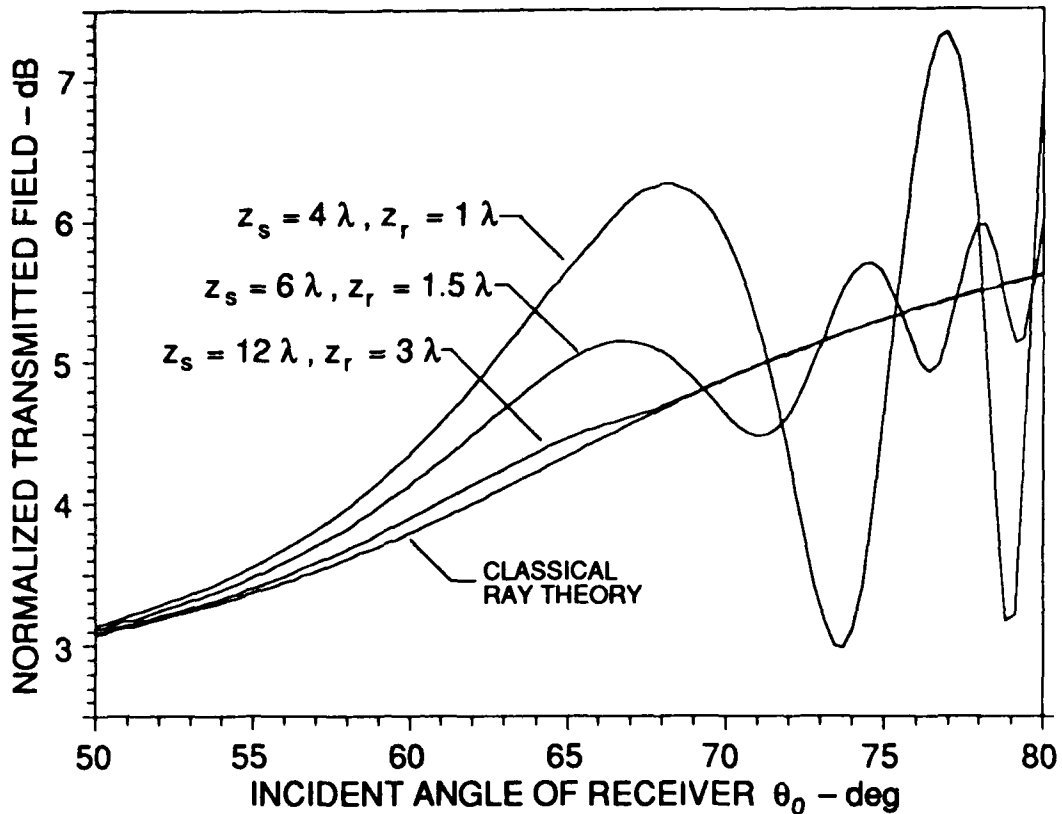


Figure 2-12 SADDLE POINTS AND STEEPEST DESCENT PATHS FOR A CASE WHERE AN ADDITIONAL "EVANESCENT RAY" SADDLE POINT MUST BE FOUND. THE PARAMETERS ARE:  $n = 0.866$ ,  $m = 1.67$ ,  $z_s = z_r = 0.25\lambda$ ,  $r = 40\lambda$ .

$\theta$ -plane, a second "evanescent ray" saddle point because it represents an inhomogeneous plane wave that travels parallel to the interface ( $\text{Re}[\gamma_{ev2}] \approx 90^\circ$ ) and is exponentially decreasing in the bottom ( $\text{Im}[\gamma_{ev2}] < 0$ ). For the case in Fig. 2-12, the field due to  $\gamma_{ev2}$  is just 5 dB weaker than that due to the usual evanescent field saddle point, so the contribution of the former cannot be ignored. We do not believe, however, that the additional saddle point represents any distinct mechanism of propagation, but simply that it is sometimes required to complete the description of the evanescent field.

It is interesting to note how the saddle point structures of the reflected and transmitted fields are related at the interface, where the total pressure field must be continuous. At short ranges (small  $\theta_0$ ), the saddle point corresponding to the partially reflected ray becomes, as the interface is crossed, the saddle point corresponding to the transmitted ray. At long ranges (large  $\theta_0$ ), it is the reflected lateral wave ray that evolves into the transmitted ray, both of which lie near the critical angle. In addition, the totally reflected ray above the interface becomes the evanescent ray in the bottom. Of course, the incident field must be added to the reflected field to obtain continuity with the transmitted field at the interface.

A comparison between classical ray theory and the exact result [obtained by numerical integration of Eq. (2-74)] for the transmitted field along a horizontal line is shown in Fig. 2-13. As in Fig. 2-4 for the reflected field, the geometric



**Figure 2-13** COMPARISON BETWEEN CLASSICAL RAY THEORY AND THE EXACT RESULT FOR THE NORMALIZED TRANSMITTED FIELD. VALUES OF  $z_s$  AND  $z_r$  IN WAVELENGTHS  $\lambda$  ARE SHOWN FOR EACH PLOT. THE INTERFACE IS THE SAME AS IN FIG. 2-4.

spreading and phase terms predicted by classical ray theory have been removed from the total field, so that only the effect of the transmission process remains. The geometric parameters  $z_s$  and  $z_r$  for each plot are indicated on the figure. Note that the ratio  $z_s/z_r = 4$  is held constant so that the classical ray result is the same for each geometric configuration. Classical ray theory is less accurate at lower frequencies (source and receiver closer to the interface in terms of wavelengths) because the evanescent field is more significant. The interference evident at the longer ranges (larger  $\theta_0$ ) is between the transmitted and evanescent rays. Attenuation in the bottom would enhance the importance of the evanescent ray



To find an expression for the ray displacement  $\Delta$ , we manipulate the saddle point criterion in Eq. (2-77). Using Snell's law and geometry, we can write the factor  $(\sin \theta + q')$  as

$$\left( \sin \gamma - \frac{\sin \gamma \cos \gamma}{n \cos \gamma_1} \right) = \frac{-\sin(\gamma_1 - \gamma)}{\cos \gamma_1} = \frac{-\overline{BE}/\overline{BR}}{z_r/\overline{BR}} = \frac{-\overline{BE}}{z_r} \quad (2-79)$$

Substituting for  $\sin(\gamma - \theta_0) = -\overline{CE}/R_1$  in the first term of Eq. (2-77), we obtain

$$f'(\gamma) = \frac{i\overline{CE}}{R_1} - \frac{i\overline{BE}}{R_1} + \frac{1}{kR_1} \frac{W'(\gamma)}{W(\gamma)} = 0 \quad (2-80)$$

Multiplying by  $-iR_1$  and recognizing that  $\overline{CE} - \overline{BE} = \Delta \cos \gamma$ , we find

$$\Delta(\gamma) = \frac{i}{k \cos \gamma} \frac{W'(\gamma)}{W(\gamma)} \quad (2-81)$$

Thus, the ray displacement for the transmission case Eq. (2-81) is obtained from the reflection case Eq. (2-60) by simply replacing  $W$  for  $V$ .

As before, the eigenray equation is obtained by substituting  $\Delta$  into the saddle point criterion. Taking our cue from the reflection case, we multiply Eq. (2-77) by  $iR_1/\cos \gamma$  and expand the  $\sin(\ )$  terms:

$$\begin{aligned} \frac{iR_1}{\cos \gamma} f'(\gamma) &= \frac{R_1 \sin(\gamma - \theta_0)}{\cos \gamma} + \frac{z_r \sin(\gamma_1 - \gamma)}{\cos \gamma \cos \gamma_1} + \Delta = 0 \\ &= R_1 \tan \gamma \cos \theta_0 - R_1 \sin \theta_0 + z_r \tan \gamma_1 - z_r \tan \gamma + \Delta = 0 \end{aligned} \quad (2-82)$$

After substituting  $R_1 \cos \theta_0 = z_s + z_r$  and  $R_1 \sin \theta_0 = r$  (see Fig. 2-14), we obtain the eigenray equation

$$\begin{aligned} r &= z_s \tan \gamma + \Delta + z_r \tan \gamma_1 \\ &= r_1(\gamma) + \Delta(\gamma) + r_2(\gamma) \end{aligned} \quad (2-83)$$

The characteristics of the transmitted eigenray are obtained from the saddle point approximation in the same manner as for the reflected eigenray:

$$p(\theta_0, R_1, z_r) = \underbrace{\sqrt{\frac{\sin \gamma}{r}}}_{G_\phi} \underbrace{\sqrt{\frac{1}{iR_1 f''(\gamma)}}}_{G_\theta} \underbrace{W(\gamma)}_{\text{transmission loss}} \exp[i \underbrace{(k\overline{SA} + k\Delta \sin \gamma + k_1 \overline{BR})}_{\text{ray path phase } \Phi}] \quad (2-84)$$

The ray path phase  $\Phi$  in Eq. (2-84) is obtained as follows:

$$\begin{aligned}
 \Phi(\gamma) &= kR_1 \cos(\gamma - \theta_0) - kz_r(\cos \gamma - n \cos \gamma_1) \\
 &= k(\overline{SA} + \overline{AC} + \overline{CD}) - k\overline{BR} \cos \gamma_1 (\cos \gamma - n \cos \gamma_1) \\
 &= k\overline{SA} + k\Delta \sin \gamma + k\overline{BR} [\cos(\gamma_1 - \gamma) - \cos \gamma_1 \cos \gamma] + k_1 \overline{BR} \cos^2 \gamma_1 \\
 &= k\overline{SA} + k\Delta \sin \gamma + k\overline{BR} \sin \gamma \sin \gamma_1 + k_1 \overline{BR} \cos^2 \gamma_1 \\
 &= k\overline{SA} + k\Delta \sin \gamma + k_1 \overline{BR} \quad . \quad (2-85)
 \end{aligned}$$

The geometric spreading factors in Eq. (2-84) have the same interpretation as for the reflection case shown in Fig. 2-9. In terms of the ray path lengths, they can be written

$$G_\theta = \sqrt{\frac{1}{r'(\gamma) \cos \gamma}} = \sqrt{\frac{1}{\overline{SA} + \Delta' \cos \gamma + \overline{BR} \cos^2 \gamma / (n \cos^2 \gamma_1)}} \quad (2-86)$$

$$G_\phi = \sqrt{\frac{\sin \gamma}{r}} = \sqrt{\frac{1}{\overline{SA} + \Delta / \sin \gamma + \overline{BR} / n}} \quad (2-87)$$

In the reflection case, the ray displacement  $\Delta$  (at a lossless interface) turns out to be real for totally reflected and lateral wave eigenrays. In the transmission case, however, the displacement  $\Delta$  turns out to be complex, which means that the simple interpretation of a real displacement upon transmission, as depicted in Fig. 2-14, does not hold. Using the case illustrated in Fig. 2-11 as an example, we find that  $\Delta$  is largely imaginary for transmitted rays. Its magnitude is very small at short ranges (indicating the accuracy of classical ray theory there) but larger at longer ranges. For example, the eigenray for the receiver at  $\theta_0 = 60^\circ$  and  $z_r = 1\lambda$  in Fig. 2-11 has angle  $\gamma = 55^\circ - i0.5^\circ$  and displacement  $\Delta = (0.03 + i0.28)\lambda$ . Recall that classical ray theory may be obtained by neglecting the displacement. From Fig. 2-13 we see that neglecting the displacement for the receiver at  $\theta_0 = 60^\circ$  and  $z_r = 1\lambda$  results in an error of 0.6 dB. Thus, although the displacement is complex and cannot be interpreted physically, we must include it in the mathematical treatment of the transmitted field. Real displacements are found only for receivers at long ranges on the interface ( $z_r = 0$ ), where  $\Delta$  is the same as for the reflected lateral wave ray on the opposite side of the interface.

For the saddle points in Fig. 2-11 that represent the evanescent field (which is not accounted for by classical ray theory), the magnitude of  $\Delta$  is on the order of  $1.5-6\lambda$ , and the real part is somewhat larger than the imaginary part. By Snell's law the plane waves in the bottom that correspond to the "evanescent ray" saddle points are inhomogeneous, with real parts close to  $90^\circ$ . The fact that the eigenray characteristics have significant imaginary parts is an indication that the evanescent field in the bottom cannot be represented as a simple ray field.

## 2-9 CONCLUSIONS

In this chapter we have developed a systematic method for finding the reflected and transmitted fields due to a point source in the presence of a plane, penetrable interface. The basic technique is to allow the plane wave reflection and transmission coefficients to influence the saddle point location by moving them into the phase function  $f$  before taking this function's derivative to find the saddle points. The result is that the saddle points are, in general, complex. Complicated effects of the reflection and transmission processes, such as the reflected lateral wave field in the water and the evanescent field in the bottom, are now included in a natural way in the saddle point formulation. By tracking the steepest descent paths in the complex  $\theta$ -plane and comparing them with the required contour of integration, one can determine whether multiple eigenrays exist at a given receiver. Numerical integration along the steepest descent paths provides a robust and frequency-independent method for evaluating the eigenray field when the usual saddle point approximation is not valid.

An attractive feature of our approach is that each saddle point can be associated with an eigenray having a certain path of propagation. Characteristics such as ray travel time, geometric spreading losses, and reflection or transmission loss provide one with physical insight into the problem. In certain transition regions, the field is too complicated to be simply expressed as a single ray field or even the superposition of several ray fields. Examples are the reflected field in the region of the critical angle and the transmitted field in the region where the transmitted ray is first accompanied by the evanescent ray. In such regions steepest descent paths are curved and contributions to the field integral come from a range of angles. Since the saddle point approximation is not valid, numerical integration along the steepest descent path must be used to evaluate the field strength. Despite the fact that a detailed physical interpretation of complex eigenray characteristics is not always possible, the real parts of the eigenray angles do indicate the approximate path of the energy represented by the eigenray.

The overriding motivation for this work has been to develop a method for solving the single interface problem in a way that could be extended to more complex environments. In the following chapter we will apply the ray method to a flat waveguide (the Pekeris model) and to a sloping waveguide (the penetrable wedge problem). For these environments, the total field is expressed as a *sum* of ray fields, each of which can be evaluated using the methods outlined in this chapter.

## CHAPTER 3

### APPLICATION OF THE RAY METHOD TO FLAT AND SLOPING WAVEGUIDES

#### 3-1 INTRODUCTION

In the previous chapter, a method was developed for finding the field due to a point source in the presence of a single plane, penetrable interface. The method involves allowing the plane wave reflection or transmission coefficient to influence the location of the (possibly complex) saddle points, as well as their associated steepest descent paths. In this chapter we find the field in flat and sloping waveguides by using the same saddle point method to evaluate each one of the ray fields that contributes to the total field.

The so-called Pekeris waveguide serves as a simple model for acoustic propagation in shallow water ocean environments. It consists of a flat, homogeneous fluid layer (water) that is bounded below by a homogeneous fluid halfspace of higher velocity (sand, for example) and above by a pressure-release interface. Traditionally, this model has been analyzed using normal mode theory, beginning with the classic work of Pekeris.<sup>17</sup> Brekhovskikh's treatment of the problem, in Chapter 5 of Ref. 5, includes both the ray and mode approach. Most computational implementations of normal mode theory include only the discrete modes, which limits the validity of the solution to long ranges. In more recent years, closer attention has been paid to the remainder of the solution, referred to as the continuous spectrum or the branch line contribution.<sup>18</sup> In the case where a mode is near cutoff (the transition from the discrete spectrum to the continuous spectrum at the critical angle), normal mode theory can be invalid at *all* ranges. The concepts of "virtual modes"<sup>19</sup> and "pseudoresonances"<sup>20</sup> have been proposed as means for correcting the theory in this case.

The modeling of the Pekeris waveguide in terms of rays with beam displacement has been carried out by Tindle, *et al.*<sup>9,10,11</sup> Although this ray formulation has been successfully applied in various circumstances, it does not model

the field accurately in the region of the critical angle. In this region, a ray theory caustic is formed, and correction formulas based on uniform asymptotic expansions must be used. However, the caustic corrections do not completely solve the problem because the field predicted from the shadow-zone formula does not match up well with the partially reflected field at shorter ranges. As can be seen in Fig. 1 of Ref. 12, the field at ranges shorter than the caustic range is not correctly accounted for by the shadow-zone formula alone. From Fig. 1 of Ref. 11, we see that partially reflected rays undergo no beam displacement and are abruptly cut off at the critical angle. Adding the partially reflected ray field to the shadow-zone field only corrects the field at short ranges; closer to the critical angle the field is still incorrect, and there is a discontinuity where the partially reflected rays are cut off at the critical angle. The reason that good results have been obtained using the usual beam displacement formulation<sup>9,10,11</sup> is that the partially reflected field, corresponding to the continuous spectrum in mode theory, is very weak at sufficiently long ranges in a flat waveguide.

In the present approach, as described in Chapter 2, we find the correct field in the problematic region of the critical angle by incorporating the *entire* reflection coefficient (rather than just its phase) in the saddle point criterion, finding complex saddle points, and numerically integrating along the paths of steepest descent. The field calculated in this way matches smoothly with the field at shorter ranges due to partially reflected rays, as well as with the field at longer ranges due to totally reflected rays plus lateral wave rays. For lossless interfaces, the representation of the field at long ranges is equivalent to the previous beam displacement formulation.

The second environment to which we will apply our ray method is the sloping waveguide or wedge, which is a useful model for coastal and continental shelf areas. The wedge problem has received considerable attention from the underwater acoustics community in recent years. Jensen and Kuperman<sup>21</sup> have used a parabolic equation model to demonstrate the cutoff of modes in upslope propagation. Pierce<sup>22</sup> and Kamel and Felsen<sup>23</sup> have studied the same issue from a theoretical standpoint. Arnold and Felsen<sup>24</sup> discuss the field in a wedge in terms of rays and local modes, and Arnold, *et al.*,<sup>25,26,27</sup> have developed the theory of intrinsic modes for the penetrable wedge. Xiang, *et al.*,<sup>28</sup> have recently reported progress in simplifying the intrinsic mode formulation.

The work of Tindle and Deane<sup>12</sup> was the first successful application of ray theory to a shallow water wedge. Using the beam displacement formulation from Ref. 10, good general agreement was found between ray theory and adiabatic normal mode theory for cases where the adiabatic approximation is valid (small slopes and no mode cutoff). In such cases, the problem in the beam displacement

formulation in the area of the critical angle apparently did not affect the results significantly. According to Sec. I of Ref. 12, partially reflected energy was accounted for by way of the shadow-zone caustic correction factors, and no partially reflected rays were included in the calculations. For moderate and large ocean bottom slopes, however, proper accounting of energy incident on the bottom at angles near and steeper than the critical angle is essential because, due to the change in ray angle upon each bottom reflection, many rays important to the field calculation are reflected from the bottom at such angles. In contrast to the flat waveguide, these partially reflected rays are important at *all* ranges from the source in the wedge, not just at short ranges.

The first three sections of this chapter deal with the flat waveguide. Section 3-2 describes the ray method for calculating the field, Section 3-3 contains comparisons of the ray model with the SAFARI model and a normal mode model, and Section 3-4 reviews the structure of the eigenrays at several receivers in the waveguide. The next three sections treat the sloping waveguide. Section 3-5 contains a derivation of the integral expression for the ray fields, Section 3-6 contains a comparison of the ray model with a two-way coupled mode model, and Section 3-7 gives examples of the eigenray structure. Concluding remarks are made in Sec. 3-8.

### 3-2 RAY METHOD FOR THE FLAT WAVEGUIDE

The environment assumed is the standard Pekeris waveguide illustrated in Fig. 3-1(a). The parameters needed to describe it are the ratio of sound speeds  $n = c/c_1$ , the ratio of densities  $m = \rho_1/\rho$ , and the water depth  $h$ . In the water, the wave number  $k$  is related to the wavelength  $\lambda$ , the frequency  $f$ , and the sound speed  $c$  by  $k = 2\pi/\lambda = 2\pi f/c$ . The source-receiver geometry is specified by the horizontal range  $r$  and the source and receiver depths  $z_s$  and  $z_r$ , respectively. All distances are expressed in terms of the wavelength  $\lambda$ . We assume that  $n < 1$ , which is typical for water-sand interfaces in shallow water ocean environments. In such a case, the critical angle  $\theta_{cr} = \arcsin(n)$  is real. Attenuation may be included in either medium by allowing the appropriate sound speed to have an imaginary part (see Sec. 2-5), which causes  $n$  to be complex as well.

The total field at a receiver in the Pekeris waveguide is expressed as a sum of ray fields due to the source and its images, which are illustrated in Fig. 3-1(b). The straight lines connecting the image sources with the receiver represent the ray paths of classical ray theory. We specify each ray path by the number of bottom reflections  $N_b$ , the number of surface reflections  $N_s$ , and the ray's direction of travel at the receiver. The ray field due to each image source is represented as

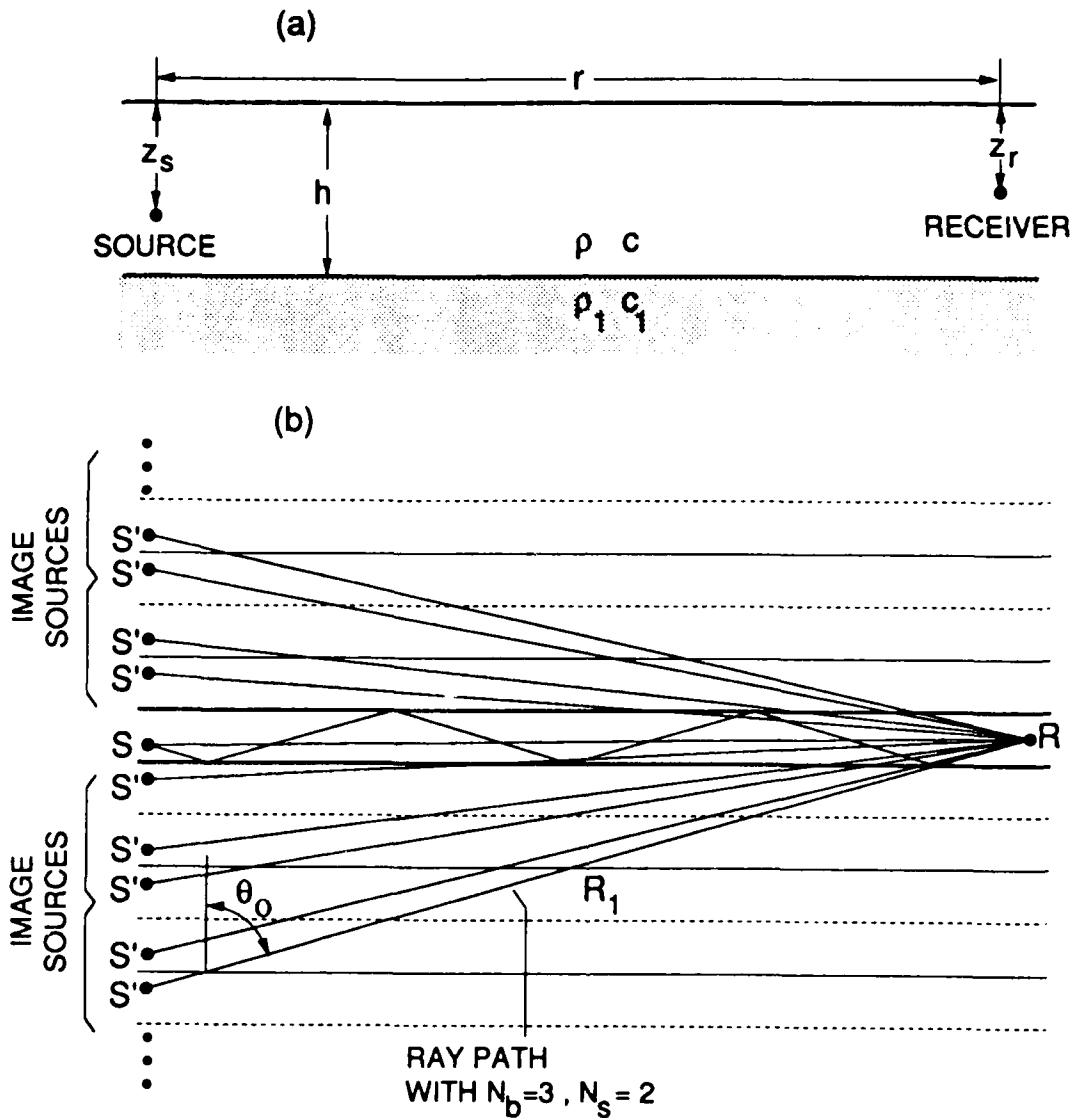


**Figure 3-1** GEOMETRY FOR THE FLAT WAVEGUIDE. (a) SOURCE-RECEIVER GEOMETRY. (b) SYSTEM OF IMAGE SOURCES, EACH OF WHICH REPRESENTS A DIFFERENT RAY PATH. THE THIN DASHED LINES REPRESENT IMAGED SURFACES, AND THE THIN SOLID LINES REPRESENT IMAGED OCEAN BOTTOMS.

a contour integral over plane waves in the complex  $\theta$ -plane, where  $\theta$  is the plane wave angle of incidence. We solve the integrals in terms of *eigenrays*, which are specific rays at specific angles that travel from source to receiver. It is important to realize that there may be more than one eigenray with a given ray path (a given sequence of reflections). For example, we saw in Chapter 2 that a lateral wave eigenray always accompanies a totally reflected eigenray.

The expression for the field reflected once from a plane, penetrable interface is given by Eq. (2-28). To modify this expression for a ray path that has  $N_b$  bottom reflections, with plane wave reflection coefficient  $V$ , and  $N_s$  surface reflections, with reflection coefficient  $-1$ , we write

$$p(\theta_0, R_1) = (-1)^{N_s} \sqrt{\frac{k}{2\pi r}} e^{i\frac{\pi}{4}} \int_{-\frac{\pi}{2}+i\infty}^{\frac{\pi}{2}-i\infty} e^{ikR_1 \cos(\theta-\theta_0)} [V(\theta)]^{N_b} \sqrt{\sin \theta} d\theta \quad , \quad (3-1)$$

where  $V$  is given by Eq. (2-18). For each of the image sources in Fig. 3-1(b) the appropriate values of the incident angle  $\theta_0$  and the distance  $R_1$  that specify the receiver location can be calculated from simple geometry. The total field is given by an infinite sum of ray fields of the form in Eq. (3-1) due to the infinite number of image sources that exist. In practice, the sum can be truncated after  $\theta_0$  has become sufficiently small and  $N_b$  sufficiently large that the ray is insignificant due to multiple *partial* reflections at the bottom.

As in Chapter 2 we use the method of steepest descent to solve the integral for each ray field. Before applying the method we incorporate the reflection process into the saddle point criterion by expressing

$$[V(\theta)]^{N_b} = e^{N_b \ln V(\theta)} \quad , \quad (3-2)$$

so that we may write the ray field as

$$p(\theta_0, R_1) = (-1)^{N_s} \sqrt{\frac{k}{2\pi r}} e^{i\frac{\pi}{4}} \int_{-\frac{\pi}{2}+i\infty}^{\frac{\pi}{2}-i\infty} e^{kR_1 [i \cos(\theta-\theta_0) + \frac{N_b}{kR_1} \ln V(\theta)]} \sqrt{\sin \theta} d\theta \quad . \quad (3-3)$$

The phase function in the steepest descent method (see Sec. 2-3) is now

$$f(\theta) = i \cos(\theta - \theta_0) + \frac{N_b}{kR_1} \ln V(\theta) \quad , \quad (3-4)$$

and the criterion for the saddle point  $\gamma$  is

$$f'(\theta) = -i \sin(\theta - \theta_0) + \frac{N_b}{kR_1} \frac{V'(\theta)}{V(\theta)} = 0 \quad \text{at } \theta = \gamma \quad , \quad (3-5)$$

where prime indicates differentiation with respect to  $\theta$ . It can be seen by comparing Eq. (3-5) to Eq. (2-48) that it is no more difficult to find the saddle points for the multiply reflected field than for the singly reflected field since the only difference is the factor  $N_b$ .

As in Sec. 2-7.1, Eq. (3-5) can be interpreted geometrically as an eigenray equation, where a horizontal displacement

$$\Delta(\gamma) = \frac{i}{k \cos \gamma} \frac{V'(\gamma)}{V(\gamma)} \quad (3-6)$$

occurs at each of the  $N_b$  bottom reflections. The structure of the saddle points as a function of horizontal receiver range  $r$  is similar to that for the singly reflected field illustrated in Figs. 2-5 and 2-7.

Once the saddle point  $\gamma$  is found, the integral in Eq. (3-3) is evaluated in one of two ways, as detailed in Chapter 2. The first method is to apply the first-order saddle point approximation given in Eq. (2-38) to Eq. (3-3). The result is

$$p(\theta_0, R_1) = (-1)^{N_b} \sqrt{\frac{\sin \gamma}{r}} \sqrt{\frac{1}{i R_1 f''(\gamma)}} [V(\gamma)]^{N_b} e^{i k R_1 \cos(\gamma - \theta_0)} \quad (3-7)$$

where  $f''$  is obtained by taking an additional derivative of Eq. (3-5). The second method, which is required when the saddle point is near the critical angle, is to numerically integrate along the path of steepest descent in the complex  $\theta$ -plane. As discussed in Sec. 2-7.2, the  $\sqrt{\sin \theta}$  term in the integrand of Eq. (3-3) is evaluated at the saddle point  $\gamma$  and taken outside the integral before the integration is performed. We do so because the integral over  $\theta$  represents the geometrical spreading  $G_\theta$  of the ray bundle in the plane of Fig. 3-1, while the factor  $G_\phi = \sqrt{\sin \gamma / r}$  represents the spreading in the perpendicular plane. We will see that the separation of the spreading factors in this way is useful when constructing the integral for the sloping waveguide in Sec. 3-5.

The algorithm for finding the field at a series of receivers at constant depth  $z_r$  proceeds as follows. First, the field due to the direct path arrival is found at all the receivers. The amplitude of this field serves as a reference for deciding when to neglect rays that are significantly weaker. Next, the algorithm loops through the image sources [see Fig. 3-1(b)], finding the field at all receivers for each ray path. The ray field calculation starts at the receiver for which  $\theta_0 \approx \theta_{cr}$ , and the field is found by numerical integration along the steepest descent path. The field at longer ranges (larger angles  $\theta_0 > \theta_{cr}$ ) is found next, each time checking if a lateral wave ray also exists. Once the lateral wave exists also, the saddle point approximation is compared to the exact (numerical) result. If the approximation is

accurate enough, it can then be used for all the receivers farther out in range. This procedure for testing the accuracy of the saddle point approximation is applied to the lateral wave ray as well as to the totally reflected ray. In addition, the strength of the lateral wave ray is compared to the reference strength, and when the lateral wave ray is sufficiently weak, it can be neglected for receivers at longer ranges.

The same type of procedure is used for the partially reflected ray field at the shorter ranges, for which  $\theta_0 < \theta_{cr}$ . As  $N_b$  gets larger, the partially reflected field drops off more and more sharply with decreasing range  $r$ . When  $N_b$  is sufficiently large that the ray field at all the receivers is insignificant due to numerous partial reflections, the process is terminated and the total field has been found.

The field in the bottom of the flat waveguide may be found using the same approach. Since all the energy arrives from above, only the upper half of image sources in Fig. 3-1(b) contributes. From the expression for the transmitted field at a single interface Eq. (2-75), we derive the following for the flat waveguide case:

$$\begin{aligned}
 p(\theta_0, R_1, z_r) = & (-1)^{N_b} \sqrt{\frac{k}{2\pi r}} e^{i\frac{\pi}{4}} \int_{-\frac{\pi}{2}+i\infty}^{\frac{\pi}{2}-i\infty} \exp\left\{kR_1 \left[ i \cos(\theta - \theta_0) \right. \right. \\
 & - \frac{iz_r}{R_1} (\cos \theta - n \cos \theta_1) \\
 & \left. \left. + \frac{1}{kR_1} (N_b \ln V(\theta) + \ln W(\theta)) \right] \right\} d\theta \quad , \quad (3-8)
 \end{aligned}$$

where  $N_b$  is the number of bottom reflections of the ray path (not including the final transmission),  $W$  is the plane wave transmission coefficient given in Eq. (2-73),  $z_r$  is now the positive distance below the bottom interface, and  $\theta_1$  is the plane wave angle in the bottom given by Snell's law,  $\sin \theta_1 = \sin \theta / n$ . In solving Eq. (3-8) in terms of saddle points, we always find a saddle point corresponding to the usual transmitted ray. When  $\theta_0$  is large there may also be a saddle point that accounts for the evanescent leakage of energy into the bottom, as discussed in Sec. 2-8.

### 3-3 COMPARISON OF MODELS FOR THE FLAT WAVEGUIDE

In order to test the validity of the ray model, which we refer to as the ACCURAY model, we have compared its predictions of propagation loss with those of other models, namely the SAFARI fast field program<sup>29</sup> developed at the SACLANT Centre in La Spezia, Italy, and a normal mode model called

NEMESIS<sup>30</sup> developed at the Applied Research Laboratories, The University of Texas at Austin. The SAFARI model, whose algorithm solves the Bessel transform of the wave equation in range-independent environments by direct numerical integration, should be accurate at all frequencies and all but very short ranges. The normal mode model includes the discrete spectrum in its calculations, but does not account for the branch line integral.

The first case for comparison of the models was chosen so that a mode would be just on the verge of cutoff. The bottom parameters are  $n = 0.9375$

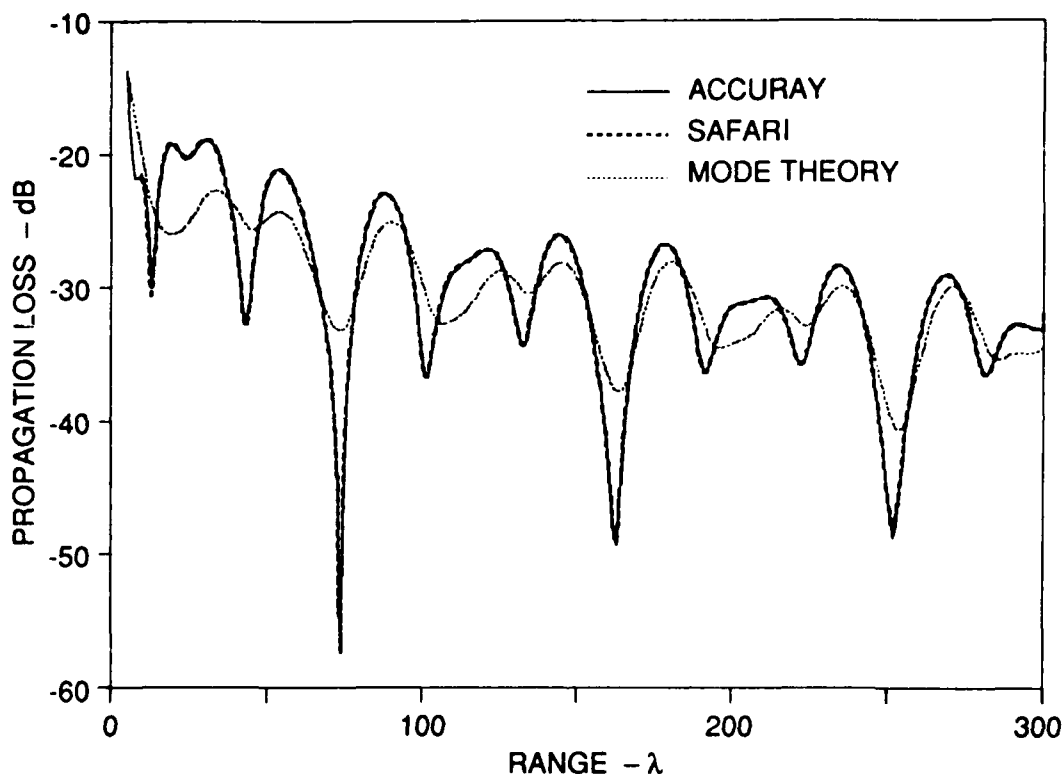
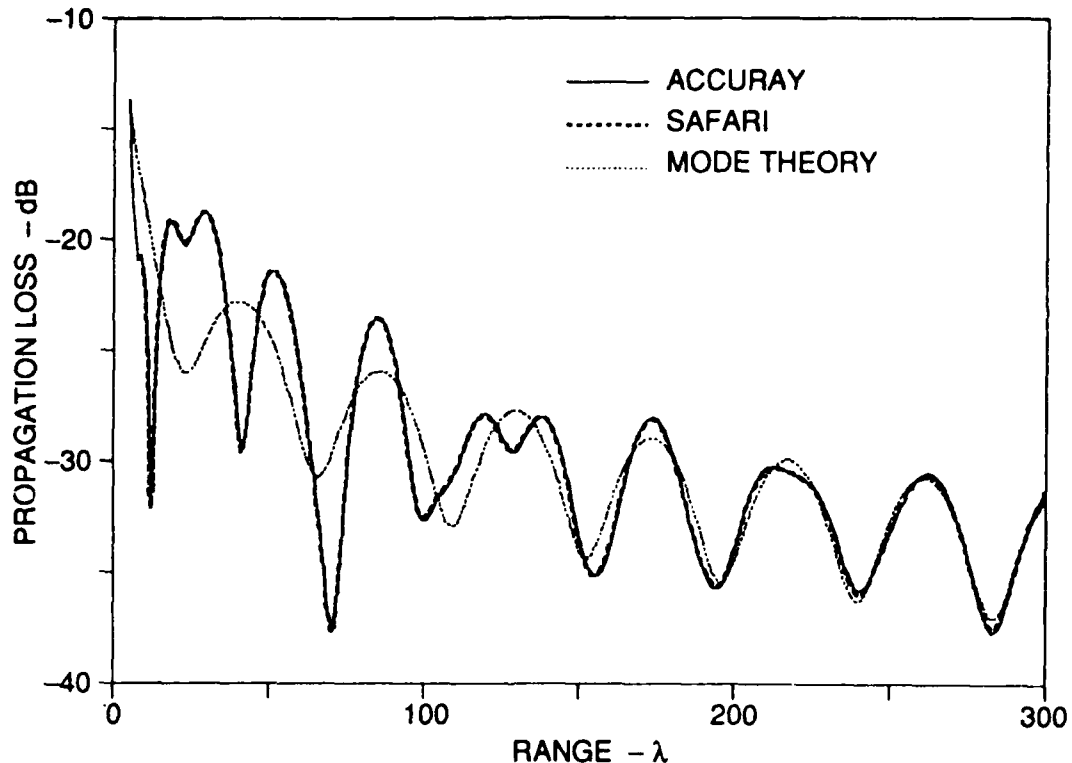


Figure 3-2 COMPARISON OF THE RAY MODEL (ACCURAY), THE SAFARI MODEL, AND A DISCRETE NORMAL MODE MODEL FOR A FLAT WAVEGUIDE OF DEPTH  $h = 3.6\lambda$ . THREE TRAPPED MODES EXIST, BUT MODE 3 IS VERY CLOSE TO CUTOFF. THE EXTREMELY CLOSE AGREEMENT BETWEEN THE ACCURAY AND SAFARI MODELS MAKES THEIR PLOTS DIFFICULT TO DISTINGUISH.

( $\theta_{cr} = 69.6^\circ$ ) and  $m = 1.25$ , and the source and receiver depths are  $z_s = 0.72\lambda$  and  $z_r = 0.60\lambda$ . Figure 3-2 shows a comparison of the three models for a water depth of  $h = 3.60\lambda$ , which is slightly deeper than the cutoff depth for the third mode

$h_{c3} = 3.59\lambda$ . The figure shows that the ray model and the SAFARI model agree so closely that the plots can barely be distinguished. The normal mode model, however, is typically off by 4 dB at the peaks and 15 dB at the valleys of the plot. The reason for its poor performance in this case is that the pole corresponding to mode 3 is very close to the branch point singularity at the critical angle. These results demonstrate that SAFARI and the ray model correctly account for energy in the neighborhood of the critical angle, while normal mode models with only the discrete spectrum do not.

The second case for comparison is the same as the first except the water depth has been lowered to  $h = 3.5\lambda$ , so that only the first two normal modes are trapped. It can be seen from Fig. 3-3 that there is still near perfect agreement



**Figure 3-3** AS IN FIG. 3-2, EXCEPT THE WATER DEPTH HAS BEEN REDUCED TO  $h = 3.5\lambda$ . MODE 3 IS NOW CUT OFF, BUT STILL CONTRIBUTES SIGNIFICANTLY AT THE SHORTER RANGES.

between the ACCURAY and SAFARI models. The mode model's performance is somewhat better than for the previous case, but it is still quite poor, especially at the shorter ranges. Although not trapped in this case, Mode 3 does, nevertheless,

influence the field quite strongly out to a range of at least  $200\lambda$ , which corresponds to 57 water depths.

Since most realistic ocean bottoms possess some attenuation, we consider in Fig. 3-4 the same case as in Fig. 3-2 except that an attenuation of  $0.5 \text{ dB}/\lambda$  has been included in the bottom. The continued close agreement between the ACCU-

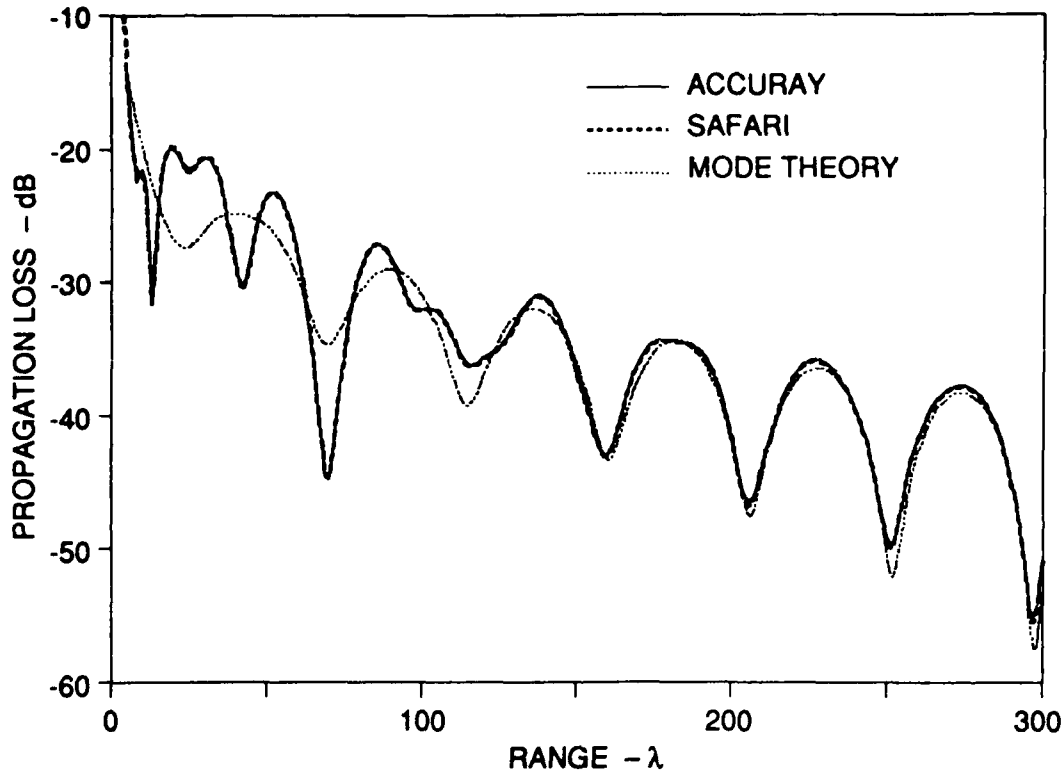


Figure 3-4 AS IN FIG. 3-2, EXCEPT THE BOTTOM HAS AN ATTENUATION OF  $0.5 \text{ dB}/\lambda$ . THE IMPORTANCE OF MODE 3 DECREASES WITH RANGE DUE TO THE ATTENUATION.

RAY and SAFARI models indicates that attenuation has been properly included in the ray model approach.\* The important difference from the lossless case is that the normal mode model's results are somewhat more accurate, especially beyond a range of  $140\lambda$ , or 39 water depths. The improvement is due to the fact that mode 3, whose proximity to the critical angle causes the poor performance in the lossless case, is now significantly attenuated with increasing range.

\*The ACCURAY and SAFARI models both account for attenuation by way of complex sound speeds or wave numbers.

In Ref. 31 Mannseth shows comparisons of propagation loss in shallow water between the formulation of ray theory with beam displacement given in Ref. 10, the discrete normal mode solution, and the exact solution (obtained by adding the branch line integral to the discrete modes). Similar conclusions are made regarding the inadequacy of the discrete mode solution when a mode is near cutoff. In addition, it is shown that the solution using rays with beam displacement is also quite poor in the region of mode cutoff. For cases where no modes are near cutoff the ray solution is better, but not as good as the discrete mode solution. Thus, the method presented here for obtaining a ray solution is an improvement over the formulation used in Refs. 9-11. The main difference is that the present method accounts correctly for the transition from total to partial reflection.

Our final comparison of models appears in Fig. 3-5, where the water

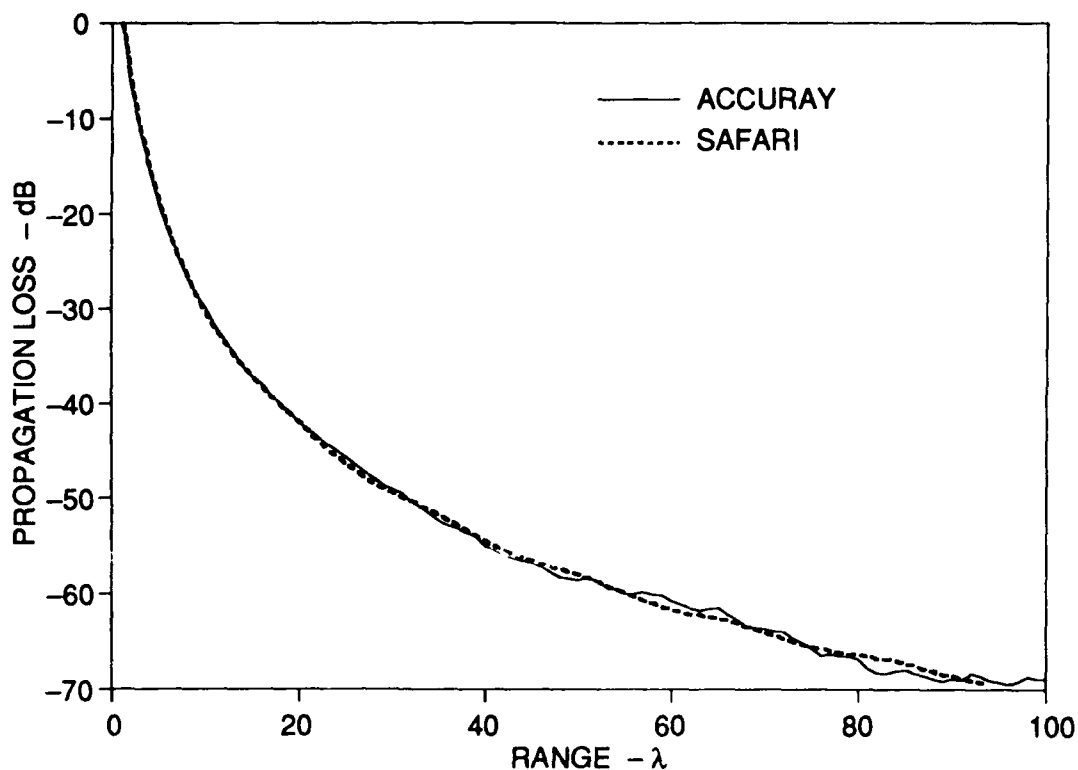


**Figure 3-5** COMPARISON OF THE RAY MODEL (ACCURAY) AND THE SAFARI MODEL FOR A FLAT WAVEGUIDE OF DEPTH  $h = 0.5\lambda$ . NO TRAPPED MODES ARE PRESENT.

depth has been reduced to  $h = 0.5\lambda$  and the maximum range considered is  $100\lambda$ , or 200 water depths. The source and receiver depths are  $z_s = 0.2\lambda$  and  $z_r = 0.4\lambda$ ,

respectively. Since no trapped modes are present ( $h_{c1} = 0.72\lambda$ ), the discrete normal mode model cannot be applied. Agreement between the ACCURAY and SAFARI models is still very good. The field in this case decays much more rapidly with range than in the other cases considered. The ray solution at the longest range requires the inclusion of ray paths with up to 40 bottom reflections, resulting in a total of more than 160 eigenrays. Despite the fact that each individual ray is quite strong, the destructive interference between rays results in a weak field. The reason that the ACCURAY solution is not smooth at long ranges is that small errors in the individual ray fields cause imperfect interference between rays.

### 3-4 EIGENRAY STRUCTURE IN THE FLAT WAVEGUIDE

Figure 3-6 shows the saddle points and their corresponding steepest descent paths in the complex  $\theta$ -plane for receivers at ranges of  $50\lambda$  and  $200\lambda$  for the environment modeled in Fig. 3-2. Each of the saddle points, indicated by the bold dots, represents the contribution of one eigenray to the total field at the receiver. The physical path that each eigenray takes in the waveguide is indicated in the figure by the number of bottom bounces  $N_b$ . The steepest descent paths drawn in Fig. 3-6 are the actual ones that would be used to find the field from numerical integration. The magnitude of the integrand of Eq. (3-3) is weaker by a factor of 0.005 at the end points of the steepest descent paths than at the saddle points.

The two eigenrays at the largest angles, for which  $N_b = 0$ , are the direct and surface-reflected rays. Their fields are simply calculated according to the spherical wave expression  $e^{ikR_1}/R_1$ . For  $N_b > 0$  there are four eigenrays with the same number of bottom interactions, and as  $N_b$  increases the eigenrays become steeper (their angles of incidence become smaller). For each totally reflected ray with a given ray path, there is a lateral wave ray with the same path whose saddle point lies next to the critical angle. As explained in Sec. 2-5, its steepest descent path loops around the critical angle and serves to complete the contour of integration for the integral representing that ray field.\* The saddle points at smaller angles, whose steepest descent paths cross the branch cut, correspond to the partially reflected eigenrays. Although the transition from total to partial reflection is, in reality, a gradual process, we use the criterion of steepest descent paths crossing, or not crossing, the branch cut to distinguish between partially and totally reflected rays.

The eigenray structure for the receiver at the short range of  $50\lambda$  (14

---

\*To avoid confusion, only one of the four lateral wave paths has been drawn in Fig. 3-6(a), and only three of the 28 lateral wave paths have been drawn in Fig. 3-6(b).

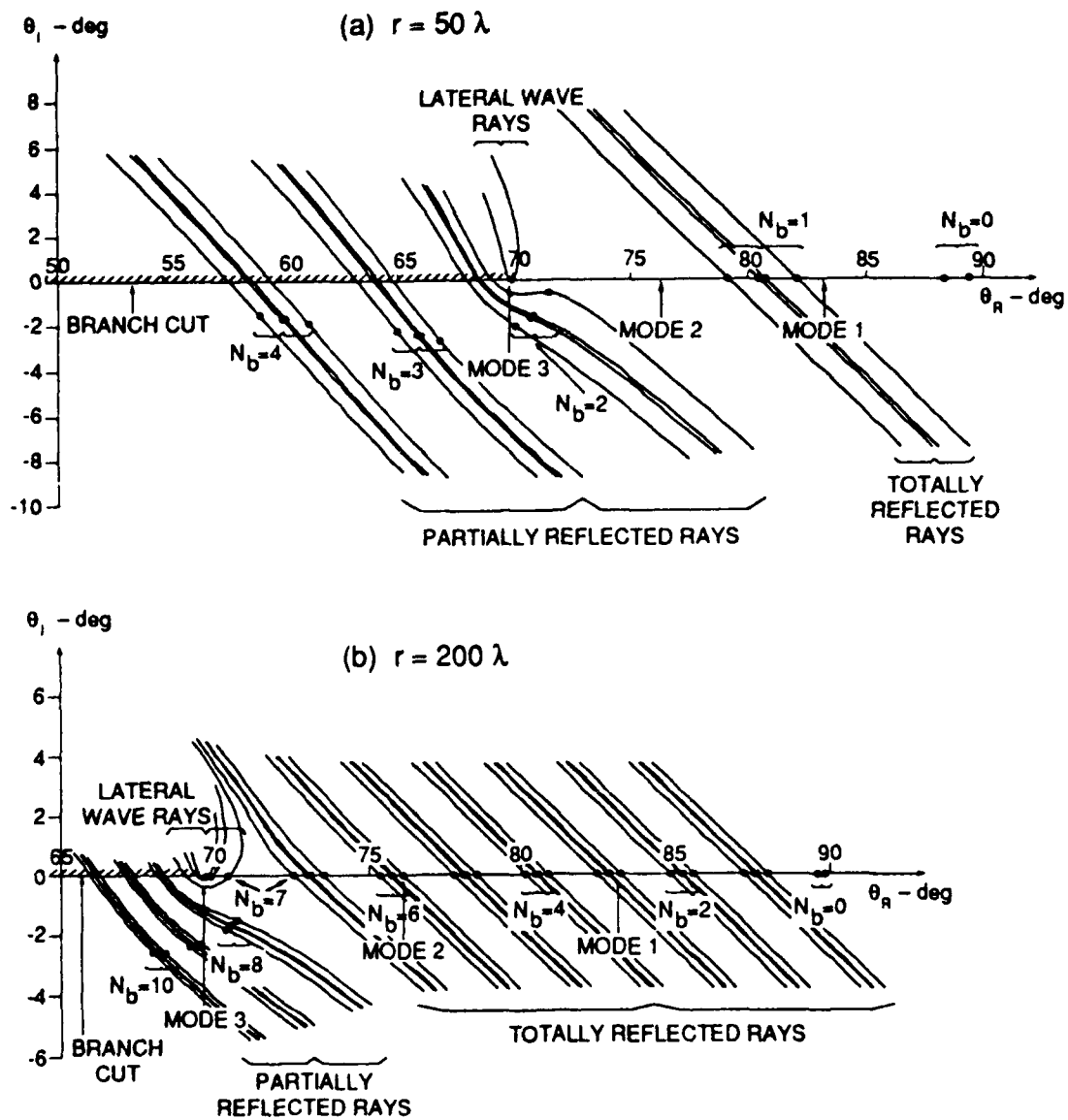


Figure 3-6 SADDLE POINTS AND STEEPEST DESCENT PATHS FOR THE EIGENRAYS AT RECEIVER RANGES (a)  $r = 50\lambda$  AND (b)  $r = 200\lambda$  IN THE WAVEGUIDE MODELED IN FIG. 3-2.

water depths) in Fig. 3-6(a) indicates that relatively few eigenrays make up the total field. Only those with  $N_b = 1$  are totally reflected. Those with  $N_b = 2$  are partially reflected, but their strengths are only 1-6 dB weaker than the totally reflected rays. Additional reflections at subcritical angles introduce much more loss: eigenrays with  $N_b = 2$  and  $N_b = 3$  are approximately 24 dB and 46 dB weaker, respectively, than the totally reflected rays. The lateral wave rays (with  $N_b=1$ ) are 20-23 dB weaker than the totally reflected rays. Neglect of these rays would change the total propagation loss by about 0.8 dB.

For the receiver at the longer range of  $200\lambda$  (56 water depths) in Fig. 3-6(b), eigenrays with up to ten bottom interactions are shown. Those with  $N_b \geq 8$  are partially reflected at the bottom. With no attenuation in the bottom, the strengths of all the totally reflected eigenrays are essentially the same. The *total* horizontal (beam) displacement at the bottom of these totally reflected rays varies from  $24\lambda$  to  $35\lambda$ . The ray displacement *per* reflection decreases from  $24\lambda$  for  $N_b = 1$  to  $5\lambda$  for  $N_b = 7$ . The lateral wave rays with  $N_b = 1$  are 39 dB down from the totally reflected rays, while those with  $N_b = 7$  are 6-8 dB down. When an attenuation of  $0.5 \text{ dB}/\lambda$  is included in the bottom, as in Fig. 3-4, the lateral wave rays at both ranges are severely attenuated. For  $r = 200\lambda$  the totally reflected rays with  $N_b = 7$  suffer an additional attenuation of about 10 dB.

On both of the plots in Fig. 3-6 the angles associated with the trapped normal modes (see Sec. 35.2 of Ref. 5) are indicated by arrows. A comparison of the two plots points out the basic difference between the ray and mode descriptions of the field. At short ranges, few rays describe the field accurately, while several discrete modes describe the field only approximately. The continuous spectrum would be required to complete the mode description. At long ranges, many rays but only a few modes are required to describe the field. The mode solution would be accurate if either no mode were near cutoff or if the bottom had significant attenuation. A good description of how the interference between rays forms a mode may be found in Ref. 9.

### 3-5 RAY METHOD FOR THE SLOPING WAVEGUIDE

#### 3-5.1 Derivation of the plane wave integrals

We now consider the sloping, or wedge, environment illustrated in Fig. 3-7(a). Parameters required to describe this waveguide are  $n = c/c_1$ ,  $m = \rho_1/\rho$ , and the wedge angle  $\alpha$ . The source-receiver geometry is given by the vertical water depth at the source  $h_s$ , the source and receiver depths  $z_s$  and  $z_r$ , and the range  $r$ . The image sources, which lie on a circle centered at the apex

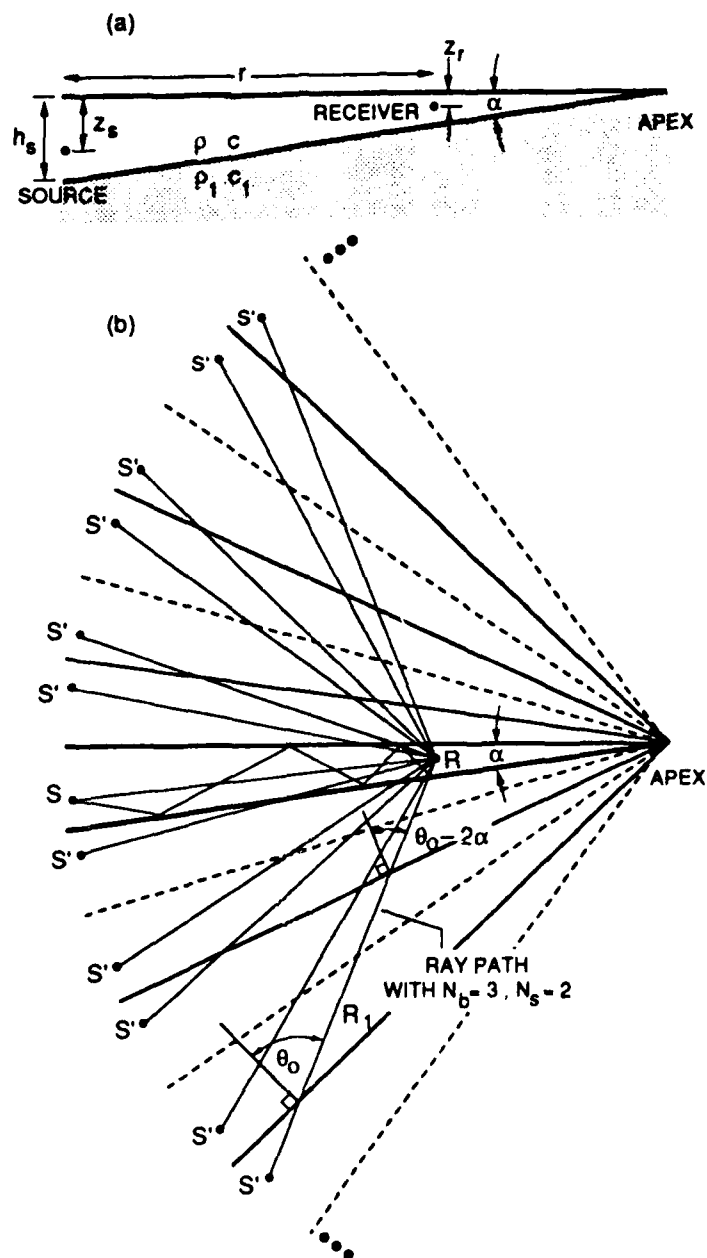


**Figure 3-7** GEOMETRY FOR THE SLOPING WAVEGUIDE. (a) SOURCE-RECEIVER GEOMETRY. (b) SYSTEM OF IMAGE SOURCES, EACH OF WHICH REPRESENTS A DIFFERENT RAY PATH. THE THIN DASHED LINES REPRESENT IMAGED SURFACES, AND THE THIN SOLID LINES REPRESENT IMAGED OCEAN BOTTOMS.

of the wedge, are shown in Fig. 3-7(b). The lines connecting the image sources to the receiver again represent the ray paths of classical ray theory. We consider the case of upslope propagation here, but the downslope case poses no additional problems. Diffraction of the acoustic energy incident directly on the apex of the wedge cannot be included in the present approach, but this effect is negligible in typical ocean environments, where  $\alpha$  is small and the bottom is penetrable.

The field associated with each image source (or, equivalently, ray path) is constructed by appropriately modifying the plane wave integral for the flat waveguide, Eq. (3-3). For a given image source in Fig. 3-7(b), the distance  $R_1$  and the angle of incidence at the first bottom reflection  $\theta_0$  can be computed from simple geometry. The main difference from the flat waveguide is that plane waves undergo successive bottom reflections at incident angles  $2\alpha$  steeper (smaller) than the previous one, as illustrated by the ray path drawn in Fig. 3-7(b). For the general ray path with  $N_s$  surface reflections and  $N_b$  bottom reflections, we may write the pressure field as

$$p(\theta_0, R_1) = (-1)^{N_s} G_\phi \sqrt{\frac{k}{2\pi}} e^{i\frac{\pi}{4}} \int_{-\frac{\pi}{2}+i\infty}^{\frac{\pi}{2}-i\infty} \exp\left\{kR_1 \left[ i \cos(\theta - \theta_0) + \frac{1}{kR_1} \sum_{j=1}^{N_b} \ln V[\theta - 2(j-1)\alpha] \right] \right\} d\theta \quad (3-9)$$

A discussion of the factor  $G_\phi$  will be given below. Again, there may be more than one saddle point (eigenray) when we solve Eq. (3-9).

The phase function of the integrand in Eq. (3-9) is

$$f(\theta) = i \cos(\theta - \theta_0) + \frac{1}{kR_1} \sum_{j=1}^{N_b} \ln V[\theta - 2(j-1)\alpha] \quad (3-10)$$

and the saddle point criterion is now

$$f'(\theta) = -i \sin(\theta - \theta_0) + \frac{1}{kR_1} \sum_{j=1}^{N_b} \frac{V'[\theta - 2(j-1)\alpha]}{V[\theta - 2(j-1)\alpha]} = 0 \quad \text{at } \theta = \gamma. \quad (3-11)$$

Using the same method as in Sec. 2-7.1, the saddle point criterion can be interpreted geometrically as an eigenray equation. The result is that on the  $j$ th bottom reflection from the source,  $j = 1, N_b$ , the eigenray undergoes a displacement parallel to the interface of

$$\Delta(\gamma_j) = \frac{i}{k \cos \gamma_j} \frac{V'(\gamma_j)}{V(\gamma_j)} \quad , \quad \text{where } \gamma_j = \gamma - 2(j-1)\alpha \quad (3-12)$$

Note that in going from Eq. (3-3) to Eq. (3-9), the  $\sqrt{\sin \theta}$  factor has been taken outside the integral and combined with the  $\sqrt{1/r}$  factor to get  $G_\phi$ , a geometric spreading factor that was discussed in Sec. 3-2 for the flat waveguide. In Eq. (2-70), this factor was derived for the single reflection case and expressed as

$$G_\phi = \sqrt{1/L} \quad , \quad (3-13)$$

where  $L$  was related to the ray path segments between source and receiver. For the sloping waveguide,  $L$  is more complicated due to the change in direction of the ray. It takes the form

$$L = \sum(\text{ray path lengths in water}) + \sum_{j=1}^{N_b} \frac{\Delta(\gamma_j)}{\sin \gamma_j} \quad . \quad (3-14)$$

The ray field in the bottom of the wedge can be derived from Eq. (3-8) in a manner similar to the derivation of Eq. (3-9). The result is

$$\begin{aligned} p(\theta_0, R_1, z_r) = & (-1)^{N_b} G_\phi \sqrt{\frac{k}{2\pi}} e^{i\frac{\pi}{4}} \int_{-\frac{\pi}{2}+i\infty}^{\frac{\pi}{2}-i\infty} \exp\left\{kR_1 \left[ i \cos(\theta - \theta_0) \right. \right. \\ & - \frac{iz_r}{R_1} (\cos \theta - n \cos \theta_1) + \frac{1}{kR_1} \left( \sum_{j=1}^{N_b} \ln V[\theta - 2(j-1)\alpha] \right. \\ & \left. \left. + \ln W[\theta - 2N_b\alpha] \right) \right\} d\theta \quad , \quad (3-15) \end{aligned}$$

where  $N_b$  is the number of bottom reflections of the ray path (not including the final transmission),  $W$  is the plane wave transmission coefficient given in Eq. (2-73),  $z_r$  is now the (positive) perpendicular distance from the bottom interface to the receiver, and  $\theta_1$  is the plane wave angle in the bottom given by Snell's law,  $\sin \theta_1 = \sin \theta/n$ . The geometric spreading factor  $G_\phi$  for this case again takes the form given in Eq. (3-13), where the quantity  $L$  is derived from Eq. (2-87) and is given by

$$\begin{aligned} L = & \sum(\text{ray path lengths in water}) + \sum_{j=1}^{N_b+1} \frac{\Delta(\gamma_j)}{\sin \gamma_j} \\ & + \frac{\text{ray path length in bottom}}{n} \quad , \quad (3-16) \end{aligned}$$

where the final term in the summation over  $j$  is to be evaluated according to Eq. (2-81) for the ray displacement upon transmission.

### 3-5.2 The mathematical basis for the multiplicity of lateral waves

An interesting aspect of propagation in a sloping environment is the multiplicity of lateral waves, caused by the change in bottom angle upon each successive reflection. Figure 3-8(a) shows the three possible eigenrays for the ray path with  $N_b = 2$  and  $N_s = 1$ . One is totally reflected at both bottom reflections, and the other two are lateral waves, each of which strikes the bottom near the critical angle on one of its two reflections. Note that the lateral wave at the first bottom reflection subsequently undergoes a *partial* reflection, whereas the lateral wave on the second reflection has already undergone a *total* reflection. Clearly, the latter is stronger under normal circumstances.

Mathematically, these lateral waves are accounted for by keeping track of the Riemann sheets on which  $V$  is calculated for the various bottom reflections. As described in Sec. 2-4.2, the square root term  $\sqrt{n^2 - \sin^2 \theta}$  in  $V$  [see Eq. (2-18)] may be evaluated such that its imaginary part is either positive (the upper Riemann sheet) or negative (the lower Riemann sheet). The two sheets are connected along branch cuts that begin at the branch points at  $\pm\theta_{cr}$ , as shown in Fig. 2-3. Every time an integration path crosses a branch cut in the complex  $\theta$ -plane, one must change Riemann sheets in order to preserve continuity of the function  $V(\theta)$ .

In a sloping environment the reflection coefficient  $V$  is evaluated at different angles for each bottom reflection. For the ray path with  $N_b = 2$ ,  $V$  is evaluated at  $\theta$  on the first reflection, giving rise to branch points at  $\pm\theta_{cr}$ , and at  $\theta - 2\alpha$  on the second reflection, giving rise to branch points at  $\pm\theta_{cr} + 2\alpha$ . A choice of Riemann sheet must be made for each of these two evaluations. Figure 3-8(b) shows the saddle points and steepest descent paths in the complex  $\theta$ -plane for the eigenrays traced in Fig. 3-8(a). In the figure, the axes representing the angle at the second reflection are simply shifted to the right by an amount  $2\alpha$  compared to the axes representing the angle at the first reflection. They have also been artificially shifted upward slightly to allow one to distinguish the two overlapping branch cuts.

The Riemann sheets on which various portions of the steepest descent paths in Fig. 3-8(b) lie are indicated by the plus and minus signs inside parentheses. For example, (+ -) means that evaluation of  $V$  is on the upper Riemann sheet for the first reflection,  $V(\theta)$ , and on the lower Riemann sheet for the second reflection,  $V(\theta - 2\alpha)$ . The contour of integration in Eq. (3-9) requires that the path begin and end on all positive sheets (+ +). Keeping in mind that a change in the appropriate Riemann sheet occurs whenever a path crosses a branch cut, it can be seen that by adding the two lateral wave rays to the totally reflected ray, the correct contour of integration is completed. Note that all three saddle points

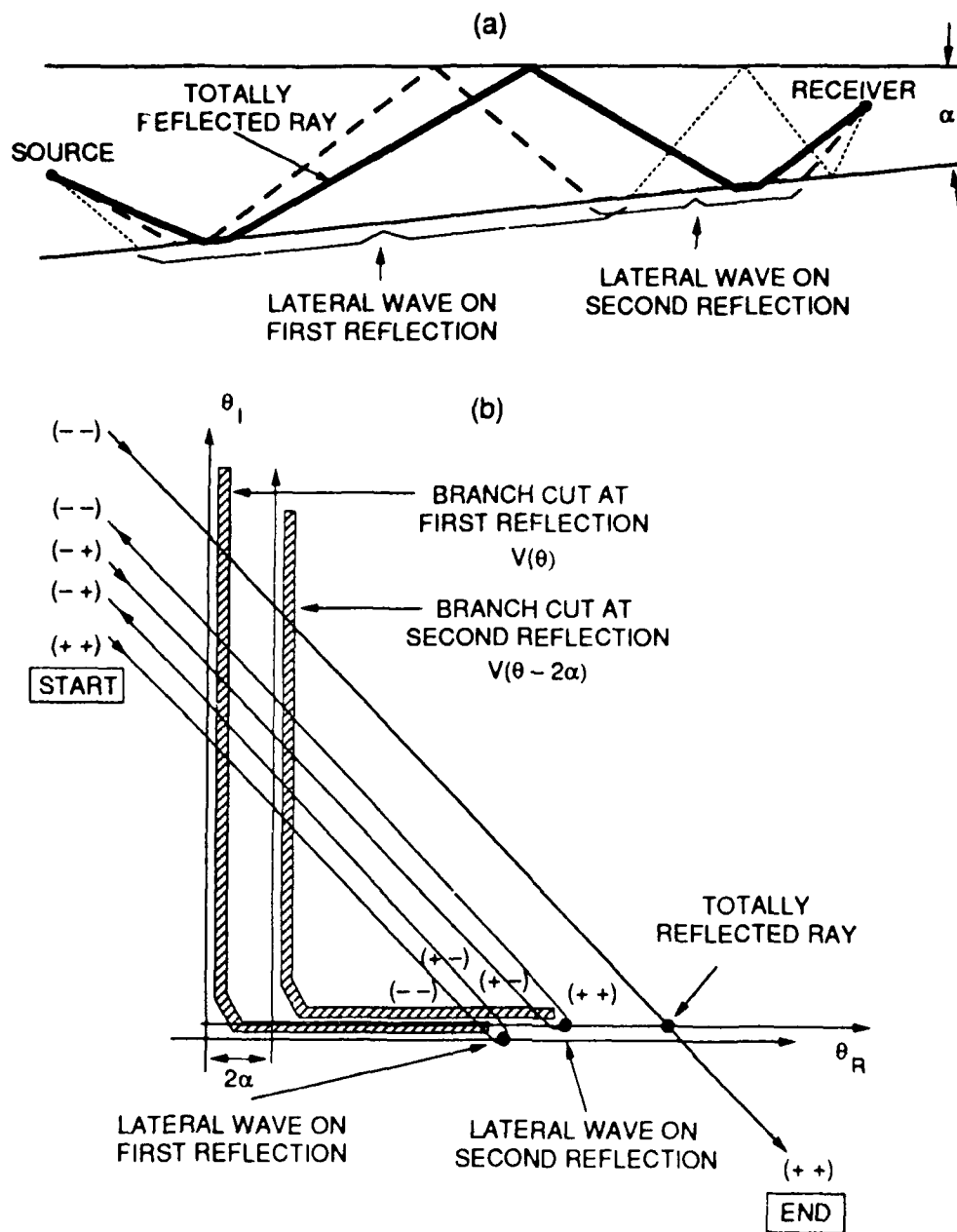


**Figure 3-8** MULTIPLE LATERAL WAVES IN A SLOPING WAVEGUIDE: (a) RAY TRACE OF THE TOTALLY REFLECTED RAY PLUS THE TWO LATERAL WAVE RAYS, (b) SADDLE POINTS AND STEEPEST DESCENT PATHS IN THE COMPLEX  $\theta$ -PLANE.

lie on both positive sheets (+ +). In the general case, there may be as many as  $N_b$  lateral wave rays plus one totally reflected ray for a ray path with  $N_b$  bottom reflections.

The algorithm for evaluating the total field at a series of receivers along a horizontal line in a wedge is similar to that for the flat waveguide outlined in Sec. 3-2. In the present case, evaluation of the field for each ray path begins at the receiver for which  $\theta_0 \approx \theta_{cr} + 2(N_b - 1)\alpha$ . The ray at this angle has total reflections at all interactions except the last, at which the interaction is near the critical angle. We use the same procedure of finding the field at longer ranges first, then shorter ranges. At each successive range, we check for the validity of the saddle point approximation and for the weakness of the eigenray. Presence of the lateral wave rays is detected by checking whether the steepest descent path crosses the appropriate branch cut.

### 3-6 COMPARISON OF MODELS FOR THE SLOPING WAVEGUIDE

The application of the ray method to acoustic propagation in sloping waveguides is the subject of Chapter 4, in which we compare the results predicted by the ray model with those predicted by a two-way coupled mode model. Here, we show just one of the model comparisons. The problems considered are the benchmark problems proposed as a result of a special session for Underwater Acoustics at the 112th Meeting of the Acoustical Society of America in Anaheim, California, 8-12 December, 1986.<sup>32</sup> The environment considered is a wedge of angle  $\alpha = 2.86^\circ$ , with  $n = 0.882$ ,  $m = 1.5$ ,  $h_s = 3.33\lambda$ , and  $z_s = 1.67\lambda$ . We show in Figure 3-9 a comparison for a case of upslope propagation, where  $z_r = 0.5\lambda$  and  $r = 0-67\lambda$ . The agreement is almost perfect, even for receivers in the bottom at ranges beyond  $56.67\lambda$ . The close agreement is strong evidence that the theoretical approach outlined here is valid and has been correctly implemented.

### 3-7 EIGENRAY STRUCTURE IN THE SLOPING WAVEGUIDE

Figure 3-10 illustrates the saddle point structure for a case of upslope propagation in a wedge of angle  $\alpha = 2^\circ$ , with  $n = 0.866$  ( $\theta_{cr} = 60^\circ$ ) and  $m = 1.67$ . The geometric parameters are  $h_s = 5\lambda$ ,  $z_s = 1\lambda$ , and  $z_r = 0.5\lambda$ . Part (a) of the figure shows the saddle points and their steepest descent paths in the complex  $\theta$ -plane for the particular ray path with  $N_b = 3$  bottom reflections and  $N_s = 2$  surface reflections. The receiver range is varied from  $r = 30\lambda$  to  $r = 60\lambda$  in increments of  $2.5\lambda$ , as labeled. Recall that  $\theta$  is the plane wave angle at the *first*

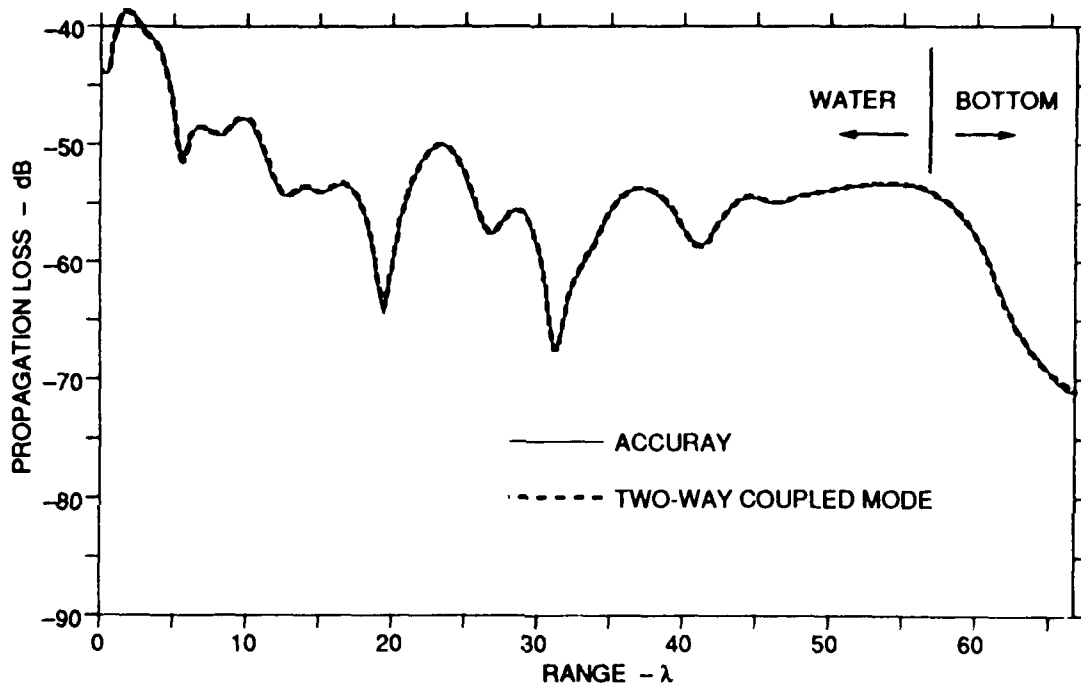


**Figure 3-9** COMPARISON OF THE RAY MODEL (ACCURAY) AND A TWO-WAY COUPLED MODE MODEL FOR UPSLOPE PROPAGATION IN A WEDGE OF ANGLE  $\alpha = 2.86^\circ$ . THE RECEIVER AT THE MAXIMUM RANGE OF  $67 \lambda$  LIES IN THE BOTTOM DIRECTLY BELOW THE APEX OF THE WEDGE.

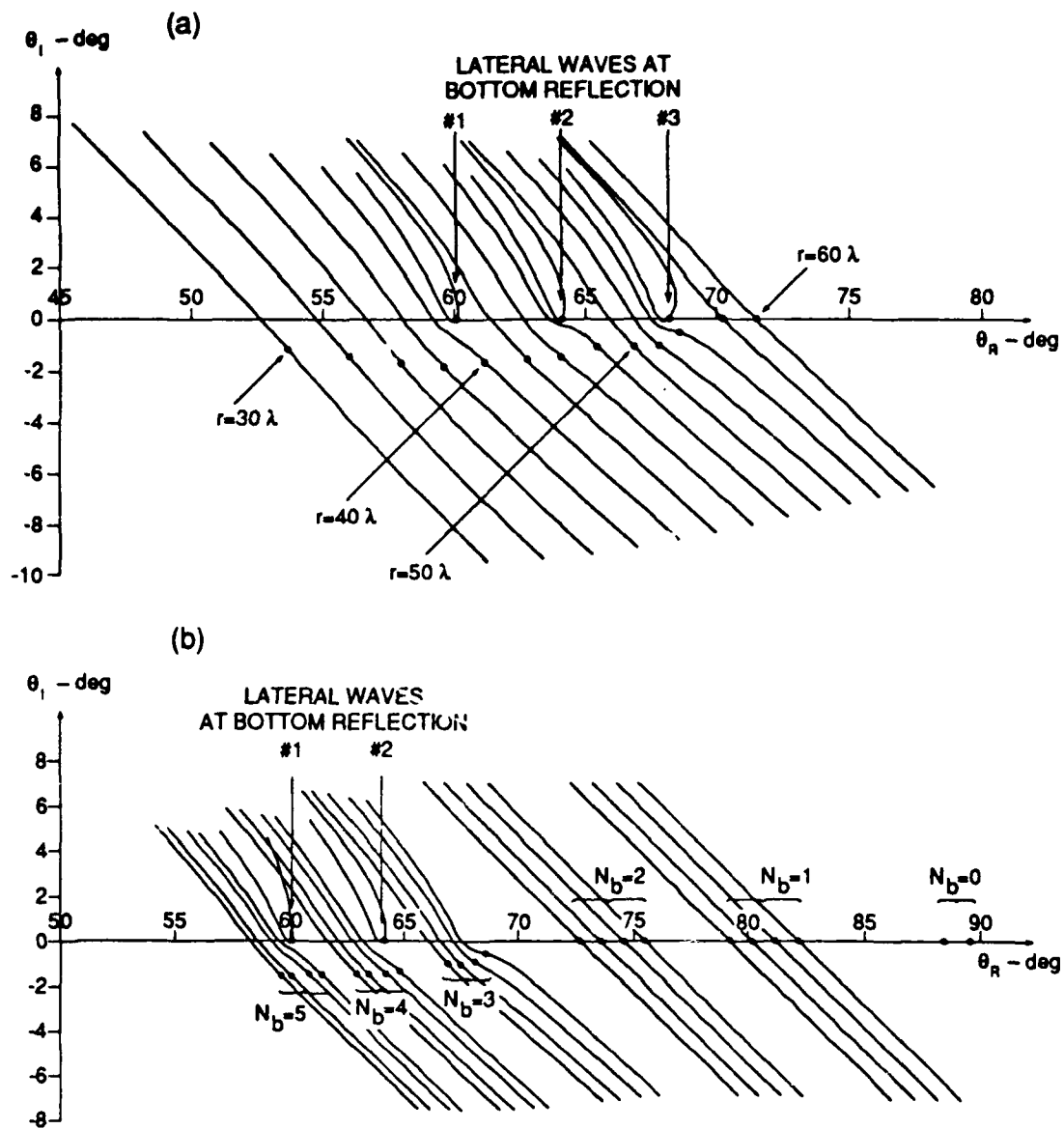


Figure 3-10 EIGENRAY STRUCTURE IN A SLOPING ENVIRONMENT: (a) SADDLE POINTS AT A SERIES OF RANGES FOR THE RAY PATH WITH  $N_b = 3$  AND  $N_s = 2$ , (b) SADDLE POINTS AT RANGE  $r = 55\lambda$  FOR RAY PATHS WITH  $N_b = 0-5$ .

bottom reflection, so the critical angle lies at  $\theta_{cr} = 60^\circ$  for the first reflection, at  $\theta_{cr} + 2\alpha = 64^\circ$  for the second reflection, and at  $\theta_{cr} + 4\alpha = 68^\circ$  for the third reflection.

From Fig. 3-10(a) we can deduce that, as a function of range, the reflected (non-lateral wave) eigenray has all (three) partial reflections for  $r \leq 40\lambda$ , two partial reflections and one total reflection beginning at  $r = 42.5\lambda$ , one partial reflection and two total reflections beginning at  $r = 50\lambda$ , and all total reflections for  $r \geq 57.5\lambda$ . This implies that there are lateral waves at the first bottom reflection for ranges  $r \geq 42.5\lambda$ , at the second bottom reflection for  $r \geq 50\lambda$ , and at the third bottom reflection for  $r \geq 57.5\lambda$ . Since the steepest descent paths of the lateral wave rays tend to overlap, we have drawn only one for each of the three bottom reflections.

Part (b) of Fig. 3-10 shows the saddle points at the particular range  $r = 55\lambda$ . Saddle points that correspond to eigenrays with zero to five bottom interactions are indicated. As in Fig. 3-6 for the flat case, there are groups of four saddle points for each value of  $N_b$ , representing the four multipath eigenrays. As  $N_b$  increases, the eigenray incident angles become smaller. An eigenray with saddle point  $\gamma$  undergoes its  $j$ th bottom reflection at angle  $\gamma_j = \gamma - 2(j-1)\alpha$ , so it is easy to determine the number of partial reflections a given eigenray suffers. For example, all four eigenrays with  $N_b = 2$  experience no partial reflections, those with  $N_b = 3$  experience one, and those with  $N_b = 4$  experience three. Again, only one of the 16 lateral waves at  $\theta = 60^\circ$  is shown, and only one of the eight lateral waves at  $\theta = 64^\circ$  is shown.

This phenomenon of eigenrays with larger numbers of bottom interactions "gradually" undergoing more partial reflections is in contrast to the flat waveguide case, in which the transition from rays with all total reflections to all partial reflections is sudden. An important consequence is that, in a wedge, eigenrays with one or more partial reflections are significant, even at long ranges. In terms of mode theory the partially reflected contributions correspond to modes that are beyond cutoff and in the process of penetrating into the bottom. In the example of Fig. 3-10(b), the rays with one partial reflection ( $N_b = 3$ ) are just 2-4 dB weaker than the totally reflected rays, whereas those with three partial reflections ( $N_b = 4$ ) are 12-16 dB weaker.

### 3-8 CONCLUSIONS

In this chapter we have applied the complex ray methods developed in Chapter 2 to the flat and sloping waveguides common in underwater acoustics applications. For the flat waveguide (the Pekeris model) agreement between the

ray model and the SAFARI model is nearly perfect. Whereas normal mode models that calculate only the discrete spectrum are in error when a mode is near cutoff, the ray model is valid at all ranges. The ray model is also valid when the water depth is as low as half a wavelength.

In the case of a sloping waveguide we have derived the integral expression for each ray field, and have shown the mathematical origin of the multiple lateral waves. In contrast to the flat waveguide, rays in a wedge change angle upon each reflection. Thus, a given ray that is totally reflected on its initial bottom interactions remains significant even after one or two partial reflections. As a result, successful modeling of a wedge environment, even at long ranges, requires accurate calculation of the field in the transition region from total to partial reflection. The validity of the ray method presented here has been demonstrated in Sec. 3-6 by its close agreement with an independent model.

Although the environments considered in this chapter are simple idealizations of the real ocean, the solutions presented here in terms of eigenrays are valuable because they provide physical pictures of the propagation. In contrast, models that numerically solve for the field usually provide little information about the actual mechanisms of propagation. Computationally intensive models, such as those based on finite element methods, the parabolic equation approximation, or coupled mode theory, can be difficult to use with confidence because the accuracy of their solutions may depend on the initial choice of mesh size, number of sample points, number of integration points, or number of modes to consider. Thus, a simple model like the ray model can be very useful in verifying the accuracy of these more versatile and powerful models.

## CHAPTER 4

### RAY MODEL SOLUTIONS TO THE BENCHMARK WEDGE PROBLEMS

#### 4-1 INTRODUCTION

In this chapter we present in more detail the results of applying the ray method developed in Chapters 2 and 3 to the benchmark wedge problems. These results were first reported in Ref. 4. Benchmark problems were proposed at a Special Session for Underwater Acoustics at the 112th Meeting of the Acoustical Society of America in Anaheim, California, 8-12 December, 1986.<sup>32</sup> Their purpose was to assess the validity and accuracy of propagation models currently in use. In the case of the penetrable-bottom wedge, an analytical solution does not exist, so only by comparing approximate solutions obtained from independent methods is it possible to verify the correct solution. In Ref. 33 Jensen and Ferla compare solutions from one-way and two-way coupled mode models and from two models that solve the parabolic wave equation. These models are quite flexible in the environmental geometries to which they can be applied, but they provide limited physical insight into the problem. The ray approach not only constitutes an independent method for solving the problem but, more importantly, provides the user with a physical picture of the propagation paths and mechanisms.

One attractive feature of the ray model is that it provides detailed information about the various eigenrays (rays between source and receiver) that contribute to the total field. The relative strengths of the eigenrays indicate which paths and mechanisms of propagation are significant and which are not. For example, from the eigenray arrival angles one can determine whether the phenomenon of backscatter is important. In a wedge, backscattered eigenrays have paths that travel up the slope, past the receiver, and then back down the slope before striking the receiver. This propagation in the "backward" direction is relevant because some models are intrinsically unable to include such a phenomenon. In fact, in Ref. 33 the difference (of 2 dB or less) between the one-way and two-

way versions of coupled mode theory is assumed to be due to backscatter. But in Sec. 4-5 we will show that backscatter is definitely *not* a factor in the penetrable wedge problems proposed.

Another practical aspect of wedge propagation addressed by the ray model is the importance of the lateral wave field. The strengths of the various lateral wave contributions to the field at a particular point can be evaluated for lossy as well as lossless wedge bottoms. Besides the eigenray strengths, the ray model also computes eigenray travel times, which indicate what the transient response to a narrowband pulse would be. Since the lateral wave contributions arrive earliest, their presence may be noticeable in the time domain even if their amplitudes are much weaker than those of the waterborne eigenrays. When measuring a transient signal in an oceanic wedge, comparisons of lateral wave arrivals with ray model simulations might be used to determine the acoustic parameters of the bottom.

The ray model differs from most numerical models in several key respects. First, it is able to find the field in a pointwise manner; *i.e.*, it is not based on a marching algorithm that must find the field at all points between a particular source and receiver. Thus, for applications where the field at only a handful of points is desired, the ray approach is likely to be the most efficient. Second, the ray model is *more* efficient at higher frequencies, and its memory requirements are independent of frequency. Most numerical models require more computation time at higher frequencies and are limited at high frequencies by the storage capacity of the particular computer on which they are implemented. Further details on efficiency considerations will be given in Sec. 4-4.

## 4-2 THE BENCHMARK WEDGE PROBLEMS

Three wedge problems were proposed as benchmarks. The first, which we will not discuss, is the "ideal" wedge, which has a pressure-release bottom as well as surface. The second two problems represent more realistic models for coastal and continental shelf regions of the ocean, where the bottom is usually sandy. In the second benchmark problem the bottom is penetrable but with no attenuation, while in the third problem the bottom possesses an attenuation of 0.5 dB/ $\lambda$ . The wedge geometry is shown in Fig. 4-1. The wedge angle is  $\alpha = 2.86^\circ$ ; the frequency is 25 Hz; the sound speeds in the water and bottom are  $c=1500$  m/s and  $c_1=1700$  m/s, respectively, such that  $n = 0.88235$  and  $\theta_{cr} = 61.93^\circ$ ; and the density ratio is  $m = \rho_1/\rho = 1.5$ . A point source is located 100 m below the surface at a range where the total water depth is 200 m. Propagation loss is to be calculated in the upslope direction along horizontal lines 30 m and 150 m below

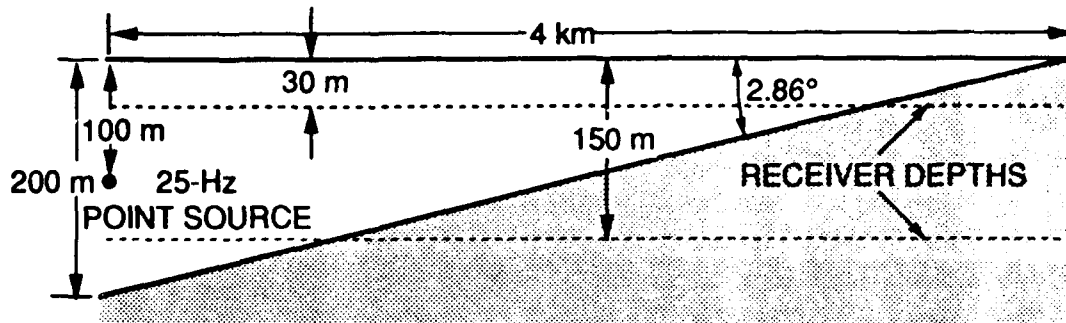


Figure 4-1 GEOMETRY FOR THE BENCHMARK WEDGE PROBLEMS PROPOSED BY THE ACOUSTICAL SOCIETY OF AMERICA.

the water surface. The horizontal range  $r$  extends from zero at the source to 4 km directly below the apex of the wedge. At the depth of 30 m, receivers are in the water for  $r < 3.4$  km and in the bottom for  $r > 3.4$  km. At the depth of 150 m, receivers enter the bottom at a range  $r=1.0$  km.

When the dimensions of the wedge are expressed in terms of the wavelength  $\lambda=60$  m, one sees that this is indeed a low-frequency environment. The total water depth decreases from just  $3\frac{1}{3}\lambda$  at the source to zero at the apex, and the total horizontal range from source to apex is  $66\frac{2}{3}\lambda$ . If normal modes are calculated at each range as though the water depth were constant (modes for the Pekeris model), then at the source there would be just three trapped modes. Mode 3 would be cut off at a range of  $r=0.81$  km, mode 2 would be cut off at  $r=2.09$  km, and mode 1 would be cut off at  $r=3.36$  km.

#### 4-3 COMPARISONS BETWEEN MODELS

At the time the benchmark problems were proposed (December 1986) the following propagation models that could be applied to range-dependent environments were available:<sup>33</sup> (1) adiabatic normal mode models, (2) coupled normal mode models [one-way and two-way versions], (3) models based on the parabolic equation (PE) approximation [narrow or wide-angle formulations and split-step or finite-difference implementations], (4) finite-difference solutions to the full wave equation, and (5) finite-element solutions to the full wave equation. Solutions provided by the adiabatic mode models are not expected to be accurate due to the simplifying assumptions on which the models are based. The PE models should be reasonably accurate, but their intrinsic limitation on the angular spectrum may introduce error in a sloping environment. The finite-difference and finite-element methods should, theoretically, provide exact solutions, but according to Ref. 33

the existing programs were too computer intensive to apply to these problems. The most accurate solution available is from a two-way coupled mode model, originally developed by R. B. Evans,<sup>34,35</sup> and run for the benchmark problems by Jensen and Ferla.<sup>33</sup> There is also a one-way version of the coupled mode model which is more efficient but which ignores propagation in the backward direction.

In this section we compare solutions from the ray model to solutions from the two-way coupled mode model. The latter set of solutions was kindly provided to the author by Dr. Finn B. Jensen of the SACLANT Undersea Research Center, La Spezia, Italy, in March 1988. Comparisons between the ray model and the two-way coupled mode model for the two receiver depths appear in Fig. 4-2 for the lossless case (Benchmark 2) and in Fig. 4-3 for the lossy case (Benchmark 3). The propagation loss in Figs. 4-2 and 4-3 is referenced to a field of 0 dB at 1 m from a point source in free space. The overall agreement between the two solutions is excellent. In all of the figures, the difference is less than 1 dB. The agreement is especially good at receivers in the water, where the two methods differ by the line thickness or less. The maximum difference of 1 dB occurs deep in the bottom for the lossy case [Fig. 4-3(b)]. Since the methods used by these two models are completely different, their close agreement strongly indicates that each is correct.

To calculate the field at the 400 points in each of the figures, the ray model requires from 8 to 10 minutes on a Cyber 180-830 computer. Jensen and Ferla<sup>33</sup> report that the two-way coupled mode model (run on the FPS-164 array processor) requires 24 hours for the Benchmark 2 cases and 8 hours for the Benchmark 3 cases.

#### 4-4 ACCURACY AND EFFICIENCY CONSIDERATIONS

The accuracy of the ray model is governed by two separate factors: first, the validity of the approximations that were introduced into the theoretical formulation of the problem; and second, the accuracy with which the computer algorithm calculates the ray fields given by the approximate integrals.

As discussed in Sec. 2-7.2, two approximations were introduced into the derivation of the plane wave integral Eq. (3-9) for the ray field in a wedge: (1) the substitution of the asymptotic form of the Hankel function and (2) the evaluation of the  $\sqrt{\sin \theta}$  term at the saddle point  $\gamma$  and its subsequent removal from inside the integral over  $\theta$ . The ultimate result of these approximations was to separate the ray spreading terms  $G_\theta$  and  $G_\phi$  in the two orthogonal directions. Since propagation straight upslope (or downslope) does not introduce any coupling between the ray tube spreadings in these two directions, there should be very little error in this formulation.

As mentioned in Sec. 3-5, we do not account for the field diffracted from

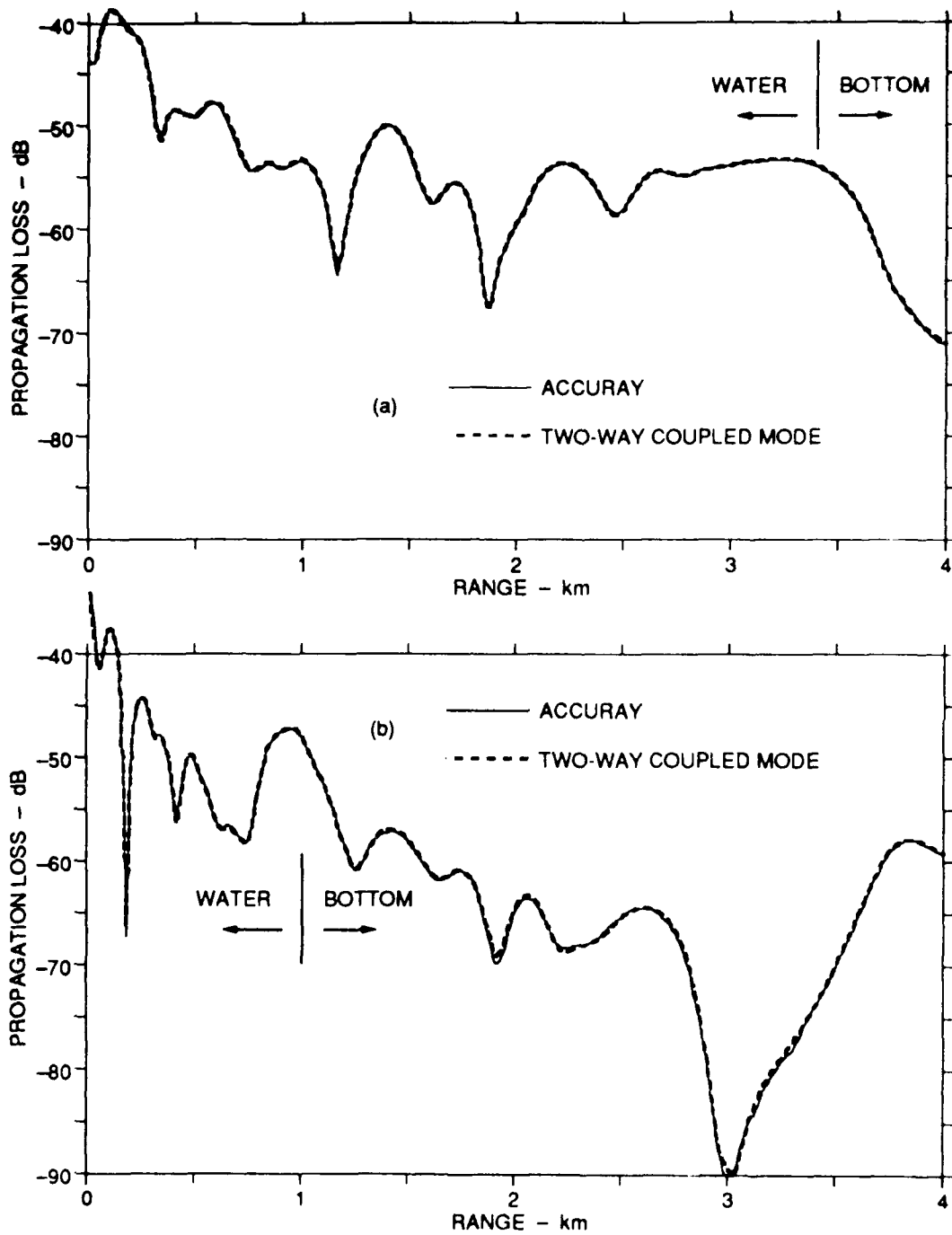


Figure 4.2 Comparison between the Ray Model and the Two-Way Coupled Mode Model for Benchmark 2: (a) 30-m receiver depth, (b) 150-m receiver depth

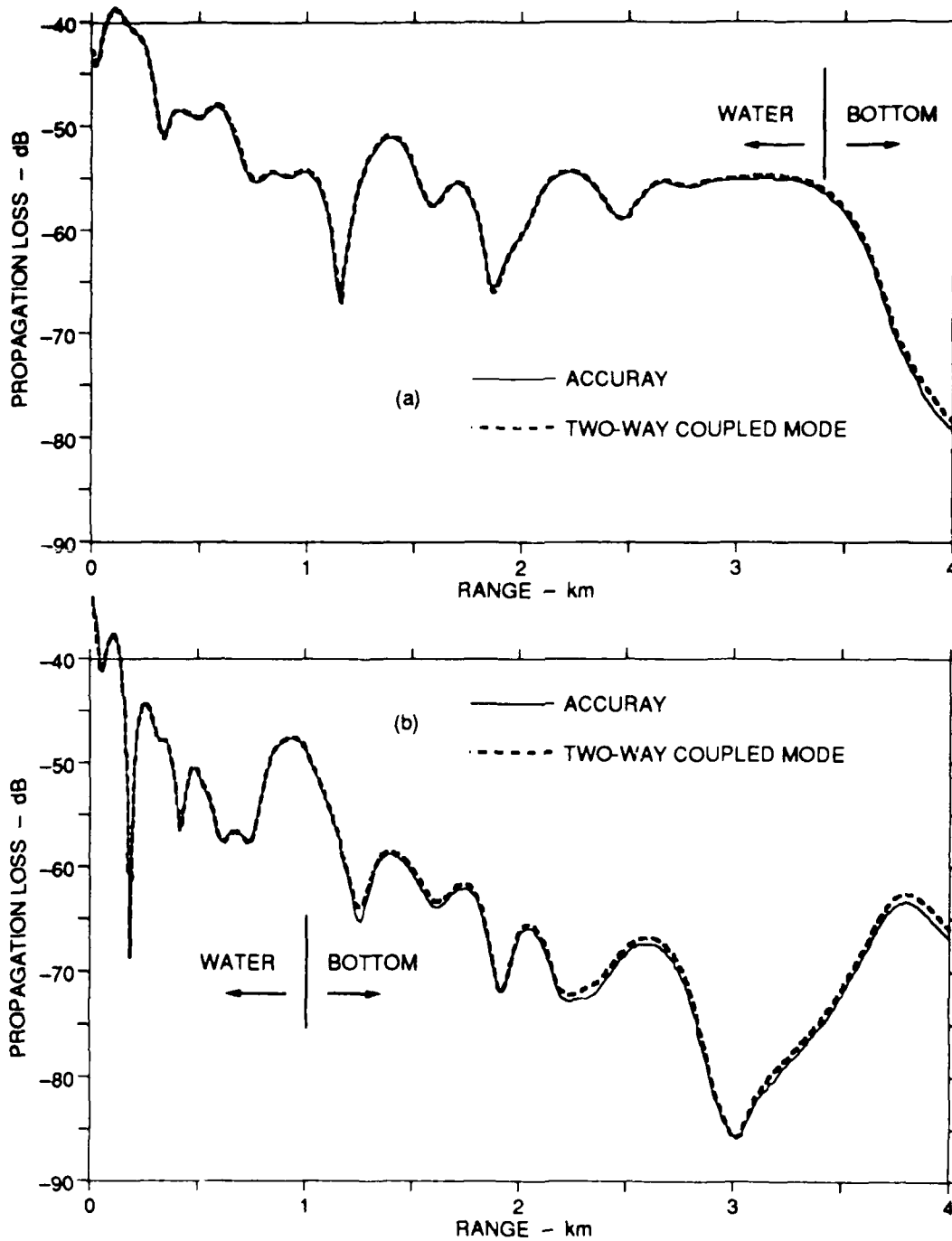


Figure 4.3 COMPARISON BETWEEN THE RAY MODEL AND THE TWO-WAY COUPLED MODE MODEL FOR BENCHMARK 3: (a) 30-m RECEIVER DEPTH, (b) 150-m RECEIVER DEPTH.

the apex of the wedge. This field is produced by energy that travels directly from the point source to the apex and is diffracted from the discontinuity in geometry and boundary conditions there. The existence of the diffracted field is more easily seen when considering wedges with angles greater than  $180^\circ$ , where the diffracted field can be a significant part of the total field. In ocean environments, however, the diffracted field should be insignificant because the wedge angles of interest are typically small and the bottom is penetrable. The diffracted field should not be confused with the *backscattered* field that consists of rays that travel up the slope, "turn around," and travel back down the slope.

The accuracy with which the computer algorithm calculates the total field can be controlled by the user of the ray model. For each receiver the pressure amplitude of the direct path eigenray is used as a reference, and any eigenrays sufficiently weaker than this reference are discarded. The cutoff amplitude is taken to be a certain number of dB (specified by the user) below the reference. For the plots in Figs. 4-2 and 4-3, this "cutoff margin" was set to a very conservative 50 dB, which corresponds to ignoring any eigenray whose pressure amplitude is less than 0.3% of the reference. Including such an eigenray would change the propagation loss by just 0.027 dB. In practical cases, where one may choose to ignore eigenrays that are weaker than 5% of the reference amplitude, a cutoff margin of 26 dB would be specified. Including such an eigenray would change the propagation loss by 0.42 dB. With a less stringent cutoff margin, fewer eigenrays need to be found, and the computation time decreases accordingly.

The time required to find the field at a single receiver depends on the number of significant eigenrays, which in turn depends on the receiver location. At short ranges in the wedge, there are fewer significant eigenrays. Those with a sufficiently large number of bottom interactions are weak because they strike the bottom at steep (small) angles where only *partial* reflection occurs. At longer ranges these eigenrays are significant because their bottom interactions are at shallower (larger) angles where *total* reflection occurs with little or no loss. For example, the field at a range of 0.5 km in Fig. 4-2(a) requires 5 seconds computation time and is composed of contributions from just 14 rays, having up to three bottom interactions. Only seven of these rays are within 26 dB of the strength of the direct ray. In contrast the field at a range of 3 km requires almost 60 seconds computation time and is composed of contributions from 71 rays (having up to seven bottom reflections), of which 22 (having up to five bottom reflections) are within 26 dB of the reference strength.

Another factor that influences the computation time is the frequency. At higher frequencies the ray algorithm is more efficient because the saddle point approximation to the integral (rather than the numerical integration along the

path of steepest descent) can be used more often to evaluate the strengths of the eigenrays. In this respect the ray model is unique since models based on normal mode theory, the PE approximation, or the finite element method can become computationally unfeasible at sufficiently high frequencies.

Finding the field at multiple receivers along a horizontal line is more efficient than finding the field at each receiver separately. One reason is that an eigenray found for one receiver can serve as an initial guess for the corresponding eigenray at a nearby receiver. A second reason is that in order to use the more efficient saddle point approximation to the integral for the eigenray strength, one must first verify its accuracy by comparing it with the result from numerical integration. With just one receiver the numerical integration method must be used all the time. A final reason is that eigenrays weaker than the cutoff level need to be found and evaluated before they can be recognized as being too weak. For example, in the field calculation at the single range of 3 km, 91 eigenrays were actually found, even though only 71 were within 50 dB of the reference strength. For a multiple-receiver computation, the algorithm recognizes that the 20 rays that are too weak do not need to be found at the other receivers.

Increased efficiency is also realized by interpolating eigenrays in range. The field due to a single type of eigenray, specified by its number of surface and bottom reflections, is quite smooth. (It is only when the fields due to rays of different types are added together that the complicated interference patterns evident in Figs. 4-2 and 4-3 emerge.) Consequently, it is possible to find eigenrays exactly at fairly large range intervals and then fill in the intermediate points by interpolating eigenray characteristics such as travel time and geometric loss. Interpolation of eigenrays as a function of frequency can also be used to greatly reduce the computation cost of simulating the propagation of broadband pulses.

Eigenray interpolation resulted in a significant improvement in efficiency when Figs. 4-2 and 4-3 were produced. Eigenrays were found exactly at range intervals of 120 m, but interpolation was used to narrow the interval to 10 m. Thus, the "exact" field was computed at only 1/12 the number of total points. We estimate that the total number of eigenrays required to calculate the field at the 400 points in Fig. 4-2(a) is on the order of 20,000. Using the interpolation scheme, only 1700 of these need to be found and evaluated.

#### 4-5 ANALYSIS OF THE FIELD IN THE WEDGE

An attractive feature of the ray model is that it provides physical insight into how acoustic energy travels from source to receiver. For each receiver position in the wedge, the ray model compiles a list of eigenrays that contribute to the

total field. Mathematically, each eigenray corresponds to a saddle point in the complex  $\theta$ -plane. Geometric interpretation of the quantities associated with the saddle point yield eigenray characteristics such as departure and arrival angles, geometric spreading loss, reflection and transmission loss, and ray travel time (see Sections 2-7 and 3-5). In this section several issues of acoustic propagation in a wedge will be addressed by analyzing the field in terms of eigenrays.

#### 4-5.1 Characteristics of eigenrays in the wedge

As an example of the eigenray information available, the eigenrays for the receiver at a range of 3 km in Fig. 4-2(a) are given in Tables 4-1 and 4-2. Table 4-1 lists the reflected rays while Table 4-2 lists the lateral wave rays. For brevity, only those rays with six or fewer bottom reflections are included in Table 4-1. Rays with more reflections are at least 26 dB weaker than the direct ray. In Table 4-2, only lateral waves with four or fewer bottom reflections are included.

One interesting observation from Table 4-1 is that rays with one partial reflection are still quite strong (rays 15-18 are within 3-8 dB of the direct ray). This indicates that partially reflected energy, corresponding to untrapped or "virtual" modes, *cannot* be ignored in wedge environments. We also see that each additional partial reflection results in a loss of 10-11 dB. Another observation is that the eigenray arrivals are quite close together in the time domain. Rays with up to six bottom reflections arrive within four periods of the direct arrival. This is an indication that the field due to the interference between many ray arrivals can be described in terms of just several normal modes.

From Table 4-2 we see that there are a very large number of lateral wave ray arrivals, but that very few of them are significant compared to the direct ray. The reason for the large number is that a lateral wave is excited whenever energy is incident on the interface at angles close to the critical angle ( $\theta_{cr} = 62^\circ$  in this case). The transmitted energy travels in the bottom parallel to the interface and continuously reradiates energy back into the water at an angle near  $\theta_{cr}$ . In a wedge, a great number of lateral waves are excited by energy that has undergone different numbers of surface and bottom reflections (see, for example, Fig. 1 of Ref. 24). There may be as many as  $N_b$  different lateral wave eigenrays having  $N_b$  bottom interactions. From Table 4-2 we see that the strongest lateral wave ray (ray 22) is about 14 dB weaker than the direct ray. It arrives very close in time to the reflected ray with the same path (ray 14 in Table 4-1). The reflected ray is the last one that does not undergo any partial reflections. The earliest lateral wave ray (ray 1) arrives almost five periods before the direct arrival. Although it is 35 dB weaker, its temporal separation from the stronger arrivals can make it

**Table 4-1** LIST OF THE REFLECTED EIGENRAYS AND THEIR CHARACTERISTICS FOR THE RECEIVER AT A RANGE OF 3 KM IN FIG. 4-2(a). INITIAL DIRECTION,  $d_i$ , SPECIFIES WHETHER THE RAY LEAVES THE SOURCE IN AN UPWARD (U) OR DOWNWARD (D) DIRECTION. ALSO GIVEN ARE THE NUMBER OF SURFACE AND BOTTOM REFLECTIONS,  $N_s$  AND  $N_b$ ; THE NUMBER OF BOTTOM INTERACTIONS AT WHICH PARTIAL REFLECTION OCCURS,  $N_p$ ; THE AMPLITUDE OF THE RAY  $A$  IN dB; THE ANGLES OF INCIDENCE AT THE FIRST AND LAST BOTTOM INTERACTIONS,  $\theta_f$  AND  $\theta_l$ ; THE LOSSES DUE TO GEOMETRIC SPREADING,  $A_g$ , AND REFLECTION,  $A_r$ ; AND THE TRAVEL TIME  $\tau$ , EXPRESSED IN NUMBER OF PERIODS OF THE 25 HZ WAVE AND REFERENCED TO THE ARRIVAL OF THE DIRECT EIGENRAY.

ray	$d_i$	$N_s$	$N_b$	$N_p$	$\theta_f$	$\theta_l$	$A$	$A_g$	$A_r$	$\tau$
1	U	0	0	0	-	-	-69.5	-69.5	0.0	0.00
2	U	1	0	0	-	-	-69.6	-69.6	0.0	0.03
3	D	0	1	0	86.6	86.6	-69.6	-69.6	0.0	0.01
4	U	1	1	0	82.8	82.8	-69.6	-69.6	0.0	0.09
5	D	1	1	0	85.4	85.4	-69.6	-69.6	0.0	0.11
6	U	2	1	0	81.7	81.7	-69.7	-69.7	0.0	0.26
7	D	1	2	0	83.7	78.0	-69.7	-69.7	0.0	0.20
8	U	2	2	0	80.0	74.3	-69.8	-69.8	0.0	0.39
9	D	2	2	0	82.6	76.9	-69.8	-69.8	0.0	0.43
10	U	3	2	0	79.0	73.3	-69.8	-69.8	0.0	0.68
11	D	2	3	0	81.0	69.6	-69.8	-69.8	0.0	0.59
12	U	3	3	0	77.2	65.8	-69.6	-69.6	0.0	0.88
13	D	3	3	0	80.0	68.6	-69.8	-69.8	0.0	0.95
14	U	4	3	0	76.1	64.7	-69.6	-69.6	0.0	1.29
15	D	3	4	1	78.5	61.3	-72.9	-67.0	-5.9	1.20
16	U	4	4	1	75.3	58.1	-75.0	-66.9	-8.1	1.61
17	D	4	4	1	77.8	60.7	-73.6	-67.1	-6.5	1.69
18	U	5	4	1	74.3	57.1	-77.3	-67.8	-9.6	2.14
19	D	4	5	2	77.3	54.4	-81.3	-66.2	-15.1	2.05
20	U	5	5	2	73.9	51.0	-86.3	-66.8	-19.5	2.54
21	D	5	5	2	76.5	53.6	-82.1	-66.4	-15.7	2.63
22	U	6	5	3	73.3	50.4	-87.4	-66.8	-20.6	3.19
23	D	5	6	3	76.0	47.4	-91.7	-65.9	-25.8	3.06
24	U	6	6	4	72.9	44.3	-97.7	-66.6	-31.2	3.65
25	D	6	6	3	75.2	46.6	-93.7	-66.9	-26.8	3.74
26	U	7	6	4	72.4	43.8	-98.8	-66.8	-32.0	4.38

**Table 4-2** LIST OF THE LATERAL WAVE EIGENRAYS AND THEIR CHARACTERISTICS FOR THE RECEIVER AT A RANGE OF 3 KM IN FIG. 4-2(a). SEE TABLE 4-1 FOR AN EXPLANATION OF THE EIGENRAY CHARACTERISTICS.

ray	$d_i$	$N_s$	$N_b$	$N_p$	$\theta_f$	$\theta_l$	$A$	$A_g$	$A_r$	$\tau$
1	D	0	1	0	61.9	61.9	-104.0	-104.0	0.0	-4.96
2	U	1	1	0	61.9	61.9	-102.0	-102.0	0.0	-3.54
3	D	1	1	0	61.9	61.9	-103.5	-103.5	0.0	-4.44
4	U	2	1	0	61.9	61.9	-101.4	-101.4	0.0	-3.02
5	D	1	2	0	67.7	61.9	-98.9	-98.9	0.0	-2.27
6	D	1	2	1	61.9	56.2	-109.6	-103.2	-6.4	-4.07
7	U	2	2	0	67.7	61.9	-95.9	-95.9	0.0	-1.16
8	U	2	2	1	61.9	56.2	-107.5	-101.1	-6.4	-2.65
9	D	2	2	0	67.7	61.9	-98.2	-98.2	0.0	-1.76
10	D	2	2	1	61.9	56.2	-109.1	-102.7	-6.4	-3.47
11	U	3	2	0	67.7	61.9	-94.9	-94.9	0.0	-.64
12	U	3	2	1	61.9	56.2	-106.9	-100.5	-6.4	-2.05
13	D	2	3	0	73.4	62.0	-90.7	-90.7	0.0	-.20
14	D	2	3	1	67.7	56.2	-104.2	-97.8	-6.4	-1.38
15	D	2	3	2	61.9	50.5	-117.2	-102.3	-14.8	-3.05
16	U	3	3	0	73.5	62.1	-85.2	-85.2	0.0	0.60
17	U	3	3	1	67.7	56.2	-100.9	-94.5	-6.4	-.27
18	U	3	3	2	61.9	50.5	-115.0	-100.2	-14.8	-1.63
19	D	3	3	0	73.4	62.0	-89.4	-89.4	0.0	0.31
20	D	3	3	1	67.7	56.2	-103.5	-97.0	-6.4	-.79
21	D	3	3	2	61.9	50.5	-116.7	-101.9	-14.8	-2.37
22	U	4	3	0	73.6	62.2	-83.5	-83.5	0.0	1.12
23	U	4	3	1	67.7	56.2	-99.9	-93.5	-6.4	0.33
24	U	4	3	2	61.9	50.5	-114.4	-99.6	-14.8	-.95
25	D	3	4	1	73.4	56.3	-95.3	-89.0	-6.3	0.69
26	D	3	4	2	67.7	50.5	-111.4	-96.6	-14.8	-.36
27	D	3	4	3	61.9	44.8	-125.9	-101.6	-24.3	-1.90
28	U	4	4	1	73.6	56.5	-89.5	-83.8	-5.7	1.50
29	U	4	4	2	67.7	50.5	-107.8	-93.0	-14.8	0.75
30	U	4	4	3	61.9	44.8	-123.6	-99.2	-24.3	-.48
31	D	4	4	1	73.5	56.3	-94.0	-87.7	-6.3	1.29
32	D	4	4	2	67.7	50.5	-110.7	-95.9	-14.8	0.32
33	D	4	4	3	61.9	44.8	-125.5	-101.1	-24.3	-1.15
34	U	5	4	2	67.7	50.5	-106.9	-92.1	-14.8	1.43
35	U	5	4	3	61.9	44.8	-123.0	-98.7	-24.3	0.27

detectable when the source is a transient pulse.

Although the lateral wave eigenrays are weaker in the presence of bottom attenuation, it is still necessary to include them to obtain an accurate solution. Along the interface, lateral wave rays travel at the speed of sound in the bottom and are attenuated according to the attenuation in the bottom. The eigenray list for Benchmark 3 shows that ray 1 from Table 4-2 suffers an additional 23 dB loss due to the attenuation of 0.5 dB per wavelength  $\lambda$  in the bottom. This translates to a path length along the interface of  $46\lambda$  or 2.76 km, which is reasonable for a receiver at a total range of 3 km. The strongest lateral wave ray in Table 4-2 (ray 22) is reduced by 6 dB as a result of attenuation, which makes it 20 dB weaker than the direct ray. Ignoring such a ray would have a noticeable effect on the total propagation loss.

#### 4-5.2 Eigenrays in the bottom

The eigenrays that make up the total field at a receiver in the bottom are listed in Table 4-3. The receiver is at a range of 3.45 km and a depth of 30 m; it lies about 2.5 m, or  $0.042\lambda$ , below the interface. Only eigenrays with 7 or fewer bottom reflections are included in the table. The number  $N_b$  does include the final bottom interaction at which transmission (or evanescent leakage) takes place. The four types of rays (see Sec. 2-8.2) listed in Table 4-3 are: "TR" for transmitted, "LW" for lateral wave, and "EV" for evanescent. The two rays labeled "EV<sub>2</sub>" represent additional evanescent ray saddle points and are described in Sec. 2-8.2.

Some general characteristics of the eigenrays in Table 4-3 will now be described. In upslope propagation the evanescent rays have total reflections at all of their bottom interactions. At a fixed receiver, the strongest evanescent eigenray (ray 20) is the one with the most reflections and the steepest angle. Compared to the transmitted rays with the same ray path, the evanescent rays arrive later due to the fact that more of their paths are in the slower medium. This is most apparent for the rays that travel direct from the source into the bottom: evanescent ray 2 arrives 6 periods later than transmitted ray 1. For the present case, where the receiver is very close to the interface, the evanescent rays are stronger than the corresponding transmitted rays. For receivers deeper than several wavelengths, the evanescent rays are typically negligible.

The lateral wave rays listed in Table 4-3 arise from energy that undergoes a lateral wave reflection and then a subsequent transmission into the bottom. For example, rays 9 and 12 are reflected as lateral waves at the critical angle  $\theta_{cr} = 61.9^\circ$  on their first bottom interaction and are transmitted into the bottom on their second bottom interaction at angle  $\theta_{cr} - 2\alpha = 56.2^\circ$ . Rays 15 and 18 have total

**Table 4-3 LIST OF EIGENRAYS AND THEIR CHARACTERISTICS FOR THE RECEIVER IN THE BOTTOM AT A RANGE OF 3.45 KM IN FIG. 4-2(a). SEE TABLE 4-1 FOR AN EXPLANATION OF THE EIGENRAY CHARACTERISTICS.**

ray	type	$d_i$	$N_s$	$N_b$	$N_p$	$\theta_f$	$\theta_t$	$A$	$A_g$	$A_r$	$\tau$
1	TR	D	0	1	1	61.9	61.9	-105.6	-111.6	6.0	.00
2	EV	D	0	1	0	86.6	86.6	-83.9	-77.5	-6.4	6.01
3	EV <sub>2</sub>	D	0	1	0	91.2	91.2	-94.7	-82.0	-12.7	5.97
4	TR	U	1	1	1	61.9	61.9	-104.1	-110.1	6.0	1.42
5	EV	U	1	1	0	84.2	84.2	-76.8	-73.6	3.1	6.04
6	EV <sub>2</sub>	U	1	1	0	90.4	90.4	-102.3	-86.1	-16.2	5.80
7	TR	D	1	2	1	67.6	61.9	-101.7	-107.7	6.0	2.69
8	EV	D	1	2	0	85.9	80.2	-71.8	-73.0	1.2	6.07
9	LW	D	1	2	1	61.9	56.2	-102.9	-106.3	3.4	.49
10	TR	U	2	2	1	67.6	61.9	-99.4	-105.5	6.0	3.80
11	EV	U	2	2	0	82.7	77.0	-69.7	-72.5	2.8	6.15
12	LW	U	2	2	1	61.9	56.2	-101.2	-104.6	3.4	1.91
13	TR	D	2	3	1	73.4	61.9	-95.7	-101.7	6.0	4.75
14	EV	D	2	3	0	84.2	72.8	-68.0	-72.5	4.6	6.22
15	LW	D	2	3	1	67.7	56.2	-98.6	-101.9	3.4	3.17
16	TR	U	3	3	1	73.4	61.9	-91.9	-97.9	6.0	5.55
17	EV	U	3	3	0	81.0	69.6	-66.9	-72.2	5.3	6.36
18	LW	U	3	3	1	67.7	56.2	-96.0	-99.4	3.4	4.29
19	TR	D	3	4	1	79.1	62.0	-85.2	-91.2	5.9	6.18
20	EV	D	3	4	0	82.5	65.4	-65.8	-72.1	6.3	6.47
21	LW	D	3	4	1	73.4	56.2	-92.0	-95.4	3.4	5.24
22	TR	U	4	4	1	79.0	61.8	-66.3	-70.1	3.9	6.64
23	LW	U	4	4	1	73.4	56.3	-87.7	-91.2	3.4	6.04
24	TR	D	4	5	1	81.0	58.1	-67.0	-69.6	2.6	6.82
25	LW	U	4	5	1	79.4	56.5	-80.7	-84.3	3.7	6.69
26	TR	U	5	5	2	78.3	55.4	-71.0	-68.1	-2.8	7.10
27	LW	U	5	5	2	73.4	50.5	-94.0	-90.4	-3.5	6.59
28	TR	D	5	6	2	80.1	51.5	-75.3	-68.2	-7.1	7.31
29	LW	D	5	6	3	73.4	44.8	106.3	-94.0	-12.3	6.42
30	TR	U	6	6	3	77.7	49.1	79.1	-67.5	-11.6	7.64
31	LW	U	6	6	3	73.4	44.8	101.8	89.7	12.2	7.22
32	TR	D	6	7	3	79.6	45.3	84.7	67.0	17.8	7.90
33	LW	D	6	7	4	73.4	39.1	115.4	93.4	21.9	7.41
34	TR	U	7	7	4	77.2	42.9	88.9	67.2	21.7	8.26
35	LW	U	7	7	4	73.4	39.1	110.8	89.0	21.8	7.91

reflections at  $\theta_{cr} + 2\alpha = 67.7^\circ$  on their first interaction and then follow the type of path just described. Rays 21 and 23 undergo *two* total reflections, followed by the lateral wave reflection and subsequent transmission, while ray 25 undergoes *three* total reflections before the lateral wave reflection and subsequent transmission. As a last example, ray 27 undergoes two total reflections, a lateral wave reflection, a partial reflection, and then a transmission into the bottom. Most of the lateral wave rays are weak, but the strongest one from Table 4-3 (ray 25) has a strength of  $-80.7$  dB, which is just 15 dB weaker than the strongest ray on the list (ray 20). The multiplicity of lateral waves is an indication of the complexity of the field in the bottom.

The strongest transmitted (TR) rays listed in Table 4-3 are those having four and five bottom interactions. Ray 22 is within 0.5 dB of being the strongest ray at the receiver. Transmitted rays with few bottom interactions (rays 1 and 7, for example) strike the bottom on their last interaction at angles near  $\theta_{cr}$ , penetrate at very shallow angles, and suffer much loss due to geometric spreading ( $A_g$ ). Those with many bottom interactions (rays 30 and 34, for example) suffer much loss due to multiple partial reflections ( $A_r$ ).

#### 4-5.3 Backscatter

An important issue in the penetrable wedge problem is the phenomenon of backscatter. Backscattered energy corresponds to rays that leave the source traveling upslope and eventually strike the receiver traveling downslope. The change in direction occurs as the result of multiple reflections off the sloping bottom. A backscattered eigenray is easily recognized as one that has a *negative* incident angle at its last bottom reflection ( $\theta_i$  in Tables 4-1 and 4-2). A brief analysis of the eigenrays at various ranges indicates that *backscatter is totally insignificant* for the penetrable wedge problems. For the receiver at a range of 3 km in Fig. 4-2(a), the steepest eigenray within 50 dB of the reference strength arrives at an incident angle of  $33^\circ$ . From Table 4-1 we see that the steepest eigenray within 29 dB arrives at  $43.8^\circ$  (ray 26). It is only at very short ranges (less than 0.1 km) that eigenrays traveling vertically are significant.

Using the image method it is easy to find the approximate path of the eigenray that would arrive at the receiver traveling vertically. In Fig. 4-4 we see that the image sources in a wedge lie on a circle centered at the apex. The ray arriving vertically at the receiver is imaged backwards to the closest image source on the circle. From geometry this image source lies approximately at the angle  $\beta$  given by

$$\beta = \arccos(\overline{RA}/\overline{SA}) \quad (4-1)$$

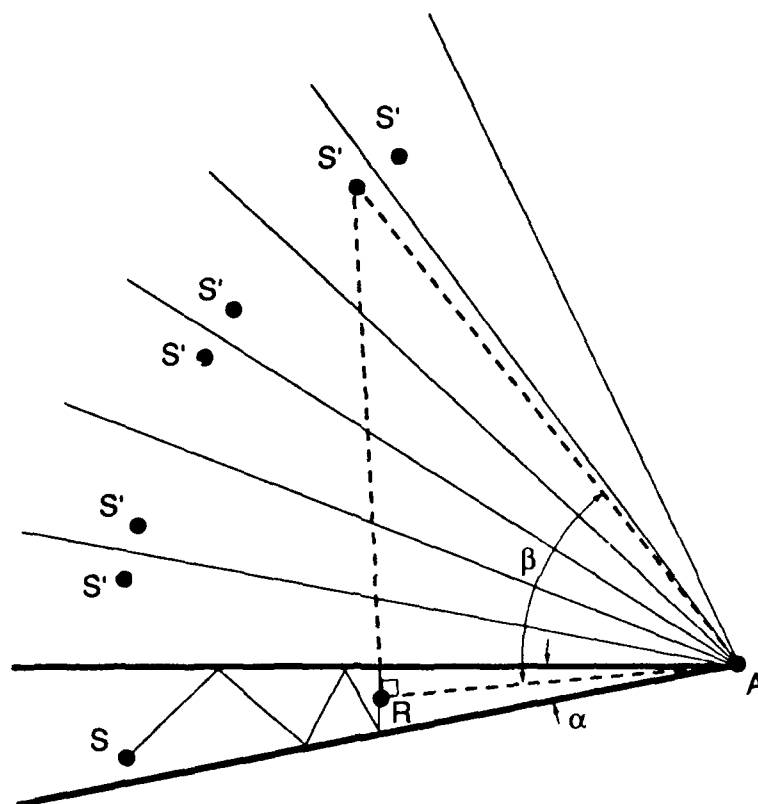


**Figure 4-4** IMAGE METHOD REPRESENTATION OF A BACKSCATTERED RAY. THE ANGLE  $\beta$  IS USED TO FIND THE APPROXIMATE NUMBER OF BOTTOM REFLECTIONS  $N_b$  THE BACKSCATTERED RAY UNDERGOES.

The approximate number of bottom reflections experienced by the first backscattered ray is then  $N_b = \beta/2\alpha$ . For the receiver at 3 km,  $\beta = 75^\circ$  and  $N_b = 13$  bottom reflections. Since the final reflection is at an incident angle close to  $0^\circ$  and the critical angle is at  $62^\circ$ , the last *ten* reflections are at angles steeper than critical ( $62^\circ \div 2\alpha \approx 10$ ). With about 11 dB loss at each partial reflection, it is clear that the backscattered eigenrays are negligible for the present case.

Although backscatter is *not* a factor for the typical water-sand coastal wedge specified in the benchmark problem, the previous analysis indicates the conditions under which backscatter *may* be a factor. First, in a wedge of larger angle  $\alpha$ , fewer reflections are required to make a ray "turn around." Second, a wedge with a higher velocity bottom has a smaller critical angle of incidence, resulting in fewer partial reflections at the bottom interface. And finally, backscattered rays experience less loss when the wedge bottom has less attenuation.

#### 4-6 CONCLUSIONS

The excellent agreement between the ray model and the two-way coupled mode model is strong evidence that both are capable of predicting the acoustic field in a realistic penetrable wedge with an error that is typically much less than 1 dB. The ray model is unique in that it expresses the total field at a point as a sum of ray fields. From a list of eigenrays and their characteristics, the user can gain much insight into the relative importance of the various paths and mechanisms of propagation. Unlike most other models, the ray model is *more* efficient at higher frequencies and is able to find the field at a single point without the need to march through the entire region between the source and receiver.

For the realistic wedge problems that were proposed as benchmarks, an eigenray analysis demonstrates conclusively that backscatter is not a significant mechanism of propagation. This raises a basic question regarding the one-way and two-way versions of coupled mode theory. The intuitive assumption has been that the one-way version neglects energy propagating in the "backward" direction, so that the difference between the two versions is due to the phenomenon of backscatter. However, in the benchmark wedge problems the absence of backscatter calls into question the reason for the difference of up to 2 dB between the one-way and two-way solutions observed in Figs. 5 and 9 of Ref. 33.

The two-way coupled mode model has already been shown to be in good agreement with the analytical solution for the *ideal* wedge (one having perfectly reflecting boundaries).<sup>36</sup> However, propagation in a *penetrable* wedge is quite different in that the reflection process at the bottom is very complex. For example, the entirely new mechanism of lateral wave propagation is introduced, and there

exists a complicated field in the bottom of the wedge that is generated not only by transmission but also by evanescent leakage of totally reflected energy. With such a profound difference between the two problems, it is not clear that the validity of a model for one necessarily guarantees its validity for the other. Thus, the corroboration of the two-way coupled mode model by the ray model for the penetrable wedge is an important result.

## CHAPTER 5

### THE THREE-DIMENSIONAL WEDGE PROBLEM

#### 5-1 INTRODUCTION

The three-dimensional wedge problem is the same as that considered in Sec. 3-5 and Chapter 4 except that the receiver is not required to lie straight upslope or downslope from the source. Detailed theoretical work on this type of geometry has dealt mainly with the special case of perfectly reflecting surface and bottom boundary conditions, a case we shall call the "ideal wedge." In the works of Bradley<sup>37</sup> and Bradley and Hudimac,<sup>38</sup> the authors provide a general review of the literature on the ideal wedge, going back to Sommerfeld's classic work.<sup>39</sup> They go on to present both the ray and mode formulations of the problem as applied to underwater acoustics and to provide approximate mode solutions for various source-receiver configurations. Buckingham<sup>40</sup> derives a similar normal mode formulation but obtains solutions with a more extensive range of validity.

In Ref. 41, Weston studies the phenomenon of horizontal refraction in a wedge, where ray paths, as viewed from above, are bent due to repeated reflections at the wedge surface and bottom. He derives some geometrical characteristics of ray paths in a wedge and qualitatively analyzes the effects of a more realistic bottom possessing attenuation. Harrison<sup>42</sup> analyzes shadow zones in three dimensional environments by restricting ray elevation angles to the discrete values that correspond to the angles associated with the normal modes at the source. In the work of Doolittle, *et al.*,<sup>43</sup> experimental evidence of horizontal refraction is given. Ray theory and Buckingham's normal mode technique are used to analyze the data theoretically. Although the existence of a three-dimensional model based on the parabolic equation approximation<sup>44</sup> was noted, the model was not available for use.

In this chapter we apply the ray methods developed earlier to find the field in the three-dimensional wedge. We find that the dependence of a ray's incident angle at the bottom on both angular variables  $\theta$  and  $\phi$  prevents the

integral over  $\phi$  from being performed analytically. An approximate method of solution is proposed.

## 5-2 DERIVATION OF THE PLANE WAVE INTEGRAL

The geometry for the three-dimensional wedge problem is illustrated in Fig. 5-1(a). The  $z = 0$  plane contains the ocean-air interface, the  $y$ -axis is the shoreline or wedge apex, and the ocean bottom makes an angle  $\alpha$  with the surface. The source lies in the  $y = 0$  plane at  $(x_s, 0, z_s)$ , and the receiver lies at  $(x_r, y_r, z_r)$ . The system of imaged sources is illustrated in Fig. 5-1(b). As in the two-dimensional problem of Sec. 3-5, the images lie on a circle centered on the wedge apex, and each line, of length  $R_1$ , connecting an image source to the receiver represents a ray path of classical ray theory. The direction of the line is specified by the angles  $\theta_0$  and  $\phi_0$ , obtained by translating the line to the origin and defining the usual polar angles  $\theta$  and  $\phi$  as in Fig. 5-1(a). For an image source at coordinates  $(x_{s'}, 0, z_{s'})$ , the three quantities associated with the ray path are computed from simple geometry:

$$R_1 = \sqrt{(x_r - x_{s'})^2 + y_r^2 + (z_r - z_{s'})^2} \quad (5-1a)$$

$$\cos \theta_0 = \frac{z_r - z_{s'}}{R_1} \quad 0 < \theta_0 < \pi \quad (5-1b)$$

$$\cos \phi_0 = \frac{x_r - x_{s'}}{r} \quad \sin \phi_0 = \frac{y_r}{r} \quad 0 < \phi_0 < \pi \quad , \quad (5-1c)$$

where  $r = \sqrt{(x_r - x_{s'})^2 + y_r^2}$ .

The field at the receiver due to a given ray path is constructed by returning to the expression in Eq. (2-16), rewritten here for convenience:

$$p(x, y, z) = \frac{e^{ikR_1}}{R_1} = \frac{ik}{2\pi} \int_{\theta=0}^{\frac{\pi}{2}-i\infty} \int_{\phi=0}^{2\pi} e^{i(k_x x + k_y y + k_z z)} \sin \theta \, d\phi \, d\theta \quad z \geq 0 \quad (5-2)$$

Equation (5-2) expresses the field at receiver position  $(x, y, z)$  due to a point source at the origin as an integral over plane waves. Translating the source position from the origin to  $(x_{s'}, 0, z_{s'})$ , setting the receiver position to  $(x_r, y_r, z_r)$ , and substituting for  $k_x$ ,  $k_y$ , and  $k_z$  from Eqs. (2-13), we rewrite Eq. (5-2) as

$$p(x_r, y_r, z_r) = \frac{ik}{2\pi} \int_{\theta=0}^{\frac{\pi}{2}-i\infty} \int_{\phi=0}^{2\pi} e^{i\Phi(\theta, \phi)} \sin \theta \, d\phi \, d\theta \quad , \quad (5-3)$$

where

$$\Phi(\theta, \phi) = k \{ \sin \theta [(x_r - x_{s'}) \cos \phi + y_r \sin \phi] + (z_r - z_{s'}) \cos \theta \} \quad (5-4)$$

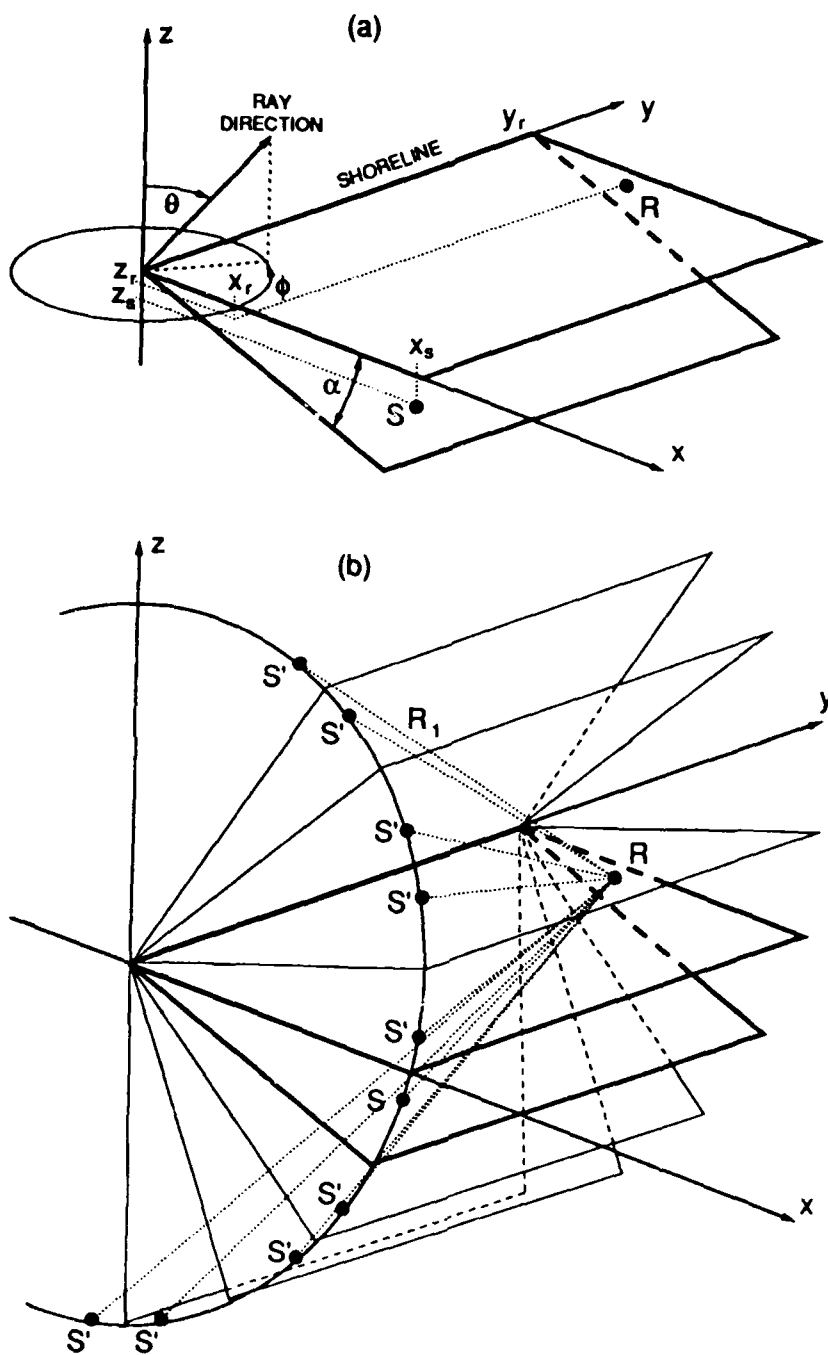


Figure 5-1 GEOMETRY FOR THE THREE-DIMENSIONAL WEDGE PROBLEM: (a) SOURCE-RECEIVER GEOMETRY, (b) SYSTEM OF IMAGES.

Introducing  $\phi_0$  from Eq. (5-1c) into the expression for  $\Phi$ , we obtain

$$\Phi(\theta, \phi) = k[r \sin \theta (\cos \phi_0 \cos \phi + \sin \phi_0 \sin \phi) + z \cos \theta] \quad (5-5)$$

$$= k[r \sin \theta \cos(\phi - \phi_0) + z \cos \theta] \quad (5-6)$$

After substituting  $r = R_1 \sin \theta_0$  and  $z = R_1 \cos \theta_0$ , we finally express  $\Phi$  as

$$\Phi(\theta, \phi) = k R_1 [\sin \theta_0 \sin \theta \cos(\phi - \phi_0) + \cos \theta_0 \cos \theta] \quad (5-7)$$

The next step is to multiply the integrand of the plane wave integral Eq. (5-3) by the appropriate plane wave reflection coefficients. In order to find the angle of incidence with which a given plane wave strikes a given interface, we use the direction cosine representation of a vector  $\vec{v}$ :

$$\vec{v} : (\cos \beta_x, \cos \beta_y, \cos \beta_z) \quad (5-8)$$

where  $\beta_x$  is the angle between  $\vec{v}$  and the positive  $x$ -axis, and  $\beta_y$  and  $\beta_z$  are defined analogously. The angle  $\psi$  between vectors  $\vec{v}_1$  and  $\vec{v}_2$  is then given by

$$\cos \psi = \vec{v}_1 \cdot \vec{v}_2 \quad (5-9)$$

From simple geometry, it can be shown that the direction cosine representation of the ray with angles  $\theta$  and  $\phi$ , as shown in Fig. 5-1(a), is

$$\vec{v}_{\text{ray}}(\theta, \phi) : (\sin \theta \cos \phi, \sin \theta \sin \phi, \cos \theta) \quad (5-10)$$

This ray is perpendicular to the wave fronts of the associated plane wave. We also require the representation of the normals to the interfaces. For the  $j$ th bottom reflection (as counted from the receiver), the normal to the imaged ocean bottom has direction cosines

$$\vec{v}_j : (\sin[(2j-1)\alpha], 0, \pm \cos[(2j-1)\alpha]) \quad (5-11)$$

The positive sign is taken for imaged bottoms that lie below the  $z = 0$  plane (rays traveling upward at the receiver), and the negative sign is taken for imaged bottoms that lie above the  $z = 0$  plane (rays traveling downward at the receiver). The signs are taken so that the normal to each interface points in the same direction as the passage of the ray from source to receiver ( $-\pi/2 < \psi_j < \pi/2$ ). From Eq. (5-9), the incident angle  $\psi_j$  of a plane wave, with angles  $\theta$  and  $\phi$ , at the  $j$ th bottom reflection is then given by

$$\cos \psi_j(\theta, \phi) = \sin \theta \cos \phi \sin[(2j-1)\alpha] \pm \cos \theta \cos[(2j-1)\alpha] \quad (5-12)$$

Note that  $\psi_j = \theta \pm (2j - 1)\alpha$  for the two-dimensional wedge problem, where  $\cos \phi = \pm 1$ .

We now construct the integral representation of the ray field in the three-dimensional wedge for the ray path with  $N_s$  surface reflections and  $N_b$  bottom reflections. To do so, we multiply the integrand of Eq. (5-3) by the reflection coefficients  $V$  evaluated at the angles  $\psi_j$  given in Eq. (5-12):

$$p(\theta_0, \phi_0, R_1) = (-1)^{N_s} \frac{ik}{2\pi} \int_{\theta=0}^{\frac{\pi}{2}-i\infty} \int_{\phi=0}^{2\pi} e^{i\Phi(\theta, \phi)} \left( \prod_{j=1}^{N_b} V[\psi_j(\theta, \phi)] \right) \sin \theta d\phi d\theta, \quad (5-13)$$

where  $\Phi$  is given in Eq. (5-7). Unlike the two-dimensional case, we cannot perform the integration over  $\phi$  analytically because the incident angles  $\psi_j$  are now dependent on  $\phi$  as well as  $\theta$ . This dependence is an indication that the spreading factors of the ray tube in the  $\theta$ - and  $\phi$ -directions are not independent.

As we have done with the previous plane wave integrals, we move the reflection coefficient terms into the exponential factor and write

$$p(\theta_0, \phi_0, R_1) = (-1)^{N_s} \frac{ik}{2\pi} \int_{\theta=0}^{\frac{\pi}{2}-i\infty} \int_{\phi=0}^{2\pi} e^{\rho \tilde{f}(\theta, \phi)} \sin \theta d\phi d\theta, \quad (5-14)$$

where

$$\rho = kR_1 \quad (5-15)$$

$$\begin{aligned} \tilde{f}(\theta, \phi) = & i[\sin \theta_0 \sin \theta \cos(\phi - \phi_0) + \cos \theta_0 \cos \theta] \\ & + \frac{1}{kR_1} \sum_{j=1}^{N_b} \ln V[\psi_j(\theta, \phi)]. \end{aligned} \quad (5-16)$$

Note that the phase function  $\tilde{f}$  is now a function of *two* angular variables  $\theta$  and  $\phi$ . Application of the method of steepest descent in this case is not straightforward because (1) there are two variables of integration and (2) all of the limits of integration are not infinite.

### 5-3 AN APPROXIMATE METHOD OF SOLUTION

We now propose an approximate method for evaluating the ray field given in Eq. (5-14). The first step is to find all the saddle points of the function  $\tilde{f}$  in Eq. (5-16), where a saddle point now consists of a pair of possibly complex angles defined by

$$\frac{\partial \tilde{f}(\theta, \phi)}{\partial \theta} = \frac{\partial \tilde{f}(\theta, \phi)}{\partial \phi} = 0 \quad \text{at } \theta = \gamma, \phi = \chi. \quad (5-17)$$

In order to be able to perform the integration over  $\phi$  for each saddle point, we evaluate the reflection coefficient terms at  $\phi = \chi$  and take them outside the integral over  $\phi$ . This approximation yields the integral

$$p(\theta_0, \phi_0, R_1) = (-1)^{N_s} \frac{ik}{2\pi} \int_{\theta=0}^{\frac{\pi}{2}-i\infty} \left\{ \int_{\phi=0}^{2\pi} e^{ikR_1 \sin \theta_0 \sin \theta \cos(\phi - \phi_0)} d\phi \right\} \\ \exp \left[ kR_1 \left( i \cos \theta_0 \cos \theta + \frac{1}{kR_1} \sum_{j=1}^{N_b} \ln V[\psi_j(\theta, \chi)] \right) \right] \sin \theta d\theta \quad , \quad (5-18)$$

and allows the integral over  $\phi$  to be performed analytically as in Eq. (2-22). At this point, the remainder of the derivation given in Sec. 2-2 follows. The result is an expression very similar to that constructed for the two-dimensional wedge problem in Eq (3-9), except that the reflection coefficients are evaluated at angles  $\psi_j$ , which depend on the saddle point angle  $\chi$ :

$$p(\theta_0, \phi_0, R_1) = (-1)^{N_s} G_\phi \sqrt{\frac{k}{2\pi}} e^{i\frac{\pi}{4}} \int_{-\frac{\pi}{2}+i\infty}^{\frac{\pi}{2}-i\infty} \exp \left[ kR_1 \left( i \cos(\theta - \theta_0) \right. \right. \\ \left. \left. + \frac{1}{kR_1} \sum_{j=1}^{N_b} \ln V[\psi_j(\theta, \chi)] \right) \right] d\theta \quad . \quad (5-19)$$

This integral may be solved using the same saddle point methods used in Sec. 3-5 for the two-dimensional wedge.

A problem arises, however, when applying the saddle point method to Eq. (5-19), where the function  $f$  has the form

$$f(\theta) = i \cos(\theta - \theta_0) + \frac{1}{kR_1} \sum_{j=1}^{N_b} \ln V[\psi_j(\theta, \chi)] \quad . \quad (5-20)$$

Note that the saddle point  $\gamma$  found from the function  $\tilde{f}$  in Eq. (5-16) is a saddle point for  $f$  in Eq. (5-20) only if  $\chi = \phi_0$ . This condition may not be satisfied exactly, especially if the eigenray undergoes displacements at the bottom. We could find a new saddle point  $\gamma$  for  $f$ , or we could keep the old saddle point from  $\tilde{f}$  by replacing  $f$  in Eq. (5-20) by

$$f(\theta) = \tilde{f}(\theta, \phi = \chi) = i[\sin \theta_0 \sin \theta \cos(\chi - \phi_0) + \cos \theta_0 \cos \theta] \\ + \frac{1}{kR_1} \sum_{j=1}^{N_b} \ln V[\psi_j(\theta, \chi)] \quad . \quad (5-21)$$

The latter choice appears to make more sense since the saddle points  $\gamma$  and  $\chi$  that satisfy the original saddle point criterion are preserved.

Some of the details of the calculations required for this problem will now be given. To find the saddle points defined in Eq. (5-17), the partial derivatives of  $\tilde{f}$  in Eq. (5-16) must be calculated. The required expressions are

$$\frac{\partial \tilde{f}}{\partial \theta} = i[\sin \theta_0 \cos \theta \cos(\phi - \phi_0) - \cos \theta_0 \sin \theta] + \frac{1}{kR_1} \sum_{j=1}^{N_b} \frac{V'[\psi_j(\theta, \phi)]}{V[\psi_j(\theta, \phi)]} \frac{\partial \psi_j}{\partial \theta} \quad (5-22)$$

$$\frac{\partial \tilde{f}}{\partial \phi} = -i \sin \theta_0 \sin \theta \sin(\phi - \phi_0) + \frac{1}{kR_1} \sum_{j=1}^{N_b} \frac{V'[\psi_j(\theta, \phi)]}{V[\psi_j(\theta, \phi)]} \frac{\partial \psi_j}{\partial \phi} \quad (5-23)$$

where the partial derivatives of  $\psi_j$ , obtained from Eq. (5-12), are:

$$\frac{\partial \psi_j}{\partial \theta} = -(\cos \theta \cos \phi \sin[(2j-1)\alpha] \mp \sin \theta \cos[(2j-1)\alpha]) / \sin \psi_j \quad (5-24)$$

$$\frac{\partial \psi_j}{\partial \phi} = (\sin \theta \sin \phi \sin[(2j-1)\alpha]) / \sin \psi_j \quad (5-25)$$

The algorithm for finding saddle points would use Taylor series expansions of a function of two variables rather than one.

### 5-3.1 An analysis of the approximation

By removing  $V[\psi_j(\theta, \phi)]$  from the integral over  $\phi$  in Eq. (5-18), we are effectively ignoring any coupling between ray-tube spreading factors in the  $\hat{\theta}$ - and  $\hat{\phi}$ -directions. In reality, this coupling *does* occur for rays that do not travel straight upslope or downslope (those not confined to the  $y = 0$  plane in Fig. 5-1). Coupling between ray-tube spreading factors corresponds to the phenomenon known as horizontal refraction, where the path of a ray as viewed from above the ocean surface appears to bend as the ray undergoes successive reflections. Horizontal refraction occurs when a ray's plane of incidence (the plane containing the ray and the normal to the interface) changes at successive bottom interactions. The approximation we have introduced may result in errors in the calculation of the two eigenray spreading factors  $G_\theta$  and  $G_\phi$  defined in Sec. 2-7.1, but the eigenray paths themselves are not affected since the full, two-dimensional saddle point criterion in Eq. (5-17) is used.

The validity of the approximation made to arrive at Eq. (5-18) depends on how strongly  $V$  varies with  $\phi$  in the neighborhood of the saddle points  $\gamma$  and

$\chi$ . Since  $V'$  is large in the neighborhood of the critical angle, the approximation is potentially poorest when an eigenray undergoes a lateral wave reflection on one of its bottom interactions (where  $\psi_j \approx \theta_{cr}$ ). But since the lateral wave rays make up a small part of the total field, slight errors in their evaluation should not harm the total calculation significantly. It should also be noted that when propagation is mainly upslope or downslope,  $\psi_j$  does not vary significantly with  $\phi$  (as will be shown in the next paragraph), so the lateral wave calculations should exhibit small errors for these cases.

For the more important rays that have saddle points somewhat removed from  $\theta_{cr}$ , the validity of the approximation introduced in Eq. (5-18) depends on how strongly the incident angles  $\psi_j$  vary with  $\phi$ . Thus, the magnitude of  $\partial\psi_j/\partial\phi$  from Eq. (5-25) should be small. We see that this is true when\* (1)  $\gamma$  is small, (2)  $\chi$  is small, or (3)  $(2j - 1)\alpha$  is small. Again, the second condition is satisfied for mainly upslope or downslope propagation. The third condition, which holds for small wedge angles and few bottom reflections, can be satisfied even in the cross-slope case; for example, if  $\theta_{cr}$  is not small and the range between source and receiver is not too large, then eigenrays with large  $N_b$  are not important because they suffer multiple partial reflections.

In cases where eigenrays undergo significant horizontal refraction, the approximation we have outlined here may not be acceptable. In such cases, it appears that a two-dimensional integration must be performed. One problem that arises when attempting to formulate the integrals in terms of the saddle point method is that the limits of integration in Eq. (5-14) are not infinite. When the integral over  $\phi$  cannot be performed analytically, it appears difficult to manipulate the integral over  $\theta$  such that the contour starts at  $-\pi/2 + i\infty$  instead of 0. It remains to be investigated if the method of steepest descent can be applied to the integral whose contour starts at 0.

---

\*The denominator of Eq. (5-25) can make  $\partial\psi_j/\partial\phi$  large only if  $\psi_j$  is close to zero. But this condition implies that the eigenray must be traveling straight upslope or downslope, in which case we have shown that the approximation is valid.

## CHAPTER 6

### THE MODELING OF A DIRECTIONAL SOURCE

#### 6-1 INTRODUCTION

The methods described herein for modeling a uniform acoustic point source may be extended to a directional source by allowing the spatial coordinates of the point source to take on complex values. It was first observed by Deschamps<sup>45</sup> that the solution  $\exp(ikR_1)/R_1$  to the Helmholtz equation represents the field of a Gaussian beam when the distance  $R_1$  is calculated from a complex source position to a real receiver position. By analytic continuation, known exact or asymptotic solutions to point source problems can then be extended to directional source problems by simply introducing the appropriate complex quantities. This method is used in Refs. 46 and 47, where asymptotic forms for the reflection and transmission of electromagnetic beams at a dielectric interface are given and discussed.

#### 6-2 THE FIELD DUE TO A COMPLEX POINT SOURCE IN FREE SPACE

We begin by describing the nature of the field produced by a point source in complex space. Referring to Fig. 6-1, we initially assume the point source to be located at Cartesian coordinates  $(0, 0, ib)$  and consider the field at coordinates  $(x, 0, z)$ . (We have restricted our attention to the  $x$ - $z$  plane with the understanding that the field is cylindrically symmetric about the  $z$ -axis.) The non-zero imaginary part  $b$  of the source coordinate results in a beam whose axis is in the  $z$ -direction. Denoting the source-receiver distance  $R_1$ , we find

$$R_1 = \sqrt{(z - ib)^2 + x^2} \quad , \quad (6-1)$$

where  $R_1$  is now complex. Since we are most often interested in the field near the axis of a directional source, we concentrate on the paraxial region  $x^2 \ll z^2 + b^2$ ,

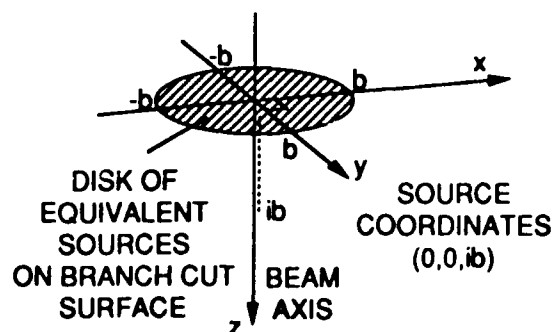


**Figure 6-1** GEOMETRY FOR THE DIRECTIONAL SOURCE. A POINT SOURCE IS PLACED AT  $(x, y, z)$  COORDINATES  $(0, 0, ib)$ , WHICH PRODUCES A BEAM IN THE POSITIVE  $z$ -DIRECTION.

where we can make the approximation

$$\begin{aligned} R_1 &\approx z - ib + \frac{x^2}{2(z - ib)} \\ &= z - ib + \frac{x^2(z + ib)}{2(z^2 + b^2)} \end{aligned} \quad (6-2)$$

Using this expression for  $R_1$  in the exponential of the field due to a point source, we find

$$e^{ikR_1} \approx \exp(kb) \exp \left\{ ikz \left[ 1 + \frac{x^2}{2(z^2 + b^2)} \right] \right\} \exp \left\{ \frac{-x^2}{2} \frac{kb}{(z^2 + b^2)} \right\} \quad (6-3)$$

The first exponential factor on the right hand side of Eq. (6-3) is a constant that can be very large or small, so we normalize the field by the factor  $\exp(-kb)$ . The second exponential factor gives the mathematical form for the phase fronts in the paraxial region. The final exponential factor represents a Gaussian amplitude distribution of the beam about the  $z$ -axis.

The square root operation required to calculate the complex distance  $R_1$  in Eq. (6-1) introduces a branch cut in real space. If we do not limit ourselves to the  $x - z$  plane and define the radicand as

$$s(x, y, z) = (z - ib)^2 + x^2 + y^2 = (z^2 - b^2 + x^2 + y^2) - i(2bz) \quad , \quad (6-4)$$

then the branch points are located at  $(x, y, z)$  values where both the real and imaginary parts of  $s$  vanish. It is easily seen that the branch points form a circle of radius  $b$  in the  $z = 0$  plane defined by  $x^2 + y^2 = b^2$ . We define the branch cuts for the square root operation to be at points where  $\text{Im}[s] = 0$  and  $\text{Re}[s] < 0$ .

The first condition implies that  $z = 0$ , and the second condition implies that  $x^2 + y^2 < b^2$ . The branch cut surface is, therefore, a disk of radius  $b$  in the  $x - y$  plane, lying in real space perpendicular to the beam axis (see Fig. 6-1).

With the branch cut as defined above, the evaluation of  $R_1$  can be made either on the upper Riemann sheet, for which  $\text{Re}[R_1] > 0$ , or on the lower Riemann sheet, for which  $\text{Re}[R_1] < 0$ . When we include the suppressed time dependence  $\exp(-i\omega t)$ , we see that

$$\frac{1}{R_1} e^{i(kR_1 - \omega t)} = \frac{1}{R_1} e^{-k\text{Im}[R_1]} e^{i(k\text{Re}[R_1] - \omega t)} \quad (6-5)$$

From the last exponential factor in Eq. (6-5), we see that on the upper Riemann sheet we have an outgoing wave, while on the lower Riemann sheet we have an incoming wave. The significance of the branch cut is that the field is discontinuous across the cut if all calculations of  $R_1$  are made on the same Riemann sheet. Therefore, points on the branch cut disk in *real* space may be viewed as equivalent sources that together represent the single point source in *imaginary* space.

### 6-3 DETERMINATION OF COMPLEX SOURCE PARAMETERS

The method described here for modeling a directional source may be used to investigate the behavior of beams from a theoretical standpoint or to model an actual acoustic source. In determining the parameters of the complex source to be used, it is appropriate to consider two basic characteristics of the beam to be modeled: (1) a measure of the beamwidth and (2) a measure of the phase front curvature of the beam along its axis. From these two quantities we derive expressions for  $z$  and  $b$ . The latter can be thought of as the distance into *imaginary* space the source is placed, while the former is the axial distance in *real* space from the source to the region where the beam has the desired characteristics.

We define the spatial "variance" or width of the Gaussian beam described in the last exponential factor of Eq. (6-3) by

$$\sigma^2 = \frac{z^2 + b^2}{kb} \quad (6-6)$$

For  $x = \pm\sigma$  the field is down by  $e^{-1/2} = 0.6065$ , or  $-4.34$  dB, from its peak at  $x = 0$ ; for  $x = \pm 2\sigma$  the field is down by  $-17.32$  dB.

The radius of curvature of the phase fronts in the paraxial region can be found from the second exponential factor in Eq. (6-3). The equation for the

curves of constant phase in the  $x$ - $z$  plane is

$$kz \left( 1 + \frac{x^2}{2(z^2 + b^2)} \right) = \text{const} \quad (6-7)$$

The radius of curvature of these phase fronts on the  $z$ -axis may be found by considering a point on the front a small distance  $\Delta x$  from the  $z$ -axis, drawing the tangent to the wavefront at that point, and finding the intersection of the perpendicular to the tangent with the  $z$ -axis (see Fig. 6-2). The distance from

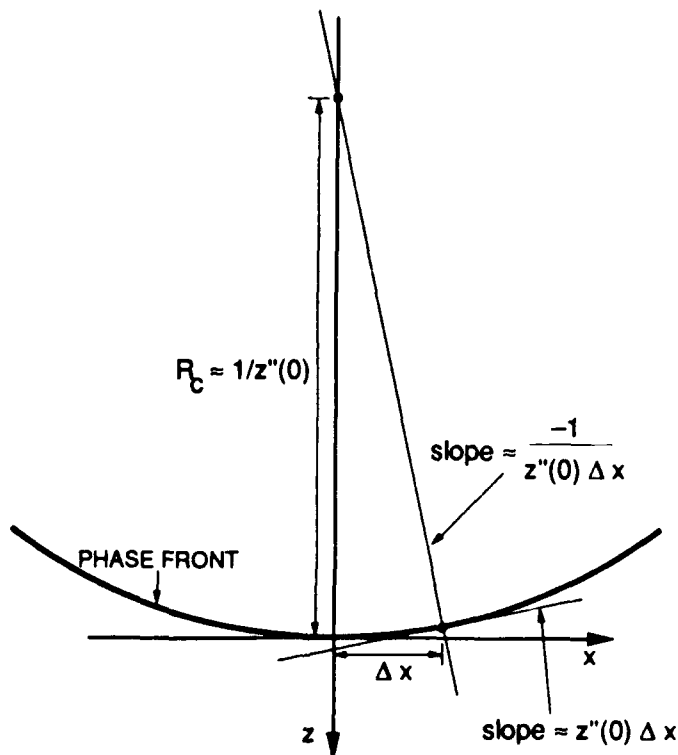


Figure 6-2 CALCULATION OF THE RADIUS OF PHASE FRONT CURVATURE  $R_c$ .

the intersection point to the phase front in the limit of small  $\Delta x$  is then the radius of curvature  $R_c$ . Some simple calculations based on Fig. 6-2 reveal that

$$R_c = \frac{1}{z''(x=0)} \quad (6-8)$$

where  $z(x)$  is the functional form of the phase front and  $z''(x=0)$  is its second derivative with respect to  $x$  evaluated at  $x=0$ . After taking (implicitly) two

derivatives of Eq. (6-7) with respect to  $x$  and evaluating the resulting function at  $x = 0$ , we find that the radius of curvature of the phase fronts on the  $z$ -axis is

$$R_c = \frac{z^2 + b^2}{z} \quad (6-9)$$

Equations 6-6 and 6-9 can be solved simultaneously for the two variables  $z$  and  $b$ :

$$z = \frac{(k\sigma^2)^2 R_c}{R_c^2 + (k\sigma^2)^2} \quad (6-10)$$

$$b = \frac{(k\sigma^2) R_c^2}{R_c^2 + (k\sigma^2)^2} \quad (6-11)$$

Thus, given the quantities  $\sigma$  and  $R_c$  that characterize a beam in a certain region of interest, one can solve for  $z$  and  $b$ . To model the beam by a complex-valued point source, one would place the point source a distance  $z$  in real space and a distance  $b$  in imaginary space away from the region of interest.

#### 6-4 REFLECTED AND TRANSMITTED FIELDS DUE TO AN INCIDENT BEAM

The problem in which we are interested is that of modeling the reflection and transmission of an acoustic beam at a fluid-fluid interface lying in the  $z = 0$  plane. We consider a beam that strikes the interface at the origin of our coordinate system with angle of incidence  $\theta_B$  (see Fig. 6-3). Values of the beamwidth  $\sigma$  and the radius of phase front curvature  $R_c$  in the region of the origin are to be specified or estimated from experimental measurements. Equations (6-10) and (6-11) are then used to calculate  $z$  (which, to avoid confusion with the  $z$ -axis in the present case, we will refer to as  $\rho_0$ ) and  $b$ . After the appropriate rotation and translation of the coordinate system, the point source is placed at  $[x, z]$  coordinates

$$\left[ (-\rho_0 + ib) \sin \theta_B, (-\rho_0 + ib) \cos \theta_B \right] \quad (6-12)$$

Note that we cannot allow the disk of radius  $b$  perpendicular to the beam axis to intersect the interface or else the equivalent sources would extend into the bottom. This restriction requires  $b \sin \theta_B < \rho_0 \cos \theta_B$ . The result is that it may not be possible to model a narrow beam ( $b$  large) incident at small grazing angles ( $\theta_B$  near  $90^\circ$ ).



The method for finding the reflected and transmitted fields due to the directional source is the same as for the point source, except that certain geometrical quantities are complex. Since the source coordinates have been made complex, the distances  $r$  and  $R_1$  and the incident angle  $\theta_0$  in the reflected field expression Eq. (2-46) and in the transmitted field expression Eq. (2-75) are also complex. The fact that  $R_1$  is now complex requires a slight redefinition of the quantities  $\rho$  and  $f(\theta)$  associated with the method of steepest descent in Eq. (2-29). For the directional source case we call these quantities  $\tilde{\rho}$  and  $\tilde{f}(\theta)$ . In order to keep  $\tilde{\rho}$  real, we set

$$\tilde{\rho} = |\rho| = |kR_1| \quad (6-13)$$

and

$$\tilde{f}(\theta) = \frac{\rho}{\tilde{\rho}} f(\theta) = \frac{kR_1}{|kR_1|} f(\theta) \quad (6-14)$$

where  $f(\theta)$  is defined in Eq. (2-47b) for the reflection case and in Eq. (2-76) for the transmission case. Note that Eqs. (6-13) and (6-14) do not constitute an approximation because  $\rho f = \tilde{\rho} \tilde{f}$ . As before, we find the saddle point(s)  $\gamma$  as the value(s) of  $\theta$  for which  $\tilde{f}'(\theta)$  vanishes. The field is then evaluated by either the saddle point approximation or by numerical integration along the path of steepest descent.

## 6-5 EXAMPLES OF COMPUTED FIELDS

Examples of the acoustic field due to the reflection and transmission of a beam incident at a fluid-fluid interface are shown in Figs. 6-4 to 6-6. The figures show contour lines of constant pressure amplitude of the reflected field ( $z < 0$ ) and the transmitted field ( $z > 0$ ) for beams incident on the fluid-fluid interface at angles  $\theta_B = 55^\circ, 62^\circ,$  and  $68^\circ$ . The beam axis intersects the interface [characterized by  $n = 0.866$  ( $\theta_{cr} = 60^\circ$ ) and  $m = 2.0$ ] at the origin. The beam is specified to have a variance of  $\sigma = 5\lambda$  and a radius of wavefront curvature of  $R_c = 50\lambda$ . These characteristics result in an imaginary source coordinate of  $b = 14.5\lambda$  and  $\rho_0 = 45.4\lambda$ . Note that the fields across the interface in Figs. 6-4 to 6-6 are discontinuous. This is because the incident field due to the beam source has not been added to the reflected field above the interface. To test the computer algorithm that produced the contour plots, the *total* field above the interface was calculated, and there was less than a 0.01 dB discontinuity across the interface. The condition of pressure continuity is one of the two boundary conditions imposed at a fluid fluid interface.

The fields shown in Figs. 6-4 to 6-6 are intended to illustrate some basic characteristics of beam interaction at a fluid-fluid interface when the angle of incidence is near the critical angle. Rather than attempt to undertake a comprehensive study of this phenomenon, we mean to show that (1) the complex source approach can be used with few restrictions to find the field due to a directional source, (2) basic characteristics of the reflected and transmitted fields, such as the beam angle and beam displacement at the interface, can be analyzed, and (3) the relative importance of different contributions to the total field at individual points can be evaluated. With regard to the second item, the axes of the reflected and transmitted beams have been estimated by roughly connecting the extremal points on successive contour lines. The beam displacements, which we call  $\Delta$  for reflection and  $\Delta_t$  for transmission, are found by extending the beam axes back to the interface. Although this procedure is not rigorous, it does give a good estimate of the beam characteristics.

In Fig. 6-4 the beam is incident on the interface at an angle of  $55^\circ$ , which is  $5^\circ$  steeper (smaller) than critical incidence. In this case both the reflected and

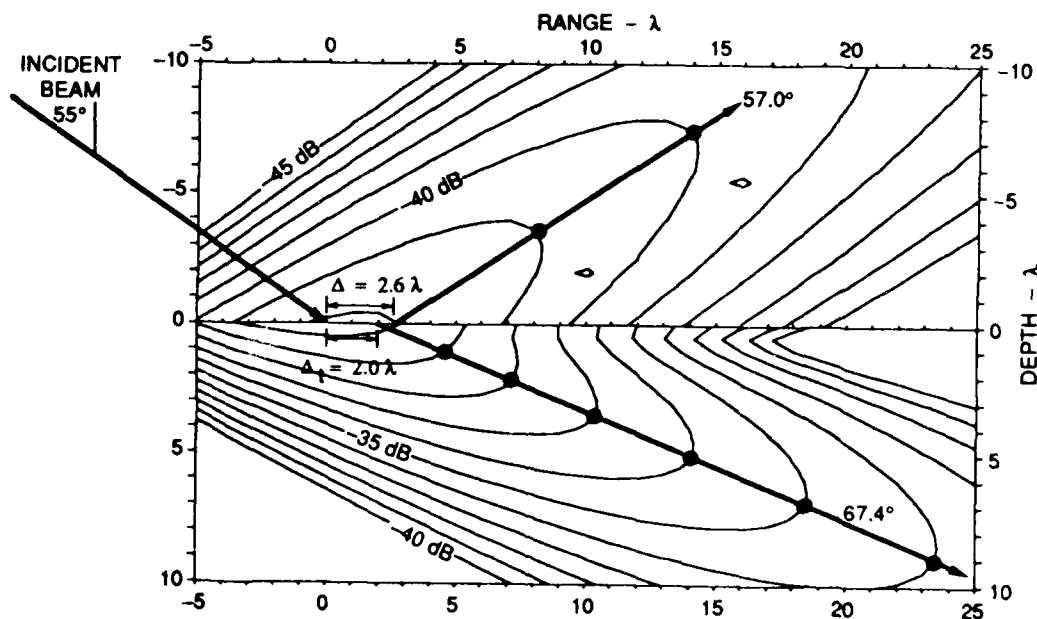


Figure 6-4 REFLECTED AND TRANSMITTED FIELD FOR AN INCIDENT BEAM WITH ANGLE  $\theta_B = 55^\circ$ .

transmitted beams are well defined, even near the interface. The reflected beam has an apparent displacement of  $\Delta = 2.6\lambda$ , while the transmitted beam has an

apparent displacement of  $\Delta_t = 2.0\lambda$ . These results may seem surprising at first because the formulas in Eqs. (2-60) and (2-81) indicate that the ray displacements at these angles should be zero. However, it appears that these phenomena may be explained consistently by considering the facts that the incident beam is actually composed of a spectrum of plane waves about the beam axis and that rays drawn perpendicular to these plane waves strike the interface at different points. For example, the rays incident at  $\theta = 55^\circ$  strike the interface at the origin and are reflected with a plane wave reflection coefficient  $V$  of 0.61, while those at the critical angle  $\theta = 60^\circ$  strike the interface to the right of the origin and are reflected with a coefficient of 1.0. Although the latter rays are initially weaker than the former due to the fact that they are  $5^\circ$  off the beam axis, their larger reflection coefficient could make them stronger after reflection. This may explain not only why the reflected beam axis has been shifted to the right, but also why its angle is slightly larger ( $57^\circ$ ) than that of the incident beam.

In the case of the transmitted beam in Fig. 6-4, one must also consider the spreading introduced by refraction according to Snell's law. For incident angles slightly steeper than critical, a small change in incident angle results in a large change in transmitted angle. The resulting spreading is largest near the critical angle and diminishes toward steeper angles. This factor may explain why the transmitted beam in Fig. 6-4 has a measured angle of  $67.4^\circ$ , while Snell's law predicts an angle of  $71.1^\circ$  for an incident beam at  $55^\circ$ . The shift to a steeper angle may be due to the decreased spreading upon refraction at steeper angles. However, since the steeper rays strike the interface to the left of the beam axis, one might expect the displacement upon transmission to be negative rather than the indicated positive value. Clearly, the present arguments are inadequate to account for both the displacement and angle of the transmitted beam.

Figure 6-5 shows the reflected and transmitted fields for a beam incident at  $62^\circ$ , which is  $2^\circ$  larger than the critical angle. The reflected beam is displaced by  $4.9\lambda$  and has an angle slightly larger than the incident beam. These phenomena can be explained using the same argument as for the  $55^\circ$  beam: the effective beam center is shifted to shallower angles and to the right because the steeper angles experience more loss upon reflection. The ray displacement at  $62^\circ$ , according to Eq. (2-60), should be  $\Delta = 1.9\lambda$ . The measured value of  $\Delta = 4.9\lambda$  is larger due to the additional effect of the beam center being shifted to the right.

The transmitted beam in Fig. 6-5 is displaced  $1.8\lambda$  to the left and has an angle of  $75.4^\circ$ . By checking the eigenray list for receiver positions along the beam axis, it is apparent that the main contribution to the field is from eigenrays that are incident on the interface at angles slightly steeper than the critical angle. These eigenrays represent a part of the beam that strikes the interface to the left

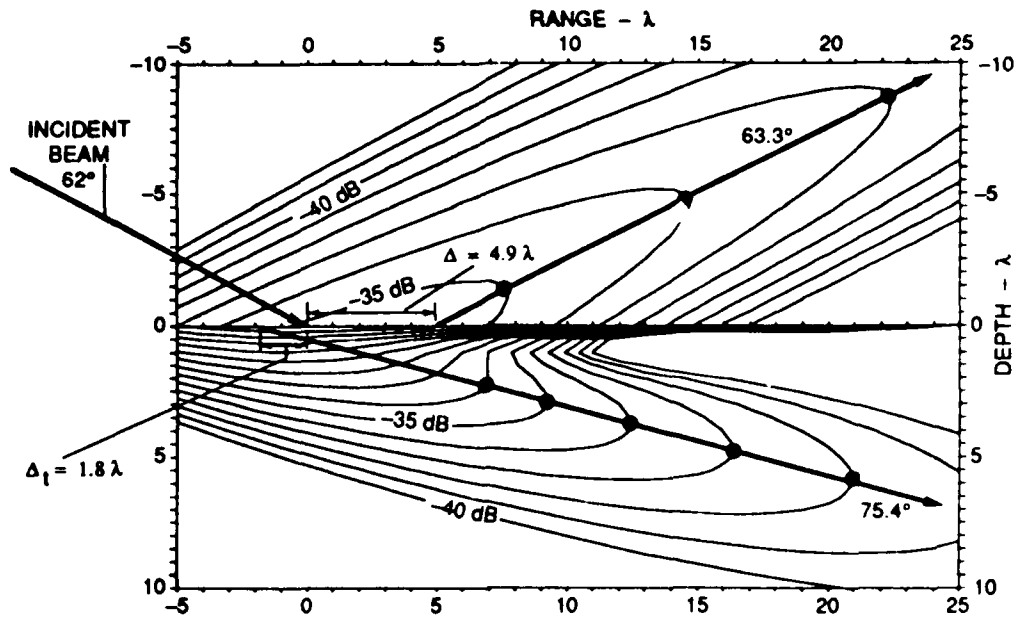
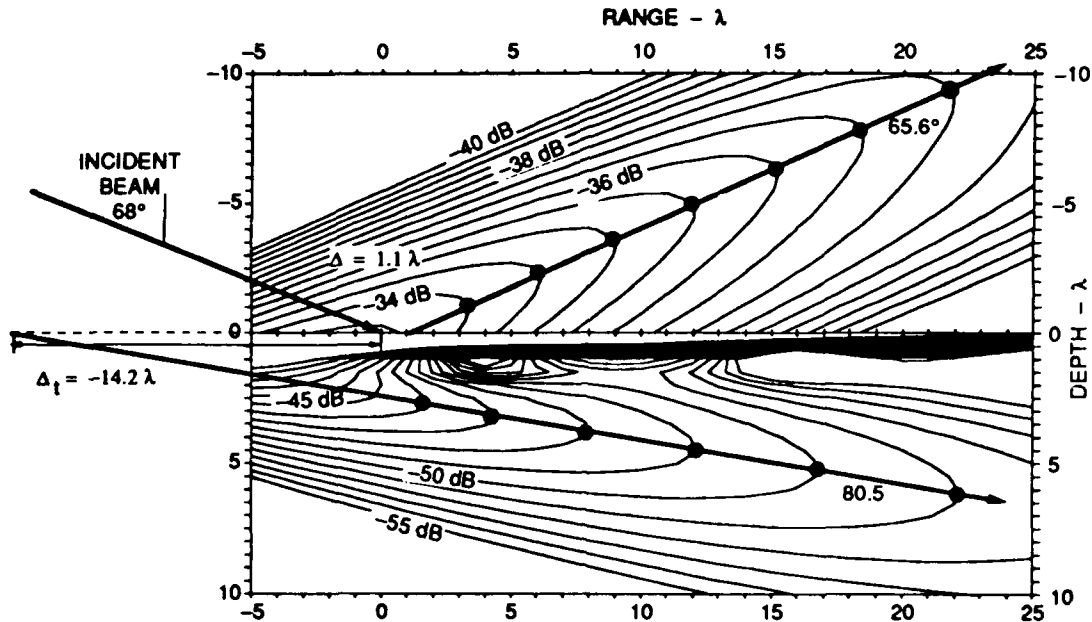


Figure 6-5 REFLECTED AND TRANSMITTED FIELD FOR AN INCIDENT BEAM WITH ANGLE  $\theta_B = 62^\circ$ .

of the main beam axis. Therefore, the apparent displacement of the transmitted beam is negative. The beam angle in the bottom is due to a combination of the following factors: (1) the decreasing spreading loss upon refraction as the incident angle becomes steeper than critical, (2) the decreasing strength of the incident beam for angles steeper than the beam axis, and (3) the decreasing transmission coefficient [see Eq. (2-73)] as the incident angle becomes steeper than critical. The transmitted beam at  $62^\circ$  incidence is shallower than at  $55^\circ$  incidence, as expected.

The final example appears in Fig. 6-6, where the incident beam angle is  $68^\circ$ . The reflected beam has an angle of  $65.6^\circ$ , compared to the value of  $68^\circ$  predicted from Snell's law, and a measured displacement of  $1.1\lambda$ , compared to a predicted ray displacement of  $1.8\lambda$ . By virtue of the fact that the incident beam is  $8^\circ$  shallower than critical, one would expect there to be little shift of the effective beam center due to unequal reflection on opposite sides of the incident beam axis. One possible explanation is that the deviation is due to interference from the lateral wave field. A check of the eigenray list shows that the lateral wave ray is typically 30 dB down from the totally reflected ray along the beam axis. On the interface side of the beam axis the lateral wave ray becomes relatively stronger. This may account for the apparent asymmetry of the reflected beam.

The transmitted beam in Fig. 6-6 has an angle of  $80.5^\circ$  and a negative



**Figure 6-6** REFLECTED AND TRANSMITTED FIELD FOR AN INCIDENT BEAM WITH ANGLE  $\theta_B = 68^\circ$ .

displacement of  $14.2\lambda$ . The displacement to the left is larger in this case than the previous because energy incident at angles steeper than critical strikes the interface farther to the left. The transmitted beam is significantly weaker in this case because the penetrating energy is farther off the beam axis. As expected, incident beams at shallower angles excite transmitted beams at shallower angles.

In both Figs. 6-5 and 6-6, the evanescent field in the upper wavelength or so of the bottom is evident. In the latter case an interference pattern between this field and the transmitted field can be seen, particularly at a range of  $4\lambda$  and a depth of  $1\lambda$ . These effects can make it impossible to trace a beam axis all the way back to the interface. The transmitted beam in such cases is only distinguishable a sufficient distance from the interface.

## 6-6 SADDLE POINT STRUCTURE

The saddle points and their associated steepest descent paths for receivers along several horizontal lines are shown in Figs. 6-7 and 6-8. In each figure both the reflected and transmitted fields two wavelengths from the interface ( $z_r = \pm 2\lambda$ ) are sampled ten times from horizontal ranges of  $-5\lambda$  to  $25\lambda$ . Figure 6-7 is for the incident beam at  $55^\circ$  shown in Fig. 6-4, and Fig. 6-8 is for the incident beam at

68° shown in Fig. 6-6.

The general effect of the source directionality on the saddle point locations is to shift the saddle points farther off the real  $\theta$ -axis as the eigenray angle moves farther off the beam axis. The computer algorithm for finding the correct saddle points must be more sophisticated in the present case because there are more possibilities for how the saddle points migrate and evolve and how the correct contour of integration is completed. For example, in Fig. 6-7(a) the partially reflected eigenrays evolve smoothly into the lateral wave eigenrays, whereas they usually evolve into the totally reflected eigenrays, as they do in Fig. 6-8(a). Another possible scenario is that for the transmitted field, the steepest descent path of the transmitted ray can loop around the critical angle, but both endpoints terminate towards  $\pi/2 - i\infty$  instead of  $-\pi/2 + i\infty$ . In this case, an evanescent ray saddle point must be found on the *lower* Riemann sheet. Its steepest descent path completes the contour of integration.

In Fig. 6-7(a) we see that the reflected field at the largest three ranges requires two saddle points, while the other ranges require only one. The lateral wave rays are about 12 dB weaker than the totally reflected rays. In part (b) of the figure we see that the transmitted field at the largest two ranges requires two saddle points: one transmitted and one evanescent. The latter rays are about 40 dB weaker than the former.

In Fig. 6-8(a) for the reflected field, we see that all but the first receiver have a lateral wave saddle point. Note how the saddle points cross the real  $\theta$ -axis around 68°, which is the angle of the incident beam. For the transmitted field in part (b) we see that all but the first receiver have the evanescent ray as well as the transmitted ray. The evanescent field, however, is 20-29 dB weaker than the transmitted field, despite the fact that the transmitted rays near 60° are quite far off the incident beam axis.

## 6-7 CONCLUSIONS

In this chapter we have demonstrated how our method for modeling acoustic propagation in terms of eigenrays can be modified to accommodate directional sources. We have described the nature of the directional field produced by placing a point source in complex space, and we interpret the associated branch cut surface as a disk of sources in real space equivalent to the point source in complex space. One method for modeling a beam with a given radius of phase front curvature and beamwidth has been proposed. Finally, we have given several examples of the reflected and transmitted fields due to a beam incident on a fluid-fluid interface near the critical angle. The same techniques described in this

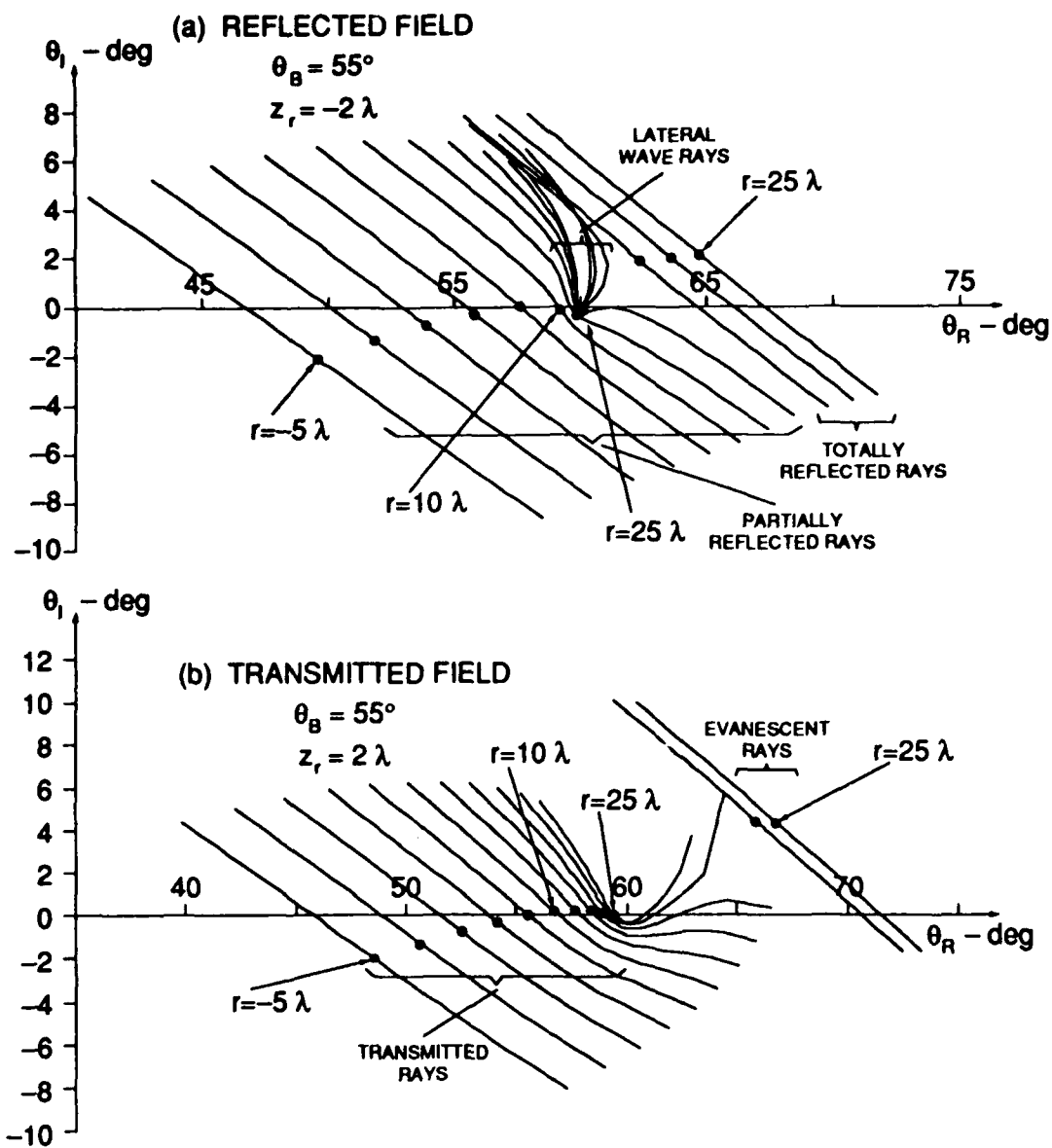
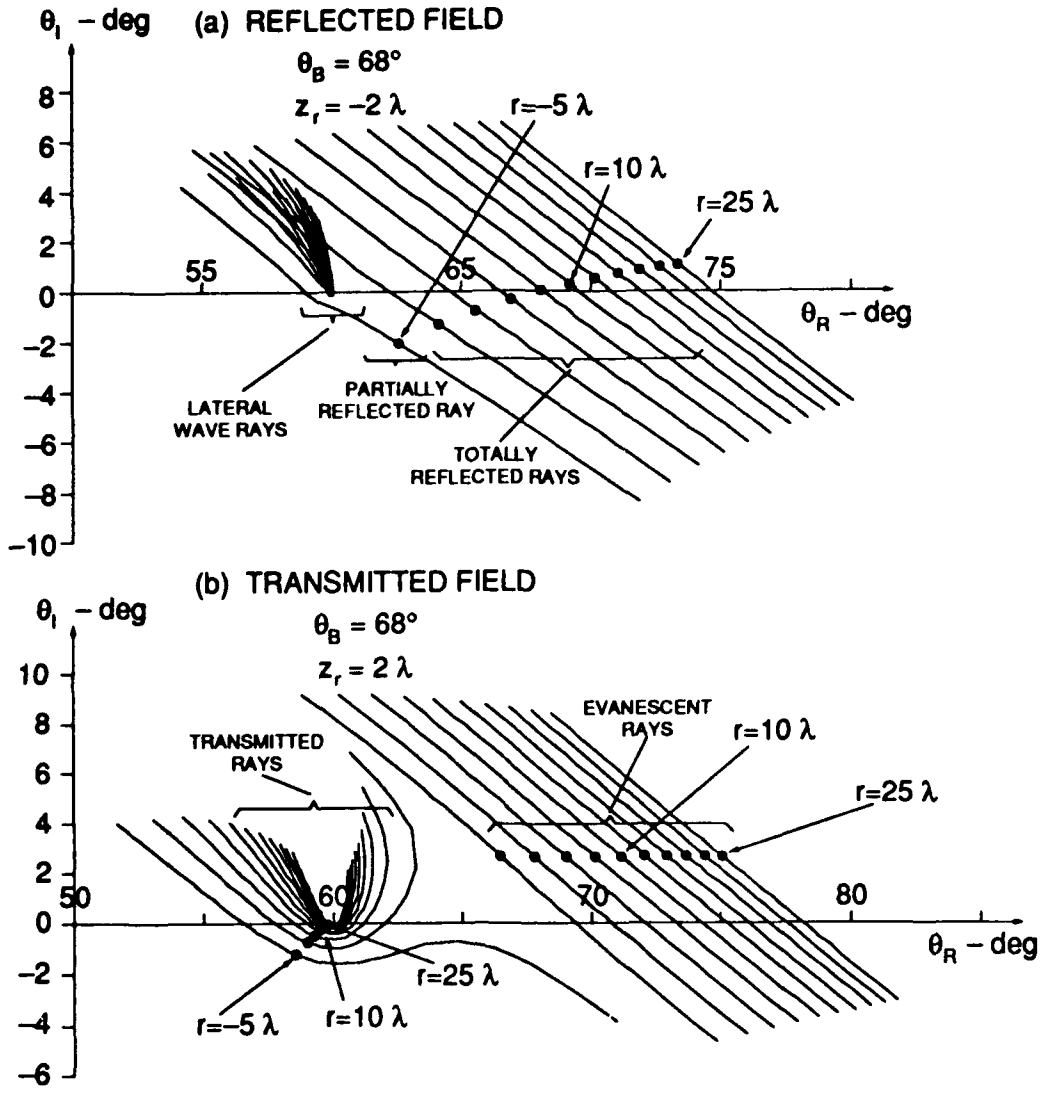


Figure 6-7 SADDLE POINTS AND STEEPEST DESCENT PATHS FOR (a) THE REFLECTED FIELD  $2\lambda$  ABOVE THE INTERFACE AND (b) THE TRANSMITTED FIELD  $2\lambda$  BELOW THE INTERFACE FOR THE  $55^\circ$  INCIDENT BEAM OF FIG. 6-4.



**Figure 6-8** SADDLE POINTS AND STEEPEST DESCENT PATHS FOR (a) THE REFLECTED FIELD  $2\lambda$  ABOVE THE INTERFACE AND (b) THE TRANSMITTED FIELD  $2\lambda$  BELOW THE INTERFACE FOR THE  $68^\circ$  INCIDENT BEAM OF FIG. 6-6.

chapter for modeling a beam incident on a single interface could be used to model a directional source in a flat or sloping waveguide by simply using the appropriate plane wave integrals given in Chapter 3.

## CHAPTER 7

### CONCLUSIONS

The contribution of the research presented in this dissertation is the improvement of ray techniques to model acoustic propagation in shallow water. In Chapter 2 we developed a method for computing the field due to a point source in the presence of a fluid-fluid interface. After formulating plane wave integral representations of the reflected and transmitted fields, we use a variation on the method of steepest descent to solve the integrals. By allowing the reflection and transmission coefficients to influence the saddle point criterion, we obtain a formulation that includes such wave phenomena as the reflected lateral wave field in the water and the evanescent field in the bottom. Each saddle point of a given plane wave integral corresponds to the angle of an eigenray that contributes to the field, and eigenray characteristics such as travel time, propagation path, and reflection or transmission losses are derived. The simple ray interpretation breaks down to a certain degree when the saddle point represents a complex eigenray angle. This occurs when the field is composed of several ray contributions merging into one, or when the field is evanescent. Although saddle point approximations to the integral for the field are usually adequate, a technique for numerical integration along the path of steepest descent must be used in certain cases.

The prime motivation behind developing the ray method for the single-interface problem is to apply it to simple shallow water ocean environments. In Chapter 3 we extended the method to flat and sloping waveguides by constructing the multiple image sources that account for the multiple ray paths between source and receiver in a waveguide. The field due to each ray path is constructed as a plane wave integral in a manner analogous to the single-interface problem. Each integral contains multiple reflection coefficient factors (evaluated at different angles for the sloping case), corresponding to the reflections encountered by the ray path whose contribution the integral represents. We use the same algorithm to evaluate the ray fields in terms of saddle points and their corresponding eigenrays, and we obtain the total field in the waveguide by simply summing the

contributions of the important rays.

We have evaluated our ray model algorithm by comparing its field calculations with those produced by other computer models. For the flat oceanic waveguide, the ray model and the SAFARI fast field program predict almost identical fields. Results from normal mode theory are also compared, and we find that if only the trapped normal modes are calculated (as is usually the case), the mode results can be poor when a mode is near cutoff. We find good agreement between results from the ray model and the SAFARI model even in the very low frequency case where the depth of the water is only half of the acoustic wavelength.

For the sloping waveguide, or wedge, the ray model has been applied to benchmark problems proposed in December 1986 by the Underwater Acoustics community of the Acoustical Society of America. In Chapter 4 we demonstrated excellent agreement between results from the ray model and a model based on two-way coupled mode theory. The independence of the two models' approaches assures us that their common solution is indeed correct. Since there are always uncertainties in the formulation and implementation of any propagation model, the development of a new and independent technique is a valuable contribution to the modeling effort in general. For example, the availability of the coupled mode results was much appreciated when the author was initially implementing the ray algorithm as a computer program.

Besides constituting an independent means of calculating acoustic fields in shallow water, the ray model provides physical insight into the composition of the field in terms of eigenrays and their characteristics. In Chapter 4 we addressed the issues of backscatter, the importance of lateral waves, and the importance of partially reflected rays by analyzing the eigenrays at a particular receiver position in a wedge.

The ray algorithm differs from most numerical models in that it can find the field in a pointwise manner, as opposed to "marching" algorithms that must compute the field at all points between a given source and receiver. In applications where the field at only a handful of points is of interest, the pointwise algorithm can be very advantageous. Another unique feature of the ray method is that it is more efficient at high frequencies than at low frequencies. In addition, the ray method has no large computer memory requirements that are sensitive to the acoustic frequency being modeled.

Ray modeling of propagation in a three-dimensional wedge with a penetrable bottom was described in Chapter 5. In deriving the plane wave integral for each ray field in this case, we find that a double integral over *two* independent plane wave angles must be evaluated. As a consequence, the saddle point criterion requires partial derivatives with respect to two angular variables to vanish.

A more complete investigation of the feasibility of solving the two-dimensional integral remains to be done, but an approximate method that would be straightforward to implement is proposed. Three-dimensional propagation problems are of great interest to the underwater acoustics community, but they pose serious problems to all modeling approaches. Successful application of the ray model to even the simplest three-dimensional problem, the isovelocity wedge, would provide a valuable tool in evaluating other modeling methods.

The final application of the ray method, described in Chapter 6, was to model a directional source by assigning complex spatial coordinates to a point source. Although a point source in complex space is difficult to interpret physically, the mathematical formulation of the problem results in branch cut surfaces in *real* space that can be viewed as containing equivalent sources. The reflected and transmitted fields due to a beam incident on a fluid-fluid interface are computed using the same techniques as for the point source problem. The only modification required is that certain parameters describing the source-receiver geometry must be made complex. Several examples of fields due to beams incident near the critical angle have been computed, and brief analyses have been given. A directional source in a flat or sloping waveguide could be modeled using the same techniques.

The development of the ray methods described in this dissertation has focused on simple environmental models. For example, the ocean water has been assumed isovelocity, interfaces have been assumed flat, the media have been assumed to be fluids, and ocean bottoms have been assumed homogeneous. As a research tool, it is valuable to be able to address such idealized problems with great precision; in practice, however, it is desirable to describe real ocean environments more accurately by including sound velocity gradients in the media, interface roughness, and shear velocities and layering in the ocean bottom. Future research may involve applying some of the concepts and numerical methods developed here to tackle these more difficult problems.

## REFERENCES

- [1] E. K. Westwood, "Complex ray methods for acoustic interaction at a fluid-fluid interface," submitted for publication in *J. Acoust. Soc. Am.*, 1988.
- [2] E. K. Westwood, "Ray methods for flat and sloping oceanic waveguides," submitted for publication in *J. Acoust. Soc. Am.*, 1988.
- [3] E. K. Westwood, "Ray model solutions to the benchmark wedge problems," submitted for publication in *J. Acoust. Soc. Am.*, 1988.
- [4] E. K. Westwood, "The modeling of a shallow-water wedge using complex rays and steepest-descent integration," *J. Acoust. Soc. Am.* **83**, S79-S80 (1988).
- [5] L. M. Brekhovskikh, *Waves in Layered Media* (Academic, New York, 1980), 2nd ed.
- [6] N. Bleistein, "Uniform asymptotic expansions of integrals with stationary point near algebraic singularity," *Comm. Pure Appl. Math.* **19**, 353-370 (1966).
- [7] D. C. Stickler, "Reflected and lateral waves for the Sommerfeld model," *J. Acoust. Soc. Am.* **60**, 1061-1070 (1976).
- [8] S. A. Chin-Bing and J. A. Davis, "Nature of the lateral wave effect on bottom loss measurements," *J. Acoust. Soc. Am.* **71**, 1433-1437 (1982).
- [9] C. T. Tindle and G. E. J. Bold, "Improved ray calculations in shallow water," *J. Acoust. Soc. Am.* **70**, 813-819 (1981).
- [10] C. T. Tindle, "Ray calculations with beam displacement," *J. Acoust. Soc. Am.* **73**, 1581-1586 (1983).
- [11] E. K. Westwood and C. T. Tindle, "Shallow water time-series simulation using ray theory," *J. Acoust. Soc. Am.* **81**, 1752-1761 (1987).

- [12] C. T. Tindle and G. B. Deane, "Sound propagation over a sloping bottom using rays with beam displacement," *J. Acoust. Soc. Am.* **78**, 1366-1374 (1985).
- [13] N. G. Plumpton and C. T. Tindle, "Saddle point analysis of the reflected acoustic field," submitted for publication in *J. Acoust. Soc. Am.*, 1988.
- [14] G. N. Watson, *Theory of Bessel Functions* (Cambridge University Press, London, 1966).
- [15] C. S. Clay and H. Medwin, *Acoustical Oceanography* (Wiley, New York, 1977).
- [16] D. W. White and M. A. Pedersen, "Evaluation of shadow-zone fields by uniform asymptotics and complex rays," *J. Acoust. Soc. Am.* **69**, 824-840 (1970).
- [17] C. L. Pekeris, "Theory of propagation of explosive sound in shallow water," *Geol. Soc. Am., Mem. No. 27* (1948).
- [18] D. C. Stickler, "Normal-mode program with both the discrete and branch line contributions," *J. Acoust. Soc. Am.* **57**, 856-861 (1975).
- [19] C. T. Tindle, "Virtual modes and mode amplitudes near cutoff," *J. Acoust. Soc. Am.* **65**, 1423-1428 (1979).
- [20] A. O. Williams, Jr., "Pseudoresonances and virtual modes in underwater sound propagation," *J. Acoust. Soc. Am.* **64**, 1487-1491 (1978).
- [21] F. B. Jensen and W. A. Kuperman, "Sound propagation in a wedge-shaped ocean with a penetrable bottom," *J. Acoust. Soc. Am.* **67**, 1564-1566 (1980).
- [22] A. D. Pierce, "Guided mode disappearance during upslope propagation in variable depth shallow water overlying a fluid bottom," *J. Acoust. Soc. Am.* **72**, 523-531 (1982).
- [23] A. Kamel and L. B. Felsen, "Spectral theory of sound propagation in an ocean channel with weakly sloping bottom," *J. Acoust. Soc. Am.* **73**, 1120-1130 (1983).
- [24] J. M. Arnold and L. B. Felsen, "Rays and local modes in a wedge-shaped ocean," *J. Acoust. Soc. Am.* **73**, 1105-1119 (1983).

- [25] J. M. Arnold and L. B. Felsen, "Intrinsic modes in a nonseparable ocean wedge," *J. Acoust. Soc. Am.* **76**, 850-860 (1984).
- [26] E. Topuz and L. B. Felsen, "Intrinsic modes: Numerical implementation in a wedge-shaped ocean," *J. Acoust. Soc. Am.* **78**, 1735-1745 (1985).
- [27] J. M. Arnold and L. B. Felsen, "Coupled mode theory of intrinsic modes in a wedge," *J. Acoust. Soc. Am.* **79**, 31-40 (1986).
- [28] F. Xiang, M. Cada, and L. B. Felsen, "Intrinsic modes revisited," *J. Acoust. Soc. Am. Suppl. 1* **83**, S117 (1988).
- [29] H. Schmidt and F. B. Jensen, "A full wave solution for propagation in multilayered viscoelastic media with application to Gaussian beam reflection at fluid-solid interfaces," *J. Acoust. Soc. Am.* **77**, 813-825 (1985).
- [30] R. A. Koch, C. Penland, P. J. Vidmar, and K. E. Hawker, "On the calculation of normal mode group velocity and attenuation," *J. Acoust. Soc. Am.* **73**, 820-825 (1983).
- [31] T. Mannseth "On the theory of acoustic shallow water propagation," Dr. Scient. Thesis, Department of Applied Mathematics, University of Bergen (1986).
- [32] Session R. "Underwater Acoustics II: Quality Assessment of Numerical Codes, Part 2: Benchmarks," *J. Acoust. Soc. Am.* **80**, S36-S38 (1986).
- [33] F. B. Jensen and C. M. Ferla, "Numerical solutions of range-dependent benchmark problems in ocean acoustics," submitted for publication in *J. Acoust. Soc. Am.*, 1988.
- [34] R. B. Evans, "A coupled mode solution for acoustic propagation in a waveguide with stepwise depth variations of a penetrable bottom," *J. Acoust. Soc. Am.* **74**, 188-195 (1983).
- [35] R. B. Evans, "COUPLE: a user's manual, Report TN-232, Naval Ocean Research and Development Activity, NSTL Station, MS (1986).
- [36] M. J. Buckingham and A. Tolstoy, "An analytical solution for benchmark problem 1: the ideal wedge," submitted for publication in *J. Acoust. Soc. Am.*, 1988.

- [37] D. L. Bradley, "The Propagation of Sound in a Wedge-Shaped Shallow Water Duct," Ph.D. Thesis, The Catholic University of America, Washington, DC (1970) (unpublished).
- [38] D. L. Bradley and A. A. Hudimac, "The Propagation of Sound in a Wedge-Shaped Shallow Water Duct," NOLTR 70-235, Naval Ordnance Laboratory, Silver Spring, MD (1970).
- [39] A. Sommerfeld, "Mathematische Theorie der Diffraction," *Math. Ann.* **47** 317-341 (1896).
- [40] M. J. Buckingham, "Acoustic Propagation in a Wedge-Shaped Ocean with Perfectly Reflecting Boundaries," NRL Report 8793, Naval Research Laboratory, Washington, DC (1984).
- [41] D. E. Weston, "Horizontal Refraction in a Three-Dimensional Medium of Variable Stratification," *Proc. Phys. Soc. London* **78** 46-52 (1961).
- [42] C. H. Harrison, "Acoustic shadow zones in the horizontal plane," *J. Acoust. Soc. Am.* **65**, 56-61 (1979).
- [43] R. Doolittle, A. Tolstoy, and M. Buckingham. "Experimental confirmation of horizontal refraction of cw acoustic radiation from a point source in a wedge-shaped ocean," *J. Acoust. Soc. Am.* **83**, 2117-2125 (1988).
- [44] J. S. Perkins and R. N. Baer, "An approximation to the three-dimensional parabolic-equation method for acoustic propagation," *J. Acoust. Soc. Am.* **72**, 515-522 (1982).
- [45] G. A. Deschamps, "The Gaussian beam as a bundle of complex rays," *Electronic Letters* **7**, No. 23 (1971).
- [46] J. W. Ra, H. L. Bertoni, and L. B. Felsen. "Reflection and transmission of beams at a dielectric interface," *SIAM J. Appl. Math.* **24**, 396-413 (1973).
- [47] H. L. Bertoni, L. B. Felsen, and J. W. Ra, "Evanescent fields produced by totally reflected beams," *IEEE Trans. Antennas and Propagation* **AP-21**, 730-732 (1973).

21 February 1989

DISTRIBUTION LIST FOR  
ARL-TR-89-6  
UNDER CONTRACT N00014-87-K-0346

Copy No.

Commanding Officer  
Naval Ocean Research and Development Activity  
Stennis Space Center, MS 39529-5000

1 Attn: B. Adams (Code 110A)  
2 J. Matthews (Code 222)  
3 S. Chin-Bing (Code 221)  
4 D. Del Balzo (Code 244)  
5 R. Wagstaff (Code 425)  
6 H. Ali (Code 425)  
7 J. Caruthers (Code 220 )  
8 T. Goldsberry (Code 240)  
9 M. Collins (Code 221)  
10 P. Valent (Code 363)  
11 C. Salinger (Code 222)  
12 D. Lavoie (Code 363)  
13 W. Moseley (Code 200)  
14 J. Newcomb  
15 Library

Office of Naval Research Field Detachment  
Stennis Space Center, MS 39529-5000

16 Attn: E. D. Chaika (Code 125)  
17 B. N. Wheatley (Code 125)  
18 B. Blumenthal (Code 125)

Office of the Chief of Naval Research  
Department of the Navy  
Arlington, VA 22217-5000

19 Attn: M. Orr  
20 G. L. Johnson (Code 1125)  
21 R. Fitzgerald (Code 1125OA)  
22 R. Jacobson (Code 1125GG)  
23 J. H. Kravitz (Code 1125GG)  
24 R. F. Obrochta (Code 1221)  
25 K. W. Lackie (Code 125)

Office of the Chief of Naval Research  
Office of Naval Technology  
Department of the Navy  
Arlington, VA 22217-5000

26 Attn: J. T. Warfield (Code 234)

Distribution List for ARL-TR-89-6 under Contract N00014-87-K-0346  
(cont'd)

Copy No.

27 Commander  
28 Space and Naval Warfare Systems Command  
29 Department of the Navy  
30 Washington, D.C. 20363-5100  
Attn: L. Parish (PMW180)  
R. Mitnick (PMW180-5)  
D. Doolittle (PMW180-4)  
K. Evans (PMW180-4)

31 Commander  
32 Naval Sea Systems Command  
33 Department of the Navy  
34 Washington, D.C. 20362-5101  
Attn: P. Tiedeman (Code 63D3)  
M. Schultz (Code 63D7)  
Y. Yam (Code 63D4)  
E. Plummer (Code 63D1)

35 Commander  
Naval Air Systems Command  
Department of the Navy  
Washington, D.C. 20361-5460  
Attn: Code 933B

36 Director  
37 Naval Research Laboratory  
38 Washington, D.C. 20375  
39 Attn: O. Diachok (Code 5120)  
40 M. F. Czarnicki (Code 5110)  
41 F. Ingenito (Code 5160)  
42 D. Bradley (Code 5100)  
43 R. Gragg (Code 5160)  
44 R. Pitre (Code 5160)  
45 T. Foreman (Code 5160)  
46 W. A. Kuperman (Code 5160)  
47 J. Perkins (Code 5160)  
R. Baer  
A. Tolstoy  
Library

48 Commanding Officer  
49 Naval Ocean Systems Center  
50 San Diego, CA 92152-5000  
51 Attn: H. Bucker (Code 541)  
52 C. Persons (Code 732)  
F. Ryan (Code 541)  
D. Hanna (Code 702)  
Library

Distribution List for ARL-TR-89-6 under Contract N00014-87-K-0346  
(cont'd)

Copy No.

53	Chief of Naval Operations U. S. Naval Observatory Washington, D.C. 20390 Attn: CDR R. Hillyer (Code 006D3)
54	Office of the Chief of Naval Operations Department of the Navy Arlington, VA 20350 Attn: A. Bisson (OP02T)
55	Commander Naval Surface Warfare Center White Oak Laboratory Silver Spring, MD 20910 Attn: Library
56	Commander David Taylor Research Center Bethesda, MD 20084 Attn: Library
57	Commanding Officer Naval Oceanographic Office Stennis Space Center, MS 39522-5001 Attn: W. Jobst (Code 7300)
58	R. Hecht (Code 7310)
59	Library
60	Commanding Officer Naval Air Development Center Warminster, PA 18974 Attn: B. Steinberg (Code 5031)
61	Library
62	Officer in Charge Naval Underwater Systems Center New London Laboratory New London, CT 06320 Attn: P. Herstein (Code 33A3)
63	R. Deavenport (Code 3332)
64	W. Carey (Code 33A)
65	D. Lee (Code 3342)
66	B. Cole (Code 33A)
67	J. J. Hanrahan
68	Library

Distribution List for ARL-TR-89-6 under Contract N00014-87-K-0346  
(cont'd)

Copy No.

69	Superintendent
70	Naval Postgraduate School Monterey, CA 93943 Attn: H. Medwin (Dept. of Physics) Library
71	Commanding Officer
72	Naval Coastal Systems Center Panama City, FL 32407 Attn: Library G. McLeroy
73	Defense Advanced Research Projects Agency Arlington, VA 22209 Attn: C. Stuart
74	Commanding Officer Naval Intelligence Support Center Washington, D.C. 20390
75 - 86	Commanding Officer and Director Defense Technical Information Center Cameron Station, Building 5 5010 Duke Street Alexandria, VA 22314
87	Woods Hole Oceanographic Institution
88	86-95 Water Street
89	Woods Hole, MA 02543
90	Attn: R. Spindel J. Lynch G. Frisk R. Stephen
91	Science Applications, Inc.
92	1710 Goodridge Drive
93	McLean, VA 22101
94	Attn: C. Spofford
95	J. Hanna
96	W. Monet P. Rost P. Vidmar R. Cavanagh

Distribution List for ARL-TR-89-6 under Contract N00014-87-K-0346  
(cont'd)

Copy No.

	Applied Research Laboratory The Pennsylvania State University P.O. Box 30 State College, PA 16801
97	Attn: S. McDaniel
98	D. McCammon
99	F. Beebe
100	A. Pierce
101	Library
	Applied Physics Laboratory The University of Washington 1013 N.E. 40 St. Seattle, WA 98105
102	Attn: Library
	Marine Physical Laboratory Scripps Institution of Oceanography The University of California, San Diego San Diego, CA 92093
103	Attn: F. H. Fisher
	Bell Telephone Laboratories, Inc. Whippany Road Whippany, NJ 07961
104	Attn: C. DeHaven
105	R. Patton
106	Library
	Planning Systems, Inc. 7900 Westpark Drive McLean, VA 22101
107	Attn: B. Brunson
	Planning Systems, Inc. 115 Christian Lane Slidell, LA 70458
108	Attn: M. Bradley
109	W. Geddes
	Daubin Systems Corporation 104 Crandon Blvd. P. O. Box 49-0249 Key Biscayne, FL 33149
110	Attn: Lan Nghiem-Phu

Distribution List for ARL-TR-89-6 under Contract N00014-87-K-0346  
(cont'd)

Copy No.

111	TRW, Inc.
112	TRW Defense & Space Systems Group
	Washington Operations
	7600 Colshire Drive
	McLean, VA 22101
	Attn: R. T. Brown
	I. Gereben
113	School of Mechanical Engineering
114	Georgia Institute of Technology
	Atlanta, GA 30332
	Attn: P. Rogers
	Y. Berthelot
115	Department of Geology and Geophysics
	Geophysical and Polar Research Center
	Lewis G. Weeks Hall for Geological Sciences
	The University of Wisconsin, Madison
	1215 W. Dayton Street
	Madison, WI 53706
	Attn: C. S. Clay
116	Bolt, Beranek, & Newman, Inc.
117	1300 North 17th Street
	Arlington, VA 22209
	Attn: M. Flicker
	H. Cox
118	Hawaii Institute of Geophysics
119	The University of Hawaii
	2525 Correa Road
	Honolulu, HI 96822
	Attn: L. N. Frazer
	F. K. Duennubier
120	Director
121	North Atlantic Treaty Organization
122	SACLANT ASW Research Centre
123	APO New York 09019
	Attn: T. Muir
	F. Jensen
	T. Akal
	Library

Distribution List for ARL-TR-89-6 under Contract N00014-87-K-0346  
(cont'd)

Copy No.

	Defence Research Establishment Pacific FMO Victoria, BC VOS 1B0 CANADA
124	Attn: N. R. Chapman
125	D. Thomson
126	Library
	Defence Research Establishment Atlantic 9 Grove Street P.O. Box 1012 Dartmouth, NS CANADA
127	Attn: D. Chapman
128	F. Cotaras
129	D. Ellis
130	H. Merklinger
131	Library
	Rosenteil School of Marine and Atmospheric Science Division of Ocean Engineering University of Miami Miami, FL 33149-1098
132	Attn: H. DeFarrari
133	T. Yamamoto
	Applied Physics Laboratory The Johns Hopkins University John Hopkins Road Laurel, MD 20810
134	Attn: J. Lombardo
135	G. Gillette
136	A. Boyles
137	R. Rottier
138	Library
	Department of Ocean Engineering Massachusetts Institute of Technology Cambridge, MA 02139
139	Attn: I. Dyer
140	A. Baggeroer
141	H. Schmidt
	The Catholic University of America Washington, D. C. 20064
142	Attn: H. Uberall
143	J. J. McCoy

Distribution List for ARL-TR-89-6 under Contract N00014-87-K-0346  
(cont'd)

Copy No.

144	The University of Miami 10 Rickenbacker Causeway Miami, FL 33149 Attn: F. Tappert
145	M. Brown
146	Department of Electrical Engineering Polytechnic Institute of New York Farmingdale, NY 11735 Attn: L. B. Felsen
147	I. Tolstoy Knockvennie, Castle Douglas S.W. SCOTLAND GREAT BRITAIN
148	Department of Aerospace Engineering and Engineering Mechanics The University of Texas at Austin Austin, TX 78712 Attn: A. Bedford
149	C. Yew
150	Department of Geology The University of Texas at Austin Austin, TX 78712 Attn: C. Wilson
151	Department of Physics The University of Auckland Private Bag, Auckland NEW ZEALAND Attn: A. C. Kibblewhite
152	C. T. Tindle
153	G. Bold
154	Defence Scientific Establishment HMNZ Dockyard Devonport, Auckland NEW ZEALAND Attn: K. M. Guthrie
155	R. Bannister
156	Library
157	Chinhae Research Laboratory P.O. Box 18 Chinhae, Kyeong Nam KOREA Attn: Jungyul Na

Distribution List for ARL-TR-89-6 under Contract N00014-87-K-0346  
(cont'd)

Copy No.

158	The Lamont-Doherty Geological Observatory
159	Columbia University Palisades, NY 10964 Attn: R. D. Stoll G. M. Bryan
160	Physics Department Georgetown University Washington, DC 20057 Attn: K. Ng
161	National Center for Physical Acoustics
162	Box 847 University, MS 38677 Attn: K. Gilbert Library
163	5th Research Center Japan Defense Agency 3-13-1 Nagase Yokosuka, Japan Attn: K. Ohta
164	Royal Aircraft Establishment Radio and Navigation Department Farnborough, Hampshire GU14-6TD ENGLAND Attn: M. Buckingham
165	Sonoquest P.O. Box 153 Wellesley Hills, MA 02181 Attn: J. Chanuel
166	Syntek Engineering and Computer Systems, Inc. 2101 E. Jefferson St., Suite 300 Rockville, MD 20852 Attn: P. Etter
167	Department of Physics University of Bergen Bergen, Norway Attn: H. Hobaek
168	Department of Oceanography Texas A&M University College Station, TX 77843 Attn: A. Anderson

Distribution List for ARL-TR-89-6 under Contract N00014-87-K-0346  
(cont'd)

Copy No.

169	Department of Physics
170	The University of Texas at Austin
	Austin, TX 78712
	Attn: W. McCormick
	A. W. Nolle
171	Department of Mechanical Engineering
	The University of Texas at Austin
	Austin, TX 78712
	Attn: M. F. Hamilton
172	Department of Electrical Engineering
173	The University of Texas at Austin
174	Austin, TX 78712
	Attn: H. Ling
	F. Bostick
	S. Marcus
175	William S. Livingston
	Vice President and Dean of Graduate Studies
	Main Building 101
	The University of Texas at Austin
	Austin, TX 78712
176	Robert A. Altenburg, ARL:UT
177	Hans A. Baade, ARLUT
178	David Ball, ARL:UT
179	Nancy R. Bedford, ARL:UT
180	David T. Blackstock, ARL:UT
181	Hollis C. Boehme, ARL:UT
182	W. Eugene Brown, ARL:UT
183	Ilene J. Busch-Vishniac, ARL:UT
184	Nicholas P. Chotiros, ARL:UT
185	George P. Coble, ARL:UT
186	Glen E. Ellis, ARL:UT
187	Karl C. Focke, ARL:UT
188	Marshall E. Frazer, ARL:UT

Distribution List for ARL-TR-89-6 under Contract N00014-87-K-0346  
(cont'd)

Copy No.

189	David E. Grant, ARL:UT
190	Thomas A. Griffy, ARL:UT
191	James Hawkins, ARL:UT
192	Celeste H. Henderson, ARL:UT
193	Terry L. Henderson, ARL:UT
194	Kirk L. Holub, ARL:UT
195	John M. Huckabay, ARL:UT
196	William A. Kennedy, ARL:UT
197	Robert A. Koch, ARL:UT
198	Scott J. Levinson, ARL:UT
199	Fredrick W. Machell, ARL:UT
200	John W. Maxwell, ARL:UT
201	Ilene L. McCool, ARL:UT
202	Stephen K. Mitchell, ARL:UT
203	Susan G. Payne, ARL:UT
204	Clark S. Penrod, ARL:UT
205	F. Michael Pestorius, ARL:UT
206	Jonathan E. Pickett, ARL:UT
207	Carol V. Sheppard, ARL:UT
208	Jack A. Shooter, ARL:UT
209	Steven Sotts, ARL:UT
210	Deborah A. Summa, ARL:UT
211	James Tencate, ARL:UT
212	Jacqueline N. Tjøtta, ARL:UT
213	Sigve Tjøtta, ARL:UT

Distribution List for ARL-TR-89-6 under Contract N00014-87-K-0346  
(cont'd)

Copy No.

214	Bernard F. Tupa, ARL:UT
215	Gary R. Wilson, ARL:UT
216	Library, ARL:UT
217 - 232	Reserve, ARL:UT